國立中山大學材料與光電科學學系

博士論文

鋯基金屬玻璃薄膜複材與微米柱之強化韌化與微奈米機械性質分析

Strengthening and Toughening of Zr-Based Thin Film Metallic Glasses and Composites under Nanoindentation and Micropillar Compression

研究生：周鴻昇 撰

指導教授：黃志青 博士

中華民國　一百　年 三 月

國立中山大學研究生學位論文審定書

本校材料與光電科學學系博士班

研究生周鴻昇（學號：D963060003）所提論文

鋯基金屬玻璃薄膜複材與微米柱之強化韌化與微奈米機械性質分析
Strengthening and Toughening of Zr-Based Thin Film Metallic Glasses and Composites under Nanoindentation and Micropillar Compression

經本委員會審查並舉行口試，符合博士學位論文標準。

學位考試委員簽章：

鄭憲清　　林仁輝

林哲信　　張六文

黃志青

指導教授　黃志青

系主任/所長　陳　明

致謝

依稀記得在碩二那年的寒假，經過深思熟慮之後，跟老師提到說想要接著繼續念博士班的那一刻，現在已經到了博士班的最後階段。在這段精彩(辛苦)的時間中，感謝恩師 黃志青教授循循善誘，引領學生進入學術研究之殿堂。老師對我們的無比關懷讓我們在遭遇瓶頸時能夠從困境中爬起來，也教導我們即使實驗上有突破，也要保持謙卑的態度。若沒有恩師的引領，便沒有今日的我，於此，誠摯的獻上一聲，「老師，謝謝您。」在研究上，也要特別感謝中山大學材光系張六文老師，在建置磁控濺鍍設備時的大力幫助，並且在性質量測及電子顯微鏡分析上亦提供許多非常寶貴且重要的意見。

由衷感謝中山大學材光系張六文教授，機電系林哲信教授，成功大學機械系林仁輝教授，義守大學機械系鄭憲清教授，不辭辛勞擔任論文口試委員，寶貴的意見與指正令本論文的內容更加完善，令我獲益良多。此外，特別感謝赴美從事學術交流的三個月期間，田納西大學材料系聶台岡教授於研究上的分享其卓越之見解，打開了我的眼界。且聶教授在生活上無微不至的照顧令我雖離家十萬公里，亦倍感窩心。同時感謝聶教授的學生們，宋雙喜，王常利及王璐在研究及生活上的幫助。

研究所期間深受許多人的幫助，有你們的幫忙令我可更專心地從事研究。感謝中山大學貴重儀器中心李秀月小姐、林明政先生、王良珠小姐、施淑娸小姐、高靖惟小姐提供儀器且協助樣品測試。感謝中山大學奈米科技研發中心鹿文卿小姐，顏采蓉小姐協助研究相關事務。感謝中山大學物理系核心設施陳彥文先生在製程上的鼎力相助。感謝所辦朱惠敏、顏秀芳、陳秀玉小姐在行政公務處理的幫忙。感謝系上華應騏大哥在做人做事上態度的教導，令小弟我獲益匪淺。

精彩的研究歲月中，先感謝實驗室金屬玻璃的第一把交椅，洪子翔學長。子翔學長在我碩士班的期間，毫無保留的傳授其研究經驗，懇切耐心的指導令我有

好的研究基礎，讓我在進入博士班後，學長的教導讓我能夠很快的就掌握研究方向。此刻的成果，學長功不可沒。也要感謝實驗室熱機性質分析專家，大神張育誠學長，育誠學長在熱機分析上的引領，讓我能夠從就不同的角度來看待金屬玻璃。感謝實驗室博士後研究員杜興蒿博士，在實驗設計及分析上提供許多精闢的見解，杜博士對本研究亦有相當大的助益。感謝張六文實驗室黃鐙興學弟，在電子顯微鏡分析技術上細心的教導。感謝實驗室大學長李敬仁博士後研究員在實驗上的鼎力相助。感謝目前正在服役中的賴炎暉及陳海明學長，陪伴我撐過博士班最辛苦的時期。感謝張志溢學長在我徬徨的時候，提點我未來的方向。感謝正在美國做博士後研究的羅友杰博士，其真誠的個性及淵博的知識，令小弟我景仰不已。感謝實驗室這些可愛的夥伴，幽默風趣充滿幹勁的裴帥裴浩然，糾肝新的思威特劉名哲，攝影功力一流的郭哲男，實驗室的陽光健身教練宋大豪，真心愛主的官聖堯，只要一個微笑就能迷倒許多美女的超級帥氣安迪哥黃朝先，還有實驗室碩士班學弟妹們，黃瀚生，陳柏佑，胡婷婷，陳盈翰及林維昭。有你們的陪伴，令我的研究生活更加多采多姿，不會孤單寂寞。

接著感謝我的好友，很愛貓的涂小良，老師有沒有說的河馬何立凱，又高又帥的大炳王炳順，動不動就推坑的口琴破壞神樊彥廷，在這段時間雖然我們都在不同的地方奮鬥，你們的鼓勵與陪伴令我更加珍惜這份深厚的感情，真的是我這輩子無價的財富。

最後我要特別感謝我的父母和妹妹，在家裡不寬裕的情況下，依然默默的支持我，不辭辛勞的付出，讓我無後顧之憂，讓我完成博士班的學業。你們的關懷愛護的恩情無以為報，我愛你們。

周鴻昇 謹誌

於中山西灣

Content

List of Tables

List of Figures

Abstract

Since the first discovery of amorphous alloys in 1960, researchers have explored many unique mechanical, magnetic, and optical characteristics of such materials for potential applications. Up to now, well-developed processes, such as rapid quenching, sputtering, evaporation, pulse laser deposition, etc, have been applied for different applications in micro-electro-mechanical systems (MEMS). Due to the lack of ordered structure, amorphous alloys can bear a high stress in the elastic region. Their plastic deformation stability is also of interest and has been widely studied. The shear-band characteristic, a kind of inhomogeneous deformation mechanism, dominates the deformation after yielding at room temperature. While a shear band nucleate, its propagation usually cannot be arrested or stopped. In other words, the occurrence of matured shear bands needs to be prevented. There are two major approaches in this aspect. The first is to increase the material yield strength so as to delay the shear band nucleation. Another is to incorporate intrinsic or extrinsic particles so as to absorb the kinetic energy of shear bands in the amorphous matrix.

In this study, we utilize three strategies to control the propagation of shear bands in thin film metallic glasses (TFMGs): sub-T_g annealing, the addition of strong element in solute form, and the introduction of strong nanocrystalline layers. For sub-T_g annealing, the base alloy system is $Zr_{69}Cu_{31}$, with a base film hardness of 5.1 GPa measured by nanoindentation. After annealing, the hardness exhibits ~30% increase. Without the occurrence of the phase transformation, as confirmed by X-ray diffraction, the possible reaction during sub-T_g annealing is attributed to structural relaxation, not crystallization. The full width at half maximum of the X-ray peak exhibits a decreasing trend in the using X-ray and transmission electron microscopy diffraction, meaning the excess free volumes forming during

vapor-to-solid deposition process would be annihilated by localized atomic re-arrangement. Moreover, the formation of medium-ordering-range clusters was confirmed utilizing high-resolution transmission electronic microscopy. The denser amorphous structure leads to the increment of hardness.

For the addition of Ta in $Zr_{55}Cu_{31}Ti_{14}$, sputtering provides a wide glass forming range with solubility of Ta approaching ~75 at%. With increasing Ta content, the elastic modulus and hardness increase slowly. A steep rise occurs at ~50 at% of Ta. Up to 75 at% of Ta, the elastic modulus and hardness approaches 140 GPa and 10.0 GPa, respectively (100% increment). Up to now, Ta-rich TFMGs exhibit the highest elastic modulus and hardness among all amorphous alloys fabricated using vapor deposition techniques. The irregular increase is attributed to the formation of Ta-Ta bonding. A large quantity of Ta bonds would lead to the formation of Ta-rich nanoclusters, drastically decreasing the strain rate while shear band propagates under nanoindentation and microcompression tests. The introduction of nanocrystalline Ta layers can not only effectively enhance the yield strength but also serve as the absorber for the kinetic energy of shear bands, revealing ductility in the microcompression test.

中文摘要

在 1960 年，自從第一個非晶質合金被製備出來後，許說研究學者發現非晶質合金在機械行為，光學性質，電磁應用，及超導現象具有許多獨特優點。隨著時間的演進，許多成熟的製程，如液態急冷，磁控濺鍍，蒸鍍，脈衝雷射鍍膜等技術，已經被開發出來。由於非晶質合金不具有長程有序的晶體結構，因此非晶質合金較相同成分的合金材料具有更高的彈性極限及降伏強度。

許多學者們發現，在常溫下非晶質合金的塑性變形行為為剪切變形帶(shear band)所主導。更進一步來說，此種行為會進一步誘發加工軟化(work softening)之現象。對於結構材來說，此種不均勻之便型特性會使非晶質合金的應用受到限制。近年來，針對這個問題，許多由非晶質合金及不同強化相所組成的非晶質合金複合材料被大量的開發及研究。其目的是希望節由強化相來分散期集中在滑移面上的剪應力，並且藉由強化相來吸收剪切變形帶之能量，進而阻止剪切變形帶之前進。

在本論文中，吾人利用三種不同的策略來料了解剪切變形帶並進而控制剪切變形帶之發展。第一種為利用結構鬆弛來觀察非晶質合金的機械性質變化及行為。利用 sub-T_g 退火，在製程中所生成的過量之自由體積藉由結構鬆弛而消滅，導致硬度大幅度提升。在 $Zr_{52}Cu_{29}Ti_{19}$ 非晶質合金中，其硬度的提升從 5.2 GPa 至 6.9 GPa (~30%的提升)。但從奈米壓痕的數據中發現，其 pop-in 事件的增多，為來自於過量之自由體積在結構鬆弛中被消滅並在非晶質母材中產生中程有序團簇。

第二種為添加合金元素，使添加元素以溶質存在於非晶質母材之中。所選用的母合金系統為 ZrCu；添加元素為 Ti 及 Ta。由於鈦的各方面性質與鋯極為相似，硬度提升的效果並不明顯，而若添加 Ta，其硬度隨著鉭含量上升而上升，最高可達到 10.0 GPa，

為近乎 100%的提升，利用高解析電子顯微鏡之技術發現，在原子影像下，可發現高密度之奈米團簇存在於非晶質母材之中。推測其生成之原因為 Ta 含量的上升，產生大量的 Ta-Ta 鍵結，因而生成其奈米團簇。

在奈米壓痕及微米壓縮之測試中，由於高含量 Ta 的添加使非晶質母材中形成大量奈米金屬團簇，進而影響剪切變形帶的前進，進而產生大量剪切變形帶。第三中為導入高強度奈米金屬層，所選用之材料為鉭，利用高強度奈米鉭做為吸收剪切變形帶動能的吸收層。由於導入的高強度 Ta 層，所量測到之硬度有約 60%的上升。更進一步在微米壓縮測試的結果中發現，利用多層結構除了提昇強度之外，在剪切變形帶發展的初期，能夠藉由奈米晶 Ta 吸收剪切變形帶之動能，展現出延展性。

Chapter 1 Introduction

1-1 Amorphous metallic alloys

Amorphous alloys are a kind of metallic materials with disordered structures. The structure of amorphous alloys displays as a random structure which consists of a short-range order structure, as shown in Fig. 1-1, in contrast to the structure of crystalline materials showing a long-range order in repeating unit cells, as shown in Fig. 1-2 [1]. According to the appearance and thermodynamic characteristics of these materials, amorphous metallic alloys are also called as liquid metals, glassy metals, non-crystalline metals, or metallic glasses.

As people know, the rapidly quenching method from the liquid to solid phase is the most popular way to synthesize amorphous alloys in forms of ribbons, bulks, or powders. This principle is based on the solidification through a sufficiently high cooling rate in order to freeze the amorphous structure of liquid. At the initial stage, it is considerably difficult to reach such a high cooling rate about 10^7 K/s. However, a novel method that can reduce effectively the critical cooling rate (lower than 10^3 K/s) to fabricate bulk metallic glasses was discovered during 1980s by adding the third element into the original binary system. The amorphous alloys are very suitable for the increased demand to resist the severe environmental situations because of their particular properties.

The disordered structure is different from the crystalline structure with the same construction in repeating unit cell. The interval between atoms to each other is called the free volume. Due to the lack of the long-range-order structure, amorphous alloys exhibit the shear band deformation mechanism. In addition, other characteristics, such as lower Young's modulus, higher tensile strength, higher electric resistance, and excellent gas absorption ability, and etc, are widely focused.

Recently, to achieve the ultimate goal of the light and tough engineering application, the amorphous alloy is considered to be a potential material. Inoue's group [2] produced ternary and multi-component bulk metallic glasses for structural or functional applications, such as protective coating. The outshape of Vertu, the famous cellphone of Nokia, is coated by liquid-metal alloys, as shown in Fig. 1-3 [3]. Owing to the trend of microminiaturization in the electronic industry, high strength and tough thin films metallic glasses with excellent superplastic formation ability are very suitable for the enclosures of electrical parts. Up to now, the Pd-based and Zr-based metallic glass thin film is developed as a microactuator and nanopatterning, as shown in Figs. 1-4 [4] and 1-5 [5], respectively.

1-2 Characteristics of bulk metallic glasses (BMGs) and thin film metallic glasses (TFMGs)

During the last decade, bulk metallic glasses (BMGs) fabricated by liquid-quenching were widely focused. Considering the hurdle in processing, the biggest problem of the fabrication in using the rapidly quenching method is to achieve an enough cooling rate (greater than 10^6 K/s). However, Inoue [6] solved this problem using the following rules for the synthesis of amorphous alloys:

(1) Multi-component systems consisting of more than three elements,

(2) Significant difference in atomic size ratios above 12% among the three main constituent elements,

(3) Negative heats of mixing among the three main constituent elements.

The third element replacement for partial or complete substitution by Gd, Ni, or Y in the Mg-Cu system is an important and valid way to solve the problem in fabrication and the diameter enlargement of BMGs [2,7]. In addition to the advantages mentioned above, adding the third or more elements into an alloy system is able to adjust the properties of BMGs for some particular applications.

Contrary to liquid quenching, vapor quenching is also a potential way for the fabrication of amorphous alloy through providing a higher cooling rate than that of liquid quenching. The development of vapor deposition technique for the fabrication of amorphous alloys was started at the 1960s [8]. Utilizing physical vapor deposition, such as evaporation and sputtering, the amorphous alloys can be also fabricated. Compared with TFMGs, the rapidly quenching method through liquid-solid route for bulk or ribbon of metallic glasses is mainly limited to the intrinsic nature of materials and the cooling rate in process. Sputtering and evaporation provide a wider glass forming range and a high cooling rate. Two main ways for the fabrication of TFMGs are listed below:

(1) Direct methods: co-sputtering and alloy sputtering,

(2) Indirect methods: annealing-induced and stress-induced amorphization.

The direct methods are similar to the liquid quenching method for BMGs. In the co-deposition process, the TFMGs could be fabricated with an enough fast cooling rate (above 10^8 K/s), such as the success for the binary Al-Fe [9] and Au-La [10] systems. However, TFMGs can be produced in using the alloy deposition technique with a lower cooling rate by adding the third or more elements. The Zr-Cu-Al [11], Zr-Cu-Al-Ni [12] and Pd-Cu-Si [13] TFMGs are successful cases in using the alloy sputtering process. The annealing-induced process is a potential method for a large mount of the continuous fabrication with lower cost and high reliability. Although the stress-induced amorphization, such as cold rolling and ball milling, is a well-known way for the modification of materials, the mechanism and phenomena will not be discussed particularly because this is not the emphasis in this thesis.

1-3 Mechanical properties and responses of amorphous alloys from microscope aspect

Due to the lack of crystalline structure, the mechanical properties and responses of amorphous alloys are also different from that of crystalline alloys. The yielding strength of amorphous alloy is close to ideal strength (~10/G) [14], where G is shear modulus. This result implies that the strength of metallic glasses is determined solely by the chemical bonding force between the constitutive atoms, similar to the result for defect-free crystals. In principle, such results are unexpected from the known deformation models of metallic glasses, in which the yielding is controlled by the intrinsic defects (free volumes) and the initiation of shear transformation zones (STZs), rather than by the inter-atomic chemical bonding in perfect crystals.

From the microscope aspect, the plastic deformation is not attributed to the dislocation in crystalline materials. Up to now, there are several theories to describe the deformation mechanism of amorphous alloys [14]. The well-known one is the STZ model [15], indicating shear deformation occurs by spontaneous and cooperative reorganization of a small cluster of randomly close-packed atoms as shown in Fig. 1-3. During compressive tests, a lot of shear transformation zones would form along the shear plane with the largest shear stress and induce the shear event, called as shear bands. The overall plastic deformation roughly can be attributed to the cooperative movement along the same direction.

1-4 Purpose and motive of this research

Amorphous alloys are potential materials for MEMS and other applications for some functional purposes, such as good wear and corrosion resistance, high hydrogen-storage ability, and antibiotic coating, etc. Inoue [7] have reported various BMG systems, such as Fe-, Co-, Zr-, Pd-, and Mg-based systems, and their applications since 1980. Reducing the critical cooling rate by the addition of alloy elements is able to modify the thermal, mechanical, electric or magnetic properties. Though BMGs have excellent properties, they might be hard to be made as micro- or even nano-components in MEMS devices. The thin-film technique for MEMS has been used in metallic glasses since 1980s. The large-area thin films with uniform-distribution of the composition and the structure are able to be fabricated.

In this study, thin film metallic glasses consisting of zirconium, copper, titanium, and tantalum will be fabricated. The amorphous ZrCuTi and ZrCuTiTa alloy thin films are fabricated utilizing the co-sputtering. Due to the positive heat of mixing in Zr-Ta (+3 kJ/mol), Cu-Ta (+2 kJ/mol) and Ti-Ta (+1 kJ/mol), Ta is a suitable element for our purpose. Tantalum will serve as solute atoms in the amorphous matrix without the precipitation of the intermetallic compounds. Amorphous Zr-Cu-Ti/nanocrystalline Ta nano-laminates are fabricated by alternative deposition. There are three different approaches to enhance the mechanical properties, listed below:

(1) Strengthening of TFMGs by structure relaxation of Zr-Cu-Ti fully amorphous TFMGs via sub-T_g annealing, where T_g is the glass transition temperature.

(2) Strengthening of TFMGs by addition of immiscible tantalum to form possible phase separation,

(3) Strengthening of TFMGs by multilayer thin films design for the Zr-Cu-Ti/Ta thin film nano-composites.

In terms of the first type, the sub-T_g annealing is the major effect, influencing the mechanical properties and responses. In the second type, the component of the bonds is changed by adding the different amounts of tantalum. The final type is designed as the nanolaminate form, which can not only provide the interface influence but also the high strength of tantalum in the third type. The mechanical properties of TFMGs are tested and compared by several kinds of mechanical tests, such as nanoindentation and microcompression testing. Finally, we discuss the advantages and disadvantages among these methods for strengthening of amorphous alloys.

Chapter 2 Background and Literature Review

2-1 Evolution of amorphous alloys

2-1-1 Evolution of bulk and thin film metallic glasses

In 1960s, Klement et al. [16] developed firstly the splat quenching method to fabricate the Au-Si amorphous alloy in avoiding crystallization during solidification. Owing to the unique characteristics of the amorphous structure, this method generated wide interests of the new type alloy among scientists and engineers. In 1969, Chen and Turnbull [17] successfully synthesized an amorphous alloy of the Pd-Si-X (X= Ag, Cu or Au) ternary system. A few years later, Chen [18] fabricated the Pd-T-Si (T= Ni, Co or Fe) ternary amorphous alloy in using the die casting and roller-quenching method, and the maximum diameter of BMGs was 1 mm. They also analyzed effects of the alloy systems and compositions by the thermodynamic calculation. As the replacement atoms increased, the arrangement of atoms was more random. The glassy metal was more easily to form.

Other potential processes for fabrication were published since early 1980s. In 1983, Schwarz and Johnson [10] fabricated first the La-Au TFMG by the solid-state reaction. Furthermore, they found the broad hump from 25^{o} to 45^{o} by X-ray diffraction (XRD) with Cu $K\alpha$ radiation, representing the formation of amorphous structure. After 1983, more alloy systems were fabricated by evaporation and sputtering. In 1986, Cotts et al. [19] successfully fabricated the Ni-Zr multilayer thin films via sputtering, and observed the amorphization of crystalline metallic thin film by differential scanning calorimetry (DSC) at a constant temperature scanning rate of 10 K/min. The formation of amorphous phase means that it is the intermediate state from crystalline phase to intermetallic compound. In the beginning of 1980s, Kui et al. [20] produced firstly the Pd-Ni-P bulk metallic glass with 5 mm diameter by the heating and cooling cycle. They used this method which may decrease the homogeneous and heterogeneous crystalline nucleation rate, and successfully improved the BMG maximum diameter from 5 mm to 10 mm by processing the Pd-Ni-P melt in a boron oxide flux.

In addition to rapid casting and solid-state reaction, as mentioned above, sputtering provides another process to fabricate the amorphous alloys. Chen et al. [21] rapidly fabricated the amorphous Al-Fe, Bi-Fe and Bi-Ti alloys via co-sputtering in 1988. The thin film was deposited on the NaCl substrate cooled by liquid nitrogen. In late 1980s, Inoue's group [7] in Tohoku University of Japan developed many new multi-component bulk metallic glass systems with the lower cooling rate in Mg-, Ln-, Zr-, Fe-, Pd-, Cu-, Ti- and Ni- based systems. Amorphous alloys started to be popularly noted and studied due to the overcoming of the critical problem in fabrication.

In 1996, Dudonis et al. [22] produced the amorphous Zr-Cu TFMGs by co-sputtering. They first discussed the structure by change deposition factors, such as the working pressure, the substrate temperature. Besides sputtering, the thin film metallic glasses can be fabricated via another deposition process, such as pulse laser deposition. Comparing the sputter deposition and pulse laser deposition, the major difference is the kinetic energy with the incident atoms. The greater kinetic energy of the incident atoms would induce the formation of the metastable amorphous phase. Moreover, some immiscible alloy systems, such as Fe-Zr and Co-Zr, can be fabricated using pulse laser deposition. For example, Krebs et al. [23] pointed out that the amorphous phase in these binary (Fe, Co, Cu)-Zr, Cu-Ti and Fe-Nb systems would form in the middle concentration range.

Near 2000, Akira's group [11,13] at Precision and Intelligence Laboratory developed the Zr-Cu-Al and Pd-Cu-Si ternary TFMGs, fabricated by alloy sputtering, for MEMs application. The benefit of alloy sputtering is that the deviation of composition between target and as-deposited films can be neglected. Moreover, because of a large super-cooled region, excellent three-dimension forming ability, good corrosion resistance and mechanical properties, the Zr- and Pd- based TFMGs are appropriate choices for the conical spring linear micro-actuator in MEMS. This report opened the TFMGs application in the MEMS industry.

Annealing-induced full amorphization in multi-component monolayer thin films was reported by Chu et al. [12] in 2004. The Zr-Al-Cu-Ni crystalline thin film was annealed under argon atmosphere at the heating rate of 40 K/min and the holding time of 60 s at the temperatures range from 550 to 950 K. The crystalline phase transferred to the metastable amorphous phase due to the atomic inter-diffusion. Compared with direct fabrication methods of TFMGs, this method can save much energy and cost because this method does not need to maintain the very low temperature of the substrate. Thus, the post-treatment methods to fabricate TFMGs are potential processes with the convenience and low cost.

After one year, Inoue's group [4] fabricated the nano-device by the nano-scale pattering technique. The Zr-Al-Cu-Ni TFMGs were deposited by magnetron sputtering. The nano-pattern on Zr-based TFMGs was produced by the focus ion beam (FIB) technology. This nano-pattering technology may be applied to fabrication of nano-mold and high-density memories.

Many researchers have reported evolution and improvement of TFMGs fabrication by a wide margin since 1960s. Because of the application of TFMGs in MEMS, several important properties, such as the electric resistance [24], hardness [25], fracture phenomena [26], reliability [27] and mechanical properties [13,28], were noticed and researched. Due to the absence of defects, the size effect is the major factor which leads to different properties between bulk and thin-film specimens. When the dimension of a crystalline material becomes as small as they can in MEMS, the intrinsic length scales, such as the grain size and dislocation structure, are no longer small in comparison with the geometric dimensions of the material, which can cause reliability problems of the microcomponents. The research of Zhang et al. [29] reported the deformation behavior of free-standing Pd-based TFMGs in 2005. As the results of the bending test, as-deposited films revealed ductility due to the existence of shear bands. After annealing, ductility might transfer to the brittleness because of the absence of shear bands.

In conclusion, it is ready to enter a more mature stage since amorphous alloys started to develop in 1960. Multi-component bulk metallic glasses produced by Inoue's group in using the liquid-quench method have excellent mechanical properties, the superplastic formation ability and thermal stability. Due to these advantages, amorphous alloys can be used in bulk application easily. The outer shape of amorphous alloys is able to strengthen the resistance to severe circumstance. However, deposition techniques, providing a convenient way to fabricate TFMGs with uniform thickness, composition and smooth surface, are potential materials as MEMS parts because it is fast, low-cost, and very easy to control the composition and morphology. Furthermore, all kinds and shapes of materials are easy to be coated with an amorphous thin layer for improvement of properties.

2-1-2 Glass forming ability (GFA)

For the phase transformation of amorphous alloys, the crystallization path from amorphous phase to crystalline phase is shown in Fig. 2-1. In the case of the liquid-quenching process, due to the complication of multi-component alloy systems, many empirical criteria were announced to characterize the glass-forming ability (GFA) thermal stability. The design of alloy system, and evaluation and prediction of properties can become easier, effective, and more economic. Considering the effect thermodynamic and dynamic effect during quenching, four popular criteria were announced:

(1) Supercooled liquid range, ΔT_x (= T_x - T_g, where T_x and T_g are the onset crystallization temperature and the glass transition temperature, respectively) [30],

(2) Reduced glass transition temperature, T_{rg} (= T_g/T_l, where T_l is the liquidus temperature) [31],

(3) γ (= $T_x/(T_g + T_l)$) [32],

(4) γ_m (= $(2T_x-T_g)/T_l$) [33].

First, ΔT_x is the first criterion of GFA and popularly used as an index of the thermal stability. As illustrated in Fig. 2-1, amorphous alloys exhibit the nature of ideal Newtonian fluid which is very suitable for forming [32]. The large ΔT_x value indicates that the disordered structure can exist in a wide temperature range without crystallization. This implied the resistance for crystallization and growth of crystalline phase [34]. However, ΔT_x is a rough parameter which does not consider any crystallization mechanism during cooling and heating process. Second, ratio of T_g/T_l was introduced for pure kinetic reactions associated with the need to avoid crystallization. T_{rg} (= T_g/T_l) is typically assumed to be less dependent on compositions, while T_l often decreases more strongly. The interval between T_l and T_g thus generally decreases and the value of T_{rg} increases with increasing alloying concentration so that the probability of being able to cool through this 'dangerous' range without crystallization is enhanced.

Therefore, a new parameter γ based on $T_x/(T_g + T_l)$ was announced by Lu and Liu [32] in 2002. As Lu and Liu mentioned in the article, γ is more suitable and accurate to evaluate glass-forming abilities of alloy systems because of completely consideration of thermal stability and resistance to crystalline, as shown in Fig. 2-2 [35]. Besides, it also has a relation with the critical cooling rate (R_c) and critical specimen thickness (Z_c), and the relationship has been formulated as follows:

$$R_c = 5.1 \times 10^{21} \exp(-117.19\gamma) , \tag{2-1}$$

$$Z_c = 2.80 \times 10^{-7} \exp(41.70\gamma) , \tag{2-2}$$

In 2007, Du et al. [33] reported the modified glass forming parameter (γ_m) to predict the glass forming ability. The modified GFA parameter emphasizes on the relationship between the liquid phase stability and the crystallization resistance. In other words, the glass forming ability of the unknown systems can be easily to predict by utilizing the measurement of the thermal properties in alloy design. Compared with the liquid-quenching process, these empirical rules usually can not work. The reason is that the greater cooling rate in vapor-quenching leads to a larger glass forming range than that in liquid-quenching.

2-1-3 Fabrication of amorphous alloys

Fabrication processes of amorphous alloys may be divided into two processes:

(1) Quenching processes: splat quenching, chill block melt spinning (CBMS), planar flow casting (PFC), spray forming, conventional metallic mold casting, high pressure die casting, pulse laser deposition (PLD), sputter deposition, and evaporation deposition [36].

(2) Solid-solid amorphization (SSA) which occurs only in solid phase: annealing, ion

implantation, ion beam mixing, mechanical alloying (MA), and accumulative roll bonding (ARB).

Generally speaking, amorphous phase in alloys is the meta-stable state compared with the alloy of the same composition. To get the metastable structure, the quenching processes can freeze the liquid or vapor structure from the liquid or vapor to solid, respectively.

As noted, the production of amorphous films requires very high cooling rates which can be reached by the increment of the contact surface with heat sinker and the container/substrate with a low temperature. Utilizing the quenching process, the metastable structure can be frozen preventing from diffusing into equilibrium lattice sites. To reach a sufficient cooling rate, liquid nitrogen or helium is usually used. In mid-1950s, Buckel [37] fabricated amorphous films of pure metals, such as Ga and Bi, by thermal evaporation onto the substrate maintained at the liquid helium temperature with the fast cooling rate above 10^{10} K/s. Because the cooling rate was too hard to reach, the fabrication of the amorphous alloys became easier after the multi-component alloy system reported in 2000.

The splat quenching method was first announced by Klement et al. [16] in order to raise the cooling rate, as shown in Fig. 2-3 [36]. An amorphous irregular die (area ~0.2 mm^2; thickness ~10 μm) can be fabricated under the cooling rate (10^6 to 10^{10} K/s). Figure 2-4 shows the two roller quenching method announced [36]. This method broke the limitation of amorphous alloys. Hence, it caused wide attention because uniform long ribbons (width ~2 mm; thickness ~ 50 μm) can be fabricated continuously by this method. This method brought a wide tide to raise the cooling rate for fabrications of more tough, and light amorphous alloys.

However, the chill block melt-spinning process developed by Liebermann et al. [36] in

1976 is to quench the melt jet on a high-speed rotating substrate wheel by inert gas, as shown in Fig. 2-5 [36]. This method can largely promote the stability and quality of fabrication processes. Until now, other liquid quenching methods, such as the planner flow casting process, are based on CBMS concept, as shown in Fig. 2-6 [36].

Before 1980, the fabrication methods emphasize on how to increase the cooling rate in avoiding formation of the crystalline phase. However, Inoue et al. [2] develop the Mg-based ternary amorphous alloy by the copper mold casting method in 1991. Bulk metallic glasses of Mg-Cu-Y with 4 mm diameter were successfully synthesized. Addition of the third kind element cooperating with liquid quenching can effectively reduce the critical cooling rate (lower than 10^2 K/s). In 1992 [30], they successfully fabricated bulk metallic glasses with 7 mm in diameter by the high pressure die casting method.

The vapor-solid reactions to form metallic glasses are well known as gas deposition techniques. The multi-component monolayer TFMGs can be fabricated by two methods: (1) co-sputter deposition process, and (2) alloy sputter deposition process, reported by Dudonis et al. [22] and Hata et al. [11], respectively. The quenching processes from vapor to solid are basically similar to that from liquid to solid. With a sufficient cooling rate, the amorphous structure would form by freezing.

Contrary to the quenching processes, solid-state amorphization, e.g. ion-mixing, accumulative rolled bonding, and annealing, provides provide possibility to modify the structure of the specimens, containing bulk and thin-thin specimens. In 1987, Liu [38] predicted the possibility of binary alloy system via ion-mixing. After the bombardment of high-energy particles, crystalline phase would transfer to the amorphous phase. Also, amorphization would form in the immiscible systems, such as Cu-Mo, Y-Mo, and etc, meaning annealing of multilayer thin film provide a different way from quenching processes to form the amorphous alloys [39,40].

2-2 Microstructure of co-sputtered and multilayer alloy thin films

2-2-1 Amorphization in miscible alloy system

Based on the empirical rules of glass forming ability, alloy systems which would form the metastable amorphous phase easily can be predicted. Since 2000, more and more amorphous alloys have been fabricated via the three criteria, such as Zr-Cu-Al [41], Pd-Cu-Si [13], and Mg-Cu-Gd [42], etc. However, sputtering can provide a wider glass forming range and more processes for amorphization. The Zr-Cu alloy system is an example for the demonstration of the routes by co-sputtering and solid-state amorphization. Since the first amorphous alloy has been fabricated, metal-metal binary amorphous alloys have been widely researched, especially for the Zr-Cu system. In addition, many binary systems with negative heat of mixing, such as Au-Ti, Co-Mo, and Al-Pd, etc, can stably exist at the amorphous state [38].

According to Section 2-1-3, the difference of the diffusion mobility would induce the formation of the metastable phase, such as amorphous phase during annealing. For instance, the metastable amorphous Zr_4Cu_3 phase forms in the interface of the Zr/Cu multilayer thin film [43]. As shown in Fig. 2-7, the smooth interfacial layers correspond to the Zr_4Cu_3 amorphous phase which thickness is ~5 nm. The Cu/ZrCu multilayer thin films exhibit a good ductility and high strength due to the interaction between the nanocrystalline Cu layers and the thin amorphous layer.

In 1982, Rivory et al. [44] measured the thermal, electrical, and optical properties of Zr_xCu_{1-x} (0.7 < x < 0.4) TFMGs. A comparison was made between the sputtered and quenched alloys of two compositions $Cu_{50}Zr_{50}$ and $Cu_{30}Zr_{70}$ (in fact $Cu_{33}Zr_{67}$ for the quenched alloy). In terms of the difference of crystallization phenomena, there were several points observed between the sputtered and quenched alloys. The major difference is that the glass transition temperature is vague and not easily to define in the sputtered Zr-Cu glasses. The crystallization temperatures and crystallization enthalpies of the sputtered alloys are presented in Fig. 2-8.

Although the crystallization temperatures are consistent with the results for quenched alloys, the crystallization enthalpies are definitely lower in the sputtered Zr-Cu glasses. The shape of the exothermic peak in the DTA curves is markedly different. The crystallization of the sputtered Zr-Cu glasses occurs over a very wide temperature range, whereas that of the quenched samples occurs over a more narrow range. These differences may be due to the existence of various amorphous states or different free volume content leading to nucleation and crystal growth processes.

2-2-2 Amorphization in immiscible alloy system

As mentioned above, there are three paths to fabricate amorphous alloys. However, the formation of amorphous alloy in immiscible systems is very difficult because of the requirement of the much higher cooling rate. Compared with the miscible alloy systems, the immiscible alloy systems do not contain eutectic reaction in the binary phase diagram. Also, the positive heat of mixing would restrain the mixing of the different atoms. However, the amorphous alloys can still be fabricated by the solid-state reaction. The solid-state reaction, such as ion-mixing [38,45,46] and mechanical alloy [47,48], usually occurs at a relatively much lower temperature than the melting point of each element. It is interesting to explore how the amorphization occurs in the binary immiscible systems. Hence, by constraining the diffusion of atoms, the metastable amorphous would form during the solid-state reactions. In this section, several immiscible binary alloy systems (Cu-Ag, Cu-Ta, and Cu-Nb) are described in Sections 2-2-2-1 to 2-2-2-3.

In these three cases, the phenomena of these three systems are different. The multilayer Cu-Ag thin films do not show the amorphization near the interfaces, and the co-sputtered Cu-Ag thin films exhibit a crystalline solid-solution. For the binary Cu-Ta system, the amorphous Cu-Ta thin films can be fabricated via co-sputtering, and the interfacial amorphization occurs in the Cu-Ta multilayer thin films. In the third case, the amorphous Cu-Nb phase does not form in the interface in the multilayer Cu-Nb multilayer thin films, and the co-sputtered Cu-Nb thin films exhibit the amorphous nature. Although these three systems belong to the immiscible systems, different phenomena would imply the different applications in the three systems. For example, the co-sputtered Cu-Nb thin films can be used in the super-conductive applications [49]; and multilayer Cu-Nb thin films can be used in high-temperature applications [50,51].

2-2-2-1 Amorphization in Ag-Cu system

In the multilayer thin film, annealing would lead to the decrease of the Gibbs free energy by lowering the interface energy between different layers. The system energy may be lowered by reducing the surface area of layer interfaces, grain boundaries and free surfaces; by reducing strain energy from applied or residual stresses; or by reducing the chemical energy in seeking a chemical equilibrium [52]. Knoedler et al. [52] reported the interaction of the Ag-Cu laminate thin film, coated on the Nb substrates thin film. Due to the lack of the inter-diffusion during annealing at 700-900 K, the schemes of the multilayer thin films show that the free-energy level would decrease via the grooves which formed at the grain-boundary/layer-interface junctions in both phases and appeared to pin the grain boundaries and prevented further migration [52]. Figure 2-9(a) and (b) show the as-deposited and annealed films with the laminate structure. After annealing, the smooth interface transfer to the zigzag one to reduce the interface energy.

Due to the positive heat of mixing between Ag and Cu, no inter-diffusion occurs during high-temperature annealing. This occurrence also implies the metastable phase is hard to form in the multilayer setting. However, the free energy of inter-diffusion is a temperature-dependent reaction. In some special cases, such as Cu-Ta, it shows the amorphization near the Cu-Ta interfaces [53], which will be discussed in next sections.

From the aspect of the atomic packing, co-sputtering would provide another structure different from the multilayer Ag-Cu films. A special characteristic of the co-sputtered Ag-Cu thin films is composition-dependent microstructure. Gohil et al. [54] adjusted the deposition factors, such as deposition pressure, power and substrate temperature, to change the microstructure of Ag-Cu thin film. The metastable hexagonal Ag-Cu phase would form under the condition of low substrate temperatures (~100 K) and high working pressures. Atoms can mix homogenously via the co-sputtering because the gas mixing is always spontaneous.

In other words, a shorter mean free path and a lower substrate temperature would limit the surface diffusion of adatoms. Hence, it is reasonable to suggest that the metastable phases, including amorphous or intermediate phases, would form by vapor-quenching. The metastable phase of Ag would form if the particle size is smaller than ~30 nm [55]. According to these reports, co-sputtering can suppress the formation of the stable phase and induce the formation of the metastable phase (nanocrystalline or amorphous phases) by controlling the processing factors.

2-2-2-2 Amorphization in Cu-Ta system

From the aspect of thermodynamic theory, no intermediate phases would form at the equilibrium state in the immiscible binary systems. However, it is not fully applicable for sputtering. In the Cu-Ta system, the observations via experiments and simulations have revealed that the amorphization would occur in the interfaces of the immiscible bi- or multilayered thin films. In 1999, Kwon et al. [53] reported that the amorphous phase formed in the immiscible Cu/Ta interface.

In bulky form of tantalum, the stable phase is α-Ta exhibiting body-centered-cubic (BCC) structure. The Ta film by sputtering usually exhibits a metastable tetragonal phase (β-Ta). The stable BCC Ta structure is obtained either at high temperatures or on specially cleaned silicon substrates. In the literature of Kwon et al. [53], they showed the different phenomena between Cu and α-Ta or β-Ta. Figures 2-10(a) and (b) show the β-Ta/Cu interfacial reaction after annealing at 400^{o}C for 30 minutes. It is noted that different contrasts in the Cu/Ta interface, showing an amorphous-like layer, in Fig. 2-10(a). In the as-deposited film, the interface is chemically abrupt, and the thickness of the amorphous-like layer is about 1.5-2 nm from mark A to the mark B, as shown in Fig. 2-11(a). The dash lines indicate the locations of interfaces observed in high-resolution transmission electron microscopy (HRTEM) graphs. Also, after annealing, the interface amorphous layer becomes clearer and thicker, as shown in Fig. 2-11(b). The thickness of the interface layer is ~4 nm confirmed by the energy-dispersive spectrum (EDS) line profile, shown in Fig. 2-11(b).

Compared with the solid-state amorphization of the Cu-Ta multilayer thin films, Zeng et al. [56] found that the Cu-Ta amorphous alloy can also be fabricated by co-sputtering. The influence of the composition in structure and mechanical properties can be well discussed in this system. As shown in Fig. 2-12, the diffraction pattern means the amorphous humps rightly shift with increasing Ta content. Roughly speaking, the elastic modulus of Cu-Ta amorphous alloy is strongly dependent on the chemical composition. However, one can see that the hardness and elastic modulus vary linearly with the Ta concentration, as presented in Fig. 2-13. The fitted results of hardness and elastic modulus reveal that the variation ratio of the hardness is 0.205 GPa per at% and that of the elastic modulus is 1.35 GPa per at%.

2-2-2-3 Amorphization in Cu-Nb system

In 2005, the self-supported Cu-Nb nanolayered films with individual layer thickness of 75 nm were fabricated by sputtering [57]. The cross-section bright TEM image, as presented in Fig. 2-14(a), shows the columnar nano-sized grains with in-plane dimensions. No porosity was found in the interfaces of Cu and Nb layers, and there is an epitaxial orientation relationship from Cu column to the adjoining Nb column, as shown in Fig. 2-14(b). After annealing at 700^{o}C for 60 hours, the smooth interfaces transfer to the zigzag alignment of the thermally grooved triple joint junctions without changing the thickness of the individual layers in Fig. 2-15. However, the measured hardness of the Cu-Nb multilayered thin films, with the thickness of the individual layer equal to 75 nm, exhibits a small drop after annealing at 700^{o}C for 1 hour, as presented in Fig. 2-16.

Moreover, the measured hardness does not change after 60 hours annealing. In terms of the effect at different annealing temperature, no change is noted up to 500^{o}C, followed by a slight decrease in hardness during the annealing temperatures at 700-800^{o}C, shown in Fig.

2-17. Compared with the 75-nm-thick multilayered Cu-Nb thin films, the 15-nm-thick Cu-Nb thin films exhibit a large drop in hardness upon annealing at temperatures higher than 600^{o}C. The measured hardness even decreases by a factor of two after annealing at 800^{o}C for 30 minutes. The decrease of hardness is caused by the high-temperature annealing which destroys the multilayer structure by adjust the grain boundaries.

In the previous research of the Cu-Nb alloys, Michaelsen et al. [58] reported the thermal properties of Cu-Nb amorphous thin films with different compositions. Figure 2-18 shows the heats of mixing of the liquid/amorphous phase for different temperatures as a function of composition. It can be seen that the heat of mixing of the liquid phase is positive at high temperatures equal to about 20 kJ/g·atom at 2000°C. In contrast, the heat of mixing at a lower temperature is negative about -15 kJ/g·atom. It also means immiscible atoms can attract each other at a lower temperature but can repulse at a higher temperature. Liquid solubility at high temperatures is therefore solely caused by entropy contributions. A decrease of enthalpy and entropy of mixing as a result of the development of chemical short-range order upon undercooling is typical for liquid phases with negative heats of mixing.

However, the heat of mixing of Cu-Nb system changes its sign with decreasing temperature. The thermodynamic calculation on Cu-Nb indicates the heat of mixing is a function of temperature, and the sign of the heat of mixing would change in a specific temperature range. Because of the irregular variation of heat of mixing, the glass-transformation temperature and the crystallization temperature do not depend on the atomic composition.

In the Cu-Nb system, Puthucode et al. [59] reported the early stage of the crystallization of the $Cu_{55}Nb_{45}$ sputtered amorphous thin film which exhibits the interconnected network of

Cu-rich and Nb-rich nano-crystalline domains, as presented in Fig. 2-19. The major difference of the crystallization between the miscible and immiscible alloy systems is the nature of the precipitates. Generally speaking, the precipitates in the miscible alloy systems, such as Zr-Cu-Al [60] and Mg-Cu-Y [61], are the intermetallic compounds, Zr_2Cu and Mg_2Cu, respectively. Contrarily, nano-particles of pure metal would precipitate during the post heat-treatment in the immiscible alloy systems, as shown in Fig. 2-20. Moreover, the nano-particles of pure metal were confirmed via the three-dimensional atom probe (3DAP), as shown in Fig. 2-21.

2-3 Deformation mechanism of amorphous alloys

The deformation mechanism of amorphous alloys is unlike to most of crystalline materials due to the lack of long-range-ordering structure. Compared with the burgers vector as the unit of the dislocation mechanism in crystalline materials, the unit of deformation in amorphous alloys is shear transition zones (STZs). Contrary to critical resolved shear stress (CRSS) in the slip systems, the direction of the shear band usually develops along the largest shear stress. The angle of the shear plane to the loading direction is different under different uniaxial tensile and compressive tests [62].

As bonding in metallic glasses is primarily metallic in character, strain can be readily accommodated at atomic level through changes in neighbors. Compared with electronic ceramics and ionic ceramics, atomic bonds can be broken and reformed at the atomic scale during plastic deformation, dislike the rigidity of bond angles as in a covalent solid, or the balance of charges as in an ionic solid [62]. Therefore, although they usually undergo a strong tendency for shear deformation [63] and macroscopically brittle crack at room temperature, it is not clear that metallic glasses are capable of legitimate plastic flow or softening at the micro-scale or even nano-scale [62,64]. Intrinsic plastic flow on a nano-scale ensures that fluid meniscus instability always occurs in BMGs.

To explain the deformation mechanism in stress-strain curve, a schematically model [65] is illustrated in Fig. 2-22. Serrated flow can be understood as an alternating process of stress- and, as shown above, temperature-assisted shearing of atomic volumes such as (STZs) and a diffusive type of structural relaxation of these sheared volumes. With reference to the free volume model, the first process described is understood as a mechanism where free volume is generated (work softening), while in the second process free volume is annihilated (time-dependent hardening). While the shear of a single STZ is assumed to be of the order of Angstroms, serrated flow can be correlated with shear offsets of several hundred nanometers.

During deformation, a cooperative process combines the nucleation and considerable initiation of STZs, which adds up to submicrometer large shear offsets and macroscopically results in shear bands with a different structure than the bulk. As described in Fig. 2-22, the stress-strain curve is divided into six stages, marked by ① to ⑥. After sufficient energy is provided for dilatation and generation of free volume a stress-assisted, thermally driven process in a shear transition zone (① ② ③) and shear propagation (④) can be initialized. This process results in a stress release, plastic strain (shear band offset) and consequently the arrest of the disorder structure (⑤).

The second process triggers the annihilation of freshly free volume and therefore causes a time-dependent hardening of the area in the vicinity of the shear band. The waiting time t_{rel} between one and the next serration causes the alternated structure, or macroscopically speaking the shear band to recover and relax (⑥) to a lower energy state (i.e. higher density due to free volume annihilation) similarly as has been described in [66]. The rates of these counteracting processes lead to a positive net generation of free volume with increasing strain. Assuming a sudden decrease in the applied strain rate, more time is available for the relaxation to occur between successive stress drops.

This time allows for the sheared zone to annihilate some of the freshly produced free volume. This in-turn leads to a strengthening of the deformed zone or macroscopically speaking to a higher stress resistance against flow. Consequently, a higher flow stress results at lower applied strain rates exhibiting negative strain rate sensitivity.

2-4 Mechanical properties of thin film metallic glasses

2-4-1 Nanoindentation and microindentation

As mentioned in Sections 2-3, the deformation mechanism of amorphous alloys is different from the crystalline materials due to the lack of defects, such as dislocations. In indentation tests of crystalline materials, we can observe the pop-in events, causing by the phase transformation [67] and dislocation emission [68-70]. For amorphous alloys, the results also show the pop-in events during loading segments [71]. However, it does not come from the phase transformation or dislocation emission but shear bands nucleation and propagation [72].

The free-volume model describing the deformation mechanism of amorphous alloys is accepted by most researchers. In typical amorphous alloys, the pop-in events are not related to phase transformation but the propagation of shear bands. In Fig. 2-23(a), a typical load-displacement curve for the amorphous alloys, showing the steps or “pop-in” events during loading. The “pop-in” events usually corresponding to the increment dh_s is the depth of a step (‘pop-in’).

The steeper portion of the loading curve preceding a step shows the elastic response between the operation of shear bands and has the increment dh_e. The total depth increment from step to step along an ideal plastic curve is ($dh_p = dh_e + dh_s$) The unloading curve reflects the elastic behavior of the material [73]. Figure 2-23(a) shows that the elastic portions (dh_e) on loading are indeed parallel to the unloading curve at similar loads. Also the trace around the indentation marks is the path which shear bands pass through, as shown in Fig. 2-23(b).

As we know, the amorphous alloys with a low glass-forming ability, such as Ag-Ni and Cu-Nb, can only be fabricated by vapor quenching processes. However, the traditional mechanical tests, such as compressive and tensile tests are not suitable for thin-film types. The nanoindentation gradually becomes a powerful tool to measure the mechanical properties of these kinds of TFMGs. In 2007, Zong et al. [74] reported the relationship between the composition variation and the mechanical properties in the Cu-W system. First of all, they fabricated the Cu_xW_{1-x} (x is equal to 0, 7, 21, 36, 41, 60, 66, 71, 75, 86, and 100 at%) thin film via alloy-sputtering.

The diffraction patterns of the alloys from 36 at% to 75 at% Cu exhibit a broadening hump, corresponding to the amorphous structure. Also, the $Cu_{21}W_{79}$ film forms BCC W (Cu) solid solution, and the $Cu_{86}W_{14}$ film forms FCC Cu (W) solid solution.

Typical nanoindentation load-displacement (P-h) curves are presented in Fig. 2-24. For clarity, only the loading portions are shown and the curves are shifted. Figure 2-24(a) is the P-h curves for the $Cu_{36}W_{64}$ amorphous alloy at various strain rates. At a lower strain rate (0.05 s^{-1}), the P-h curve is punctuated by many discrete bursts (labeled A, B, C, D and E) of rapid displacement at nearly constant load, which are called pop-in events. When the strain rate increases to 0.2 s^{-1}, the curve only shows two faint pop-in events (labeled F and G). Increasing the strain rate further to 1 s^{-1}, the curve is smooth and no pop-in could be found. This indicates that its deformation behavior is obviously dependent on the indentation strain rate. Figure 2-24(b) is the P-h curves for the $Cu_{60}W_{40}$ amorphous alloy at various strain rates.

It can be seen that its deformation behavior is also influenced by the strain rate. At 0.05 s^{-1}, the P-h curve exhibits serrated flow (labeled H and I). While at 0.2 s^{-1} and 1 s^{-1}, the curves are smooth. For the $Cu_{71}W_{29}$ amorphous alloy, all the P-h curves (not shown) do not show any pop-in events. This suggests that the deformation behavior of the Cu-W amorphous alloy is dependent on not only the strain rate but also the chemical composition.

In their work, the elastic modulus and hardness of the Cu-W thin films strongly depend on the chemical composition. Moreover, it is interesting that the indentation marks, shown in Fig. 2-25, exhibits the distinct morphology with the variation of the chemical compositions. From Figs. 2-25(a) to (d), the corresponding structure of the $Cu_{21}W_{79}$ thin films are the BCC solid solution, exhibit no pop-in events during the indentation and no marks of the initiation of the shear bands. With increasing Cu content, the nature gradually transfers to amorphous phase from solid solution, inducing the pop-in events during indentation.

2-4-2 Microcompression tests

Facing on the smaller and smaller size of the device, it is necessary to understand the mechanical properties in micro- or even nano-scale. In addition to nanoindentation, two methods, microcompression and microtensile tests are developed. Microcompression and microtensile tests belong to the mechanical test along uniaxial axis with tensile or compressive stress, respectively. The nanoindentation, complex two-dimension stress field leads to the difficulty in analyzing the deformation characteristics. The mechanical response of the micro-scale specimen under tensile or compressive mode is easier to analyzing the deformation phenomena. In this section, the topic is focused on the microcompression test. First of all, to avoid the effect of the artifact, how to fabricate the microcompression specimen is the key point. Up to now, there are two major methods:

(a) Focus-ion-beam method, which can develop the micropillar of any material with any configuration by selective etching.

(b) Lithography method, which can produce a large quantity of the micropillars but depend on its parameters during fabrication.

In terms of method (a), the micro-sample fabrication methodology is based on FIB milling (highly localized ion sputtering using energetic ions) to micro-machine small compression samples from the surface of a bulk crystal. Focused-ion-beam systems are uniquely suited in their ability to fabricate 3D structures while maintaining sub-micron precision in a variety of metallic and non-metallic systems [75,76]. A FEI company strata dual beam 235 was used for this study, and the FIB column on this instrument supplies 30 kV Ga^+ ions at beam currents ranging from 0.001 to 20 nA. The micro-sample fabrication process begins with the preparation of the bulk material of interest. A small section of a bulk material is prepared using standard metallographic methods, so that the section can be placed on a standard scanning electron microscope (SEM).

Typically the bulk section is mechanically polished using an automated lapping machine (Allied High-Tech Multi-Prep System) to produce a parallel-sided sample, subsequently electro-polished to remove any residual damage from the mechanical polishing. The sample is then mounted to a SEM stub using silver-based conductive paste or epoxy. The microcompression sample preparation process consists of two steps. First, the surface of the bulk section is oriented normal to the FIB column, and an area of interest is located using FIB imaging.

In that area a series of concentric annular milling patterns are used to mill a cavity or crater that creates each sample blank in relief. The large cavity serves the following purposes: (i) allows one to image the sidewalls of the micro-sample both before and after deformation using the SEM or FIB (which is necessary for subsequent fabrication steps), (ii) ensures that the flat indenter tip does not contact any other surfaces than the micro-sample, (iii) lessens the probability that sputtered material will redeposit back onto the freshly milled micro-sample during subsequent fabrication steps, and (iv) facilitates locating the micro-sample using the optical microscope of the nanoindenter test system. Note that this step is usually performed using high-beam currents (20-5 nA), since the goal is to quickly remove material from around the sample volume of interest. For example, the time required to mill the cavity for the 5 μm diameter pure Ni sample shown in Fig. 2-26 was approximately 240 min using a 5 nA beam. This time could be shortened considerably by changing to an even higher beam current, as a 20 nA beam current could machine this same structure in one-fourth of the time.

However, one must be careful when using the highest beam currents since the spot size and lateral spread of the ion beam increases dramatically. This must be taken into account when defining a specific milling pattern, or one risks accidentally milling into the area of interest. Also note that the time required to mill the cavity increases directly in proportion to the volume of material removed. This can present problems in terms of the overall time required to machine samples that are equal to or larger than 20 μm in diameter. For instance, this step in the fabrication process requires at least 16 h for a 20 μm diameter sample in pure Ni (using a 20 nA beam current). Two examples of micro-samples machined using this fabrication methodology are shown in Fig. 2-27, and it is clear from this figure that the dimensional form of the micro-samples can be carefully controlled over a wide range of sizes.

In addition of the focus-ion-beam method, the micropillars are also fabricated by other methods. In 2007, Bei and George [77] reported that the Mo alloy micropillars fabricated by lithographic method. Though the technique, the micropillar array can be easily fabricated. The micropillars were produced by etching away the NiAl matrix of a NiAl-Mo in situ composite grown by directional solidification (Fig. 2-28).

Details of the directional solidification process and the resulting composite microstructures have been discussed elsewhere [77,78]. The composite consists of monocrystalline Mo solid-solution fibers (composition, 86Mo-10Al-4Ni, at%) with axes parallel to (100) embedded in a NiAl matrix (composition, 55Ni-45Al, at%) [77].

Examples of P-h curves obtained from good compression tests on the four different size pillars are shown in Fig. 2-29(a). The reproducible P-h curves are initially linear elastic but, upon reaching a critical load. The cross-sectional area of the fibers, which varies inversely as the directional solidification rate, was measured from scanning electron microscope (SEM) images using image-analysis software. Because of their nearly square cross-sections (Fig. 2-29(b) to (d)), the fiber (or pillar) size is taken to be the square root of the measured cross-sectional area. The pillar sizes in this study ranged from 360 to 1000 nm. The magnitude of the displacement burst corresponds well to the height of the pillar (the pillars had aspect ratios in the range 2.5-3.0), confirming that once plasticity commences, it continues catastrophically and unstably until the pillar is fully compressed. Since the tests were conducted in load control at a constant loading rate, the instability suggests that there is significant strain softening after yielding, as was observed by Brenner in his micro-whisker tests [79,80]. Quantification of the strain softening behavior would require a displacement-controlled test. Yield strengths for the valid tests computed from measured loads at yielding and initial cross-sectional areas are summarized in Table 2-1 [78] .

Curiously, the average yield strength is independent of pillar size at a value near 9.2 GPa. The slip systems in Mo are (110)$[1\bar{1}1]$ and (112)$[11\bar{1}]$ [81], which for our compression geometry yields Schmid factors of 0.41 and 0.47. Assuming that slip occurs on the slip system with the higher Schmid factor, the critical resolved shear stress at yielding is equal to 4.3 GPa. The shear modulus of Mo is 126 GPa [82], but assuming that alloying with Al and Ni lowers this according to a rule of mixtures based on their respective atomic percentages, G for our micropillars should be approximately 112 GPa. Thus, the measured resolved shear stress at yielding is approximately G/26 and therefore within the range expected for the theoretical strength (G/30 to G/10) [79,83]. This large critical resolved shear stress suggests that their micropillars are essentially dislocation-free before testing, consistent with transmission electron microscopy observations of NiAl-Mo eutectics [76], and that yielding occurs when dislocations are nucleated at the theoretical shear strength, similar to Brenner's whisker tests.

This conclusion is further corroborated by the fact that yield strength is independent of sample size. The fact that there is an intense burst of plasticity after yielding indicates that dislocation multiplication is rapid and widespread and that dislocation starvation does not occur in any of the specimens after yielding. These results are consistent with the view that well-annealed metals, which have dislocation densities in the range 10^7-10^{11} m^{-2} [84], should behave as ideal metals (i.e. have yield strengths approaching the theoretical strength) when their sizes are ~1 μm or smaller. It is surprising, therefore, that no other micropillar tests performed to date have observed such high yield stresses, even though some of the pillars were of appropriate dimensions (~1 μm or smaller).

Possible reasons for the lower stresses measured in the previous studies include the generation of small dislocation loops and vacancies during FIB milling, and additional internal stresses from the implanted gallium ions due to the size difference between gallium and the host lattice. Although a size effect on yield stress was not observed in the present study, the current results do not rule out a size effect on the flow stress if stable deformation after yielding could be achieved through a displacement-controlled test.

In 2008, Lai et al. [85] observed the relationship between the compressive strength and the pillar size. Figure 2-30 shows the different appearance of the Zr-based micropillars in 3.8 μm, 1 μm, and 700 nm after compression. The representative engineering stress-strain curves are shown in Fig. 2-31. The deformation mode of these micropillars is invariably the localized shear banding, independent of the specimen size. From Fig. 2-30, we can observe that sample shear-off does not occur immediately. Also, the compressive stress increases with decreasing pillar size, as shown in Table 2-2.

2-5 Toughness of metallic glasses

2-5-1 Intrinsic strengthening

Metallic glasses exhibit a high fracture strength, like oxide ceramic materials, and exhibit some ductility, like metallic or alloy materials. In 2005, Lewandowski et al. [86] brought up an idea to identify the ductility of metallic glasses. The value of μ/B, where μ and B are the shear modulus and bulk modulus, respectively, is typically about two-thirds of the value for the polycrystalline pure metal on which it is based.

The glasses might therefore be expected to show more plasticity, but this is offset by the shift in value of $(\mu/B)_{crit}$ which divides plasticity and brittle fracture. For metallic glasses (Fig. 2-32) $(\mu/B)_{crit}$ is in the range 0.41-0.43, where there is a large drop in shear modulus (G) with increasing μ/B, and G approaches the toughness of oxide glasses. This is lower than the range of values for $(\mu/B)_{crit}$ reported earlier for polycrystalline pure metals. Overall, it would appear that glassy alloys are slightly more likely than their crystalline counterparts to show brittle behavior. The correlation between fracture energy and elastic constants can also be expressed in terms of Poisson's ratio (ν). Higher values of ν give higher fracture energy, the transition between brittle and tough regimes at the region for ν_{crit}=0.31-0.32, observing a large increase in G, as shown in Fig. 2-33.

The factor, μ/B, was announced to describe the ductility of the metallic glass, which concept is like crystalline materials. The data on the as-cast metallic glasses, plotted in Fig. 2-32, show a clear correlation between fracture energy G and μ/B. With low values of μ/B, the glasses based on Pd, Zr, Cu or Pt, all have fracture energies well in excess of 1 kJm^{-2}, exhibit extensive shear banding, and have vein-pattern fracture surfaces. With high μ/B the magnesium-based glass approaches the ideal brittle behavior (G~1 Jm^{-2}) associated with oxide glasses. Recent reports of the platinum-based glasses with low μ/B and exceptionally high toughness and malleability fit well on the same correlation. This correlation between G and μ/B is similar to that discussed earlier for crystalline metals [86].

2-5-2 Extrinsic strengthening

As mentioned above, amorphous alloys via intrinsic strengthening is not the remarkable effect due to the amorphous nature. Moreover, extrinsic strengthening is another potential way to improve the mechanical properties. Considering the choice of reinforcement, the important key is avoiding the occurrence of chemical reaction between the matrix and the reinforcement. In 1998, Conner et al. [87] successfully fabricated the bulk metallic glass composites (BMGCs), as shown in Fig. 2-34. In this case, the authors selected the Zr-based amorphous alloy, serving the matrix, corresponding to the white contract. The tungsten and 1080 steel fibers (~50 μm) were selected as the reinforcement, corresponding to the black contract. The side view shows clearly that the fibers split longitudinally and buckled. Note that the cracks on the compression face run toward and through the tungsten wires. This is expected for the tungsten composite, because cooling leaves the residual tensile stress in the matrix.

In compression test of the Zr-based/steel or tungsten fiber BMGCs, the stress-strain curve exhibits a significant improvement of ductility, as shown in Fig. 2-35 [87]. It is proposed that the fibers first yield, followed by axial shear cracking, which makes the fibers unstable and unable to prevent buckling in the composite. Both have the same ultimate strength, though the tungsten strain to failure (18%) is substantially larger than that of the steel (6%). This shows that the compressive strength of the composite is controlled by the matrix. Unlike the perfectly-plastic tungsten composite, the inelastic portion of the stress-strain curve for the steel wire reinforced composite shows some work hardening.

Contrary to the amorphous alloy with the fiber-type reinforcement, the porous-particle-strengthening would improve the plastic strain up to ~7% engineering strain, as presented in Fig. 2-36 [88]. In the stress-strain curves, the plastic strain increases with increasing the porous Mo content. From the aspect of microstructure of the Mg-based BMG with Mo reinforcement, it shows two kinds of microstructures in different scales. One is that the Mo micro-size particles are embedded in the amorphous matrix; another is that the amorphous regions in nano-scale are embedded in the porous Mo particles. As shown in Fig. 2-37, the deformation morphology shows the Mo particles can effectively absorb shear bands and suppress the growth of crack, inducing a drastic plastic strain [88].

Chapter 3 Experimental Procedures

In this study, three kinds of TFMGs or nanolaminate composites are fabricated via sputtering. Providing the wide glass forming range, three different approaches are tried to tough TFMGs, listed below:

(1) Strengthening of TFMGs by structure relaxation of Zr-Cu-Ti fully amorphous TFMGs via sub-T_g annealing,

(2) Strengthening of TFMGs by addition of immiscible tantalum to form possible liquid phase separation or precipitated crystalline phases,

(3) Strengthening of TFMGs by multilayer thin films design for the Zr-Cu-Ti/Ta thin film nanocomposites.

The flow chart is shown in Fig. 3-1. In this chart, how to tough TFMGs and to estimate the relative properties, such as elastic modulus and hardness is first focused. Through the change of the composition and introduction of the crystalline layers, these different effects in mechanical properties can be understood. The methods will help to determine which approach mentioned above has the potential to enhance ductility. The ductility is verified by the microcompression tests.

3-1 Materials

The Zr, Cu, Ti, and Ta metallic targets used in this study were purchased from Well Being Enterprise Co., Ltd, Taipei, Taiwan. The purity levels of the Zr, Cu, Ti, and Ta targets are 99.9%, 99.999%, 99.99%, and 99.9%, respectively. To simplify the deposition variation, the ZrCuTi alloy target, where the composition is $Zr_{65}Cu_{25}Ti_{10}$ in wt%, is used in multi-component co-sputtering. The purity of the Zr-Cu-Ti alloy target is 99.9%.

3-2 Alloy Designation

In this study, the alloy systems are focused on the ZrCu based systems. By controlling the sputtering factors, the specimens can be divided to several groups:

(1) Zr-rich Zr-Cu systems,

(2) Zr-Cu-Ti systems,

(3) Zr-Cu-Ti-Ta systems,

(4) Multilayer Zr-Cu-Ti/Ta systems.

This design is from simple binary to complex multi-component systems. For the sputtering process, it provides a high cooling rate and a wide glass-forming range. Especially for the low GFA alloy systems, it is possible to fabricate these systems by sputtering.

First of all, Tang et al. [89] and Dudonis et al. [22] bring up a concept about the instability of the metallic materials by co-sputtering. The glass forming range of Zr-Cu system is from 4 to 96 at% of Cu. From the aspect of ductility, Kwon et al. indicate that a higher Zr content would lead to better ductility [90]. Combining the ideas mentioned above, the Zr-rich ZrCu would be a good candidate for good mechanical properties. As shown in Fig. 3-2, the chosen $Zr_{69}Cu_{31}$ is close to the eutectic point at $Cu_{27.6}Zr_{72.4}$. Moreover, the Ti substitution for Zr is to improve the adhesion to the Si substrates and to analyze the mechanical response during nanoindentation tests. In addition, Ti effect can enhance the thermal stability of the amorphous alloys [91]. To understand the phenomena of the structural relaxation, the Zr-rich Zr-Cu and Zr-Cu-Ti specimens are simpler because the equilibrium phase is the mixture of (Zr,Ti)Cu and Zr-Ti solid solution in the Zr-Cu-Ti ternary phase diagram at 703°C, as shown in Fig. 3-3.

As mentioned in Section 1-4, the addition of the immiscible element is another approach to strength the amorphous alloys. According to the binary phase diagrams of Zr-Ta, Cu-Ta, and Ti-Ta (Figs. 3-4(a) to (c)), it shows these systems all do not contain any intermetallic compound. Moreover, the immiscible tantalum is supposed to change the amorphous nature or the atomic packing. Hence, the Zr-Cu-Ti-Ta TFMGs are fabricated by adjusting the power of the Zr-Cu-Ti and Ta guns. Another multilayer system is composed by the Zr-Cu-Ti and Ta layers for comparison, which deposited alternatively with the thickness of 50 nm/50 nm and 50 nm/5 nm, respectively.

3-3 Sample preparation

3-3-1 Substrate preparation

In this experiment, films are deposited on the P-type (100) silicon wafer. In order to avoid some other impurities and greasy dirt adhering to the substrates, the following surface cleaning procedures were adopted.

(1) With deionized (DI) water, an ultrasonic cleaner is used to clean the substrates for 10 minutes to remove the dust and impurities on the surface of substrate.

(2) An ultrasonic cleaner is used to clean the substrates in alcohol for 10 minutes to remove the greasy on the surface of substrate.

(3) After rinsing in alcohol, an ultrasonic cleaner is used to clean it in acetone for 10 minutes.

(4) After rinsing in acetone, an ultrasonic cleaner is used to clean it in DI water for 10 minutes.

(5) Air was use to dry the substrates.

3-3-2 Thin film preparation

In this study, monolayer and multilayer thin films were prepared by magnetron sputtering with a target of 50.8 mm in diameter at a working pressure of 3×10^{-3} torr. There were five kinds of procedures listed below:

(1) Zr-Cu monolayer thin films using co-sputtering,

(2) Zr-Cu-Ti monolayer thin films using co-sputtering,

(3) Zr-Cu-Ti monolayer thin films using alloy sputtering,

(4) Zr-Cu-Ti-Ta monolayer thin films using co-sputtering,

(5) Multilayer thin films composing of alternative Zr-Cu-Ti and Ta layers with different thicknesses equal to 50 nm/50 nm and 50 nm/5 nm.

The Zr-Cu and Zr-Cu-Ti films can be fabricated using the co-sputtering deposition process with zirconium, copper, and titanium targets. A rotary pump was used to achieve mediate vacuum, and a cryo-pump was used to achieve a base pressure less than 1×10^{-6} torr. The base pressure maintains below $5\mathrm{x}10^{-7}$ torr. There was a load-lock chamber, for quick and convenient exchanging of substrates without venting the main chamber. After achieving the base pressure, Ar was introduced into the chamber, and targets were pre-sputtered by inserting a movable shutter for five minutes. For the $Zr_{69}Cu_{31}$ (at%) films, the Zr target was set up on the DC cathode with 305 W, and the copper target was set up on the DC cathode with 50 W, respectively. The substrate is set on the sample holder, with a substrate-to-cathode distance of ~100 mm. The working gas was pure argon. The argon flow rate was fixed at 30 standard cubic centimeters per minute (sccm). During deposition, the substrate was rotated with an average speed of 15 rpm for the uniform distribution of the film thickness. The process of the $Zr_{52}Cu_{29}Ti_{19}$ thin film is similar to $Zr_{69}Cu_{31}$. The deposition condition is set at

DC Zr 250 W, DC Cu 200, and RF Ti 140 W.

The films were fabricated by the co-sputtering with the $Zr_{65}Cu_{25}Ti_{10}$ in wt% alloy target and the pure Ta target, which were both set on the direct current (DC) cathodes. The purity of $Zr_{65}Cu_{25}Ti_{10}$ and Ta target is 99.9% and 99.95%, respectively. Before processing, the base pressure of the chamber is at 5 x 10^{-7} torr or greater. The ZrCuTi-rich films were fabricated at a fixed power of 300 W for the ZrCuTi cathode and various powers of 50, 100, 200 and 300 W for the Ta cathode, resulting in increasing Ta content. To reach the high Ta content greater than ~50 at%, the Ta-rich films were fabricated at a fixed power of 300 W for Ta and the decreasing powers of 200, 150, 100 and 50 W for ZrCuTi. The ZrCuTi alloy films without Ta and pure Ta thin films were also prepared for comparison. The thickness of all as-deposited ZrCuTiTa alloy thin films lies within 2~3 μm.

Two different Zr-Cu-Ti/Ta multilayer thin films were fabricated with the thickness of Zr-Cu-Ti and Ta individual layer equal to 50 nm/50 nm and 50 nm/5 nm, respectively. The details of the monolayer and multilayer sputtering conditions are summarized in Table 3-1. During deposition, the substrate was rotated with an average speed of 15 rpm for the uniform distribution of the film thickness.

3-3-3 Post-treatment of the as-deposited ZrCu and ZrCuTi samples

The post-treatment is used in the route of the structural relaxation. In this study, the $Zr_{69}Cu_{31}$ and $Zr_{52}Cu_{29}Ti_{19}$ TFMGs are discussed in the influence of the sub-T_g annealing. First, the specimens are set in the rapid thermal annealing (RTA) system. The mechanical pump starts to lower the chamber pressure to $8x10^{-2}$ torr. Thus, the chamber pressure is reduced below $1x10^{-3}$ torr and remains for 30 minutes to ensure the clearance of the chamber.

The annealing route of $Zr_{69}Cu_{31}$, named as ZC, and $Zr_{52}Cu_{29}Ti_{19}$, named as ZCT, TFMGs is shown in Fig. 3-5. First, stages I and II are the heating stage with a slow heating rate and the holding stage to stabilize the atmosphere and remove the residual vapor. Then, the specimens are heated with the heating rate of 2 K/s and hold at 200°C or 473 K (~$0.8T_g$) in stage III. Then, stage IV is the holding stage for the annealing. The duration time is for 15 minutes. Repeat the annealing process four times to reach the target of the annealing time, equal to 60 minutes. The annealed specimens of $Zr_{69}Cu_{31}$ and $Zr_{52}Cu_{29}Ti_{19}$ are named as ZC200 and ZCT200, respectively. Similarly, the ZrCuTi TFMGs are annealed at 290°C or 563 K (~$0.95T_g$) for 60 minutes. The annealed specimens of $Zr_{52}Cu_{29}Ti_{19}$ at 290°C are named as ZCT290. After the end of the annealing process, the specimens are taken out until the temperature of the specimens is below 323 K.

3-4 Property measurements and analysis

3-4-1 X-ray diffraction

The nature of the thin film fabricated by the magnetic sputtering deposition is examined by X-ray diffraction (XRD). The SIEMENS D5000 X-ray diffractometer with Cu K_α radiation (λ = 1.5406 Å), operated at 40 kV and 30 mA, and equipped with 0.02 mm graphite monochrometer, is utilized. The ranges of the diffraction angle 2θ of the specimens were within 20° to 60°, respectively, at the scanning rate of 0.0083 °/s.

3-4-2 Qualitative and quantitative constituent analysis

In order to identify the constituent component and confirm the composition percentage of the binary metallic thin films, the samples are characterized by a Joel 6330 scanning electron microscopy (SEM) with energy dispersive X-ray spectrometry (EDS). The film surface is selected to examine the quantity of the designed compositions by EDS. By using the electron beams at 10 kV, the composition of each sample is averaged by 10 measurements. which standard error is ~5 at%.

3-4-3 Thermal analysis using differential scanning calorimetry

The Perkin Elmer, Pyris Diamond DSC is used for thermal analysis to determine the temperature of the phase transformation. The as-deposited films are first peeled off, avoiding the effect of the substrate. For the Cu containers of reference and sample, the thermal history between them was removed by using annealing. In DSC analysis, for the non-isothermal heating course, the Zr-Cu-Ti thin films are heated to 823 K at the heating rate of 10 K/min.

3-4-4 Plan-view TEM analysis

To understand the microstructure of as-deposited metallic thin film, plane-view TEM specimens are prepared via ion-thinning technique (GATAN PIPS-691 Ion-Miller). Then, to prepare the plane-view TEM specimen, as-deposited thin films are bound on a 3-mm Mo slot grid and thinned until the thickness is lower than 100 nm via an ion miller below 3 keV. Finally, the plane-view specimens are examined using the JOEL 3010 analytical scanning transmission electron microscope (AEM) at 300 kV and FEI E.O Tecnai F20 G2 Field-Emission TEM at 200 kV.

3-4-5 Mechanical tests in micro-scale

3-4-5-1 Measurement of elastic modulus and hardness via nanoindentation

The MTS XP nanoindenter is used to evaluate the nanomechanical properties of a series of the Zr-based TFMGs coated on the Si (001) wafer with the thickness equal to 2~3 μm. During the process of indentation, the deeper penetration depth, the higher effect of the substrate. Generally speaking, the examined mechanical properties without the substrate effect were tested within about 10% thickness of the film. Hence, the Zr-based TFMGs with the Si substrate were tested by the nanoindenter operated in the loading-rate-control mode. In this mode, indentation without applied frequency would trace the mechanical response from indentation deformation. In this study, the as-deposited thin film would are indented up to the maximum load equal to 5 mN at 0.01, 0.05, 0.1, 0.5, 1 and 5 mN/s. The peak holding time is equal to 30 seconds. Every condition would test 10 times to get the reliable data.

3-4-5-2 Microcompression test

The micropillar specimens of $Zr_{52}Cu_{29}Ti_{19}$, $Zr_{45}Cu_{27}Ti_{15}Ta_{13}$, $Zr_{31}Cu_{15}Ti_{10}Ta_{44}$, $Zr_{14}Cu_{7}Ti_{5}Ta_{74}$, $Zr_{55}Cu_{31}Ti_{14}$ 50 nm/ Ta50 nm, and $Zr_{55}Cu_{31}Ti_{14}$ 50 nm/Ta 5 nm were prepared via dual-beam focus ion beam (FIB) system (Seiko, SMI3050 SE). The top diameter and height of $Zr_{52}Cu_{29}Ti_{19}$, $Zr_{45}Cu_{27}Ti_{15}Ta_{13}$, $Zr_{31}Cu_{15}Ti_{10}Ta_{44}$, $Zr_{14}Cu_{7}Ti_{5}Ta_{74}$, micropillar is ~900 nm and ~2000 nm, respectively. The micropillar $Zr_{55}Cu_{31}Ti_{14}$ 50 nm/Ta 50 nm, and $Zr_{55}Cu_{31}Ti_{14}$ 50 nm/Ta 5 nm is ~900 nm in diameter rand ~1500 nm in height. The microcompression tests were performed at MTS Nanoindenter XP system with a flat-end Berkovich tip. The shape is equilateral triangle with the 13.5 μm in each side.

All tests are performed at loading rate control mode using 2-cyclc test. In this test, the micropillar was tested at the load function, as shown in Fig. 3-6. The values of the loading time (Δt_1,Δt_3, Δt_4, and Δt_6) are the same. The holding time at the first and second peak load (Δt_2 and Δt_5) are both set as 60 seconds. The first peak load (P_1) is half to the second peak load (P_3), and P_2 is 1/10 of P_1. To determine the peak load, the yield stress is roughly equal to H/3 using Von Mises yield criterion. In the case of $Zr_{52}Cu_{29}Ti_{19}$, $Zr_{45}Cu_{27}Ti_{15}Ta_{13}$, $Zr_{31}Cu_{15}Ti_{10}Ta_{44}$, and $Zr_{55}Cu_{31}Ti_{14}$ 50 nm/Ta 5 nm, the values of P_2 and Δt_1 are 2 mN and 120 seconds. In the case of $Zr_{55}Cu_{31}Ti_{14}$ 50 nm/Ta 50 nm and $Zr_{14}Cu_7Ti_5Ta_{74}$, the values of P_2 and Δt_1 are 3 mN and 180 seconds. Thus, the peak load in the microcompression of nanocrystalline Ta pillars is set at 4 mN. The testing conditions are all listed in Table 3-2.

Considering the deformation characteristics in the $Zr_{55}Cu_{31}Ti_{14}$ 50 nm/Ta 50 nm nanolaminate system is more complex than the condition in the monolithic TFMG, one more test at 2.5 mN was performed to understand the deformation process in detail. The loading rate at 2.5 mN is equal to 0.0163 mNs^{-1} close to the test at 3 mN.

Chapter 4 Results

4-1 Sub-T_g annealing of Zr-based TFMGs

The effect of annealing on mechanical behaviors has been studied. Many researchers found that annealed amorphous alloys become more brittle [92-95] by the precipitation of the intermetallic compounds or the structural relaxation. The embrittlement characteristic causes some critical concern for the potential applications. Here, we would like to use the nanoindentation technique to analyses the relationship between the mechanical behaviors and sub-T_g annealing.

4-1-1 Structural of ZrCu and ZrCuTi TFMGs

4-1-1-1 SEM/EDS analysis of ZrCu and ZrCuTi TFMGs

Quantity analysis of as-deposited ZrCu and ZrCuTi thin films was performed using SEM/EDS at low magnifications. As shown in Figs. 4-1(a) and (b), the surfaces of ZrCu and ZrCuTi are plane and smooth. The compositions of the two thin films were measured by collect at least 50 μm x 50 μm. In average, the ZrCu thin films are composed by 69 at% Zr and 31 at% Cu; and the ZrCuTi thin films are composed by 52 at% Zr, 29 at% Cu and 19% Ti.

4-1-1-2 XRD analysis of ZrCu and ZrCuTi TFMGs

In Table 4-1, the basic properties of Zr, Cu, and Ti are listed. Zr is the element with the largest atomic radius. The middle is Ti, and the smallest element is Cu [96]. The difference in Zr-Cu, Ti-Cu, and Zr-Ti are ~24%, ~15%, ~8%, respectively. Moreover, Table 4-2 lists the heat of mixing (ΔH_{mix}) of the Zr-Cu, Ti-Cu and Zr-Ti system, equal to -23, -9, and 0 kJ/mol [97]. According to the empirical rule for the fabrication of amorphous alloys [7], the ZrCuTi amorphous alloys are expected to be produced. The co-sputtered Zr-based thin films, including $Zr_{69}Cu_{31}$ and $Zr_{52}Cu_{29}Ti_{19}$, were characterized by XRD. As shown in Fig. 4-2, the broadened humps of the two samples indicate the formation of amorphous phase. To simplify the process, the ZrCuTi thin film metallic glasses were also successfully fabricated via alloy sputtering using pre-alloyed targets. The composition difference between the as-fabricated ZrCuTi via co-sputtering and alloy sputtering is smaller than 5 at%. The corresponding diffraction patterns of the two ZrCuTi specimens are shown in Fig. 4-3, indicating the similar amorphous characteristics. This means that the structural characteristic is insensitive to the deposition process.

4-1-2 Influence of hysteresis effect on mechanical properties of Zr-based TFMGs

Through nanoindentation tests, the basic information, including elastic modulus and hardness, can be obtained. According to the research of Oliver and Pharr [98], an indentation test is composed of three parts: loading, holding and unloading segments. The displacement of the loading segment is attributed to the elastic and plastic deformation. The holding segment is caused by the time-dependent deformation of the materials. The unloading segment is attributed to the elastic recovery.

The relationship between the indentation depth (h) and the projection indentation area (A(h)) can be expressed by the following equation:

$$A(h) = a_0h^2 + a_1h + a_2h^{1/2} + a_3h^{1/4} + a_4h^{1/8}, \quad (4\text{-}1)$$

where a_0 to a_4 are constants. For perfect Berkovich tips, the value of a_0 is 24.5. In reality, the value of a_0 would be slightly different for various tips. The values of a_1 to a_4 are determined via the elastic modulus calibration of standard fused silica. To determine the elastic modulus of the test materials, the reduced elastic modulus (E_r) can be calculated by the following equation.

$$E_r = \frac{1}{\beta}\frac{\sqrt{\pi}}{2}\frac{S}{\sqrt{A_c}}, \quad (4\text{-}2)$$

where β is equal to 1.034 for a Berkovich tip. A_c and S are the contact area of indentation mark, which is corrected by the elastic recovery, and the unloading stiffness, respectively. According to Oliver and Pharr [98], the unloading curve can be expressed as a power-law equation,

$$P = B(h - h_f)^m, \quad (4\text{-}3)$$

where P is the applied load, h is the displacement, B and m are empirically determined fitting parameters, and h_f is the final displacement after complete unloading (also determined by curve fitting). Thus, the unloading stiffness (S) is can be established through the differentiation of Eq. 4-3 at the maximum depth (h_{max}),

$$S = Bm(h - h_f)^{m-1}\,|_{hmax} \quad (4\text{-}4)$$

The contact area ($A_c(h)$) is a modified projection area which corrects and removes the effect of the elastic recovery, expressed as the following equation:

$$A_c(h_c) = a_0 h_c^2 + a_1 h_c + a_2 h_c^{1/2} + a_3 h_c^{1/4} + a_4 h_c^{1/8}, \quad (4\text{-}5)$$

where a_0 to a_4 are equal to the values in Eq. 4-1, respectively, h_c is defined as the contact depth which is the indentation depth corrected by the deleting of the contribution of elastic deformation from the following equation:

$$h_c = h - \varepsilon \frac{P}{S}, \quad (4\text{-}6)$$

where ε is the geometry constant. In the case of Berkovich tip, ε is equal to 0.75. And P, S and h are the applied load, stiffness from the unloading segment and indentation depth from instrument, respectively.

After calculating the reduced elastic modulus from Eq. 4-2, the elastic modulus of the test materials can be extracted through the removal of the contribution from the tip, as shown below,

$$\frac{1}{E_r} = \frac{1-\nu_s^2}{E_s} + \frac{1-\nu_i^2}{E_i}, \quad (4\text{-}7)$$

where E_s and ν_s are the elastic modulus and Poisson's ratio for the sample. E_i and ν_i are the elastic modulus and Poisson's ratio for the indenter tip. For diamond Berkovich tip, $\nu_i = 0.07$ and $E_i = 1141$ GPa. After calculating the elastic modulus, the indentation hardness can be calculated using the following equation,

$$H = \frac{P}{A_c}, \tag{4-8}$$

where H, P, and A_c are the indentation hardness, load and contact area. According to Eqs. 4-2 and 4-8, the elastic modulus and hardness of the materials can be easily conducted at each loading rate.

The mechanical properties of the $Zr_{69}Cu_{31}$ amorphous alloy are measured by nanoindenter. As we know, the deformation caused by the impression of Berkovich tip can be divided into elastic and plastic parts at the quasi-static range. However, with increasing loading rate, the visco-elastic characteristics would be detected during the nanoindentation test. Under this condition, the mechanical response can consist of the elastic, visco-elastic and plastic regions. In other words, the load-displacement (P-h) curve would show the similar loop like axial compressive or tensile tests, as shown in Fig. 4-4. In this test, the peak load from the first to fifth cycle is 0.028, 0.625, 1.25, 2.5, 5 mN, respectively. By dividing the loading time (1 s), the loading rate in each cycle is equal to 0.028, 0.625, 1.25, 2.5, and 5 mNs^{-1}, respectively. The results show that the hysteresis phenomena also appear in the nanoindentation test at various loading rates. Also the hysteresis phenomena in the compressive and tensile test are dependent on the applied stress and strain rate.

Before extracting the measured data, it is important to know the source of the hysteresis characteristic. The measured data are attributed to the contribution of the test material, the tip, and the machine. The three parts, thus, can be treated as a series connecting. In MTS nanoindenter, the force is applied while the computer input signals are driven by the electromagnetic controlling system. If the setting of the loading rate is too fast, a potential problem from the controlling system is the hysteresis effect from the electromagnetic controlling system. The feedback rate would be too slow to let the applied loading rate fit the computer signals. In addition, the tip mass of the MTS nanoindenter XP is 6 g, which is heavier than that of Hysitron Triboindenter equal to 236 mg. The design of the MTS nanoindenter brings the error of the measured properties from the as-mentioned effects, limiting the range of the test conditions. For the case of $Zr_{69}Cu_{31}$, the slope of the unloading curve in each cycle, as shown in Fig. 4-4, exhibits a continuous change of the slope, leading to the difficulty of the extraction of the slope.

Thus, how to get the elastic modulus with the hysteresis response is important. From Eq. 4-4, the stiffness is defined as the slope of the unloading segment. A simple correction is to utilize the linear part of the unloading segment, as shown in Fig. 4-5. After this correction, the elastic modulus and hardness would be modified, shown in Fig. 4-5. These results still show a lower value of the elastic modulus tested at 5 mNs^{-1}, meaning that the hysteresis effect has not been fully corrected. In other words, in addition to the contribution of test samples, the machine would also exhibit the hysteresis effect. Under this condition, the measured data are not suitable for the measurement of the mechanical properties. In our study, all discussions and comparisons of mechanical properties are based on the hypothesis that the test condition is at quasi-static state. Hence, the tests in the dynamic regions would not be discussed. The comparison of the mechanical properties is made for data obtained below 5 mNs^{-1}.

As shown in Fig. 4-6, elastic modulus and hardness almost remain constant from 0.01 to 1 mNs^{-1}. For the test condition at 0.01 mNs^{-1}, a larger deviation compared with other test conditions would be introduced. The reason might be related to the thermal drift from surrounding. Also, according to the hardness variation shown in Fig. 4-6, the measured hardness and elastic modulus almost keeps a constant at ~5 GPa and ~102 GPa. The strain rate sensitivity does not seem to play an important role in the $Zr_{69}Cu_{31}$ thin film metallic glasses.

4-1-3 Evolution of mechanical properties of $Zr_{69}Cu_{31}$ and $Zr_{52}Cu_{29}Ti_{19}$ TFMGs via sub-T_g annealing

4-1-3-1 Evolution of the mechanical properties by sub-T_g annealing

According to the literature of Rivory et al. [44], the glass-transition temperature of $Zr_{69}Cu_{31}$ fabricated by sputtering was measured to be 357°C (630 K). The annealing temperature in this study was 473 K (~$0.75T_g$). The XRD patterns, shown in Fig. 4-7, indicate no crystalline peaks formed after annealing. Compared with the elastic modulus of the as-deposited films (94 GPa), the elastic modulus of the annealed $Zr_{69}Cu_{31}$ TFMG is 99 GPa, only 4% difference to the as-deposited films. It indicates that the amorphous nature slightly does not change much after annealing. Meanwhile, the hardness increases slightly from 5.2 to 5.7 GPa.

A similar transition of mechanical properties also occurs for $Zr_{52}Cu_{29}Ti_{19}$ TFMGs. According to the DSC scan, shown in Fig. 4-8, the obvious T_x point is 303°C (576 K). T_g is vague in the DSC curve due to the occurrence of the structural relaxation because of a high content of excess free volumes [44]. Utilizing the differential operation, T_g can be roughly found in the DDSC curve, equal to ~292°C (565 K). The annealing condition was set at 200°C (473 K) and 290°C (563 K), corresponding to ~0.83 and ~$0.99T_g$, respectively. Figure 4-9 shows the diffraction patterns, indicating the crystallization also does not occur during annealing.

Figure 4-10 shows the evolution of the mechanical properties influenced by the structural relaxation. Through annealing, the elastic modulus slightly increases from 102 to 112 GPa. The major reason causing the slightly increment of elastic modulus should come from the structural relaxation, not crystallization, due to the absence of any crystalline peak during annealing. Moreover, the hardness exhibits a considerable ~30% increment from 5.4 to 6.9 GPa, implying the structural relaxation would be an useful way for strengthening amorphous alloys. It will be discussed in Chapter 5.

4-1-3-2 Evolution of the mechanical response by sub-T_g annealing

In addition to the hardness increase after annealing, obvious pop-in events also appear after annealing. Figures 4-11(a) and (b) show the P-h curves of ZC and ZC200 indicating that the five curves from left to right are the results tested at 1, 0.5, 0.1, 0.05, and 0.01 mNs^{-1}. In Fig. 4-11(a), no discontinuous signals (pop-in events) are observed at each loading rate. As shown in Fig. 4-11(b), the pop-in events become obvious with decreasing loading rate after annealing at 200^{o}C (473 K).

For the case of the $Zr_{52}Cu_{29}Ti_{19}$ (ZCT) TFMGs, the P-h curves, as shown in Fig. 4-12(a), exhibit the pop-in events at the last indentation stage. The corresponding P-h curves of the ZCT sample annealed at 200 and 290^{o}C are shown in Figs. 4-12(b) and (c). The initial stage of the indentation exhibits obvious pop-in events. This evolution of the mechanical response is similar to that of $Zr_{69}Cu_{31}$. How the structural relaxation influences the pop-in events is an interesting issue, and which will be discussed in Chapter 5.

4-2 Ta addition in ZrCuTi alloy system

4-2-1 Structural characteristics of ZrCuTiTa alloy thin films via co-sputtering

The ZrCuTi and ZrCuTiTa thin film metallic glasses can both be fabricated by alloy sputtering. Considering the limit of the sputtering instrument and the simplification of the fabrication process, it is easier to control the composition via the co-deposition of ZrCuTi and Ta cathodes. The ZrCuTi alloy thin films with a series of tantalum addition were fabricated. As mentioned in Section 3-3-2, the recipe of the ZrCuTiTa can be divided into two parts. One group is processed at the constant value (300 W) of the ZrCuTi cathode and a series values (50, 100, 200, and 300 W) of Ta cathode. Another group is processed at the constant value (300 W) of the Ta cathode and a series values (200, 150, 100 and 50 W) of the ZrCuTi cathode. Also, the reference materials, monolithic ZrCuTi and pure Ta thin films, are also fabricated.

To understand the composition change by changing the powers of ZrCuTi and Ta cathodes, SEM/EDS measurements are made, as presented in Fig. 4-13. As shown in the left side of Fig. 4-13, the Ta content in the ZrCuTi-rich films increases with increasing Ta cathode power and reaches ~60 at%. In parallel, as shown in the right side of Fig. 4-13, the Ta content in the Ta-rich films can reach ~90 at% with decreasing ZrCuTi cathode power.

Figure 4-14 shows the XRD scans of the as-deposited ZrCuTiTa thin films, showing the broadening hump characteristic attributed to the amorphous nature for films with Ta content from 0 to ~75 at%. The ZrCuTi amorphous films with 75 at% Ta are demonstrated to be successfully fabricated without the precipitation of nanocrystalline phases. As the Ta content is higher than ~75 at%, the structure transfers to nanocrystalline structure corresponding to the tetragonal β-Ta phase. Moreover, to understand if nanocrystalline Ta would precipitate in the ZrCuTi amorphous matrix, the microstructure of these specimens is confirmed via TEM observation. Figures 4-15(a)-(f) present the plane-view bright-field images (BFI) showing the uniform contrast in the amorphous ZrCuTiTa thin films, indicating no obvious nanocrystalline particles have formed.

From the thermodynamic database [97], the heat of mixing in Zr-Ta, Cu-Ta, and Ti-Ta is +3, +2, and +1 kJ/mol, respectively. This indicates Ta is finally immiscible to Zr, Cu and Ti at given sufficient time and temperature. Because of the absence of the Ta crystalline phase, the as-fabricated alloy thin films are composed of the ZrCuTi amorphous solid solution with supersaturated Ta. Finally, the addition of immiscible Ta greater than 75 at% would lead to the formation of nanocrystalline Ta phase, shown in Figs. 4-15(g)-(i). Compared with the microstructure of pure Ta, as shown in Fig. 4-15(i), the grain size in these three specimens (83, 92 and pure Ta) are similar, equal to about 30 nm in diameter.

4-2-2 Nanoindentation results of ZrCuTiTa thin films via co-sputtering

Considering the ZrCuTi thin films with addition of Ta, as shown in Table 4-3, the elastic modulus of a series of the ZrCuTiTa alloy thin films remains a constant from 0.05 to 1 mNs^{-1}, respectively, indicating that the test condition is located in the quasi-state range. Thus, the hardness of the ZrCuTiTa alloy thin films, shown in Table 4-4, almost keep constant, meaning all of the ZrCuTiTa alloy thin films are insensitive to the loading rate, the same as the previous results of $Zr_{69}Cu_{31}$ and $Zr_{52}Cu_{29}Ti_{19}$.

As mentioned above, we understand the rate and structural-relaxation effect in the amorphous alloys. In this section, the composition effect is discussed. By adding Ta in the ZrCuTi amorphous alloys, the mechanical properties and responses would be changed. The mechanical properties of ZrCuTiTa alloy thin films are compared at the test condition equal to 0.05 mNs^{-1}. Figure 4-16(a) shows the relationship between Ta addition and the corresponding elastic modulus. Among all ZrCuTiTa alloy thin films, the glass forming range is strongly dependent on Ta content. From 0 to ~75 at%, the ZrCuTiTa alloy thin films exhibit amorphous nature; and for Ta greater than 75 at%, ZrCuTiTa alloy thin films exhibit the fully nanocrystalline characteristic while Ta content is greater than ~75%. Moreover, according to Fig. 4-16(a), a transition point of the elastic modulus is found at ~50 at%. Hence, the ZrCuTiTa alloy thin films can be divided into three regions: region I, II and III. In region I, named as Zr-rich ZrCuTiTa TFMGs, Ta content is from 0 to 50 at%. The ZrCuTiTa alloy thin films with Ta content from 50 to 75 at% is named as Ta-rich ZrCuTiTa TFMGs located in region II. Finally, region III corresponds to the nanocrystalline ZrCuTiTa alloy thin films, named as nc-Ta. As shown in Fig. 4-16(b), the hardness also increases with increasing Ta content, similar to the trend of the elastic modulus.

According to the nanoindentation platform, the deformation courses during indentation can be recorded with high resolution in load and displacement. Figures 4-17 to 4-19 show the P-h curves of Zr-rich, Ta-rich, and nc-Ta alloy thin films tested at 0.05 to 1 mNs^{-1}, respectively. Comparing the results at 0.05 mNs^{-1}, with increasing Ta content, the pop-in events become vague gradually at 0.05 mNs^{-1}, implying Ta would change the deformation characteristics in shear deformation. Also, Fig. 4-20 shows the SEM images of indentation marks at the depth of 1000 nm in a series of co-sputtered ZrCuTiTa alloy thin films. Figures 4-20(a) to (f) present the trace of shear bands in the ZrCuTiTa TFMGs; Figs. 4-20(g) and (h) show no trace of shear bands in the nc-Ta thin films. Contrary to ZrCuTiTa TFMGs, no traces of shear bands but the pile-up characteristic in $Zr_{55}Cu_{31}Ti_{14}$ are observed near the indentation marks, shown in the mark in Fig. 4-21(a). For the nc-Ta alloy thin films, Figs. 4-20(g)-(h) and Fig. 4-21(b) show a similar morphology, indicating no traces of shear bands.

4-2-3 Structural characteristics of ZrCuTi/Ta multilayer nanocomposite via alternative deposition

By adjusting the deposition time in the alternative deposition process, the thickness of the ZrCuTi alloy layers and Ta metallic layers can be controlled. As shown in Figs. 4-22(a) and (b), the cross-section BFI images of the two multilayer specimens consisting of 50 nm/50 nm individual layers and 50 nm/5 nm individual layers, respectively. The layers with black contrast correspond to the Ta layers, and the layers with white contrast correspond to the ZCT ones. In the Ta layers, the grain size is ~30 nm in diameter. The SAD patterns of these two specimens inserted in Figs. 4-22(a) and (b) show a diffused halo ring and the crystalline diffraction spots, corresponding to the amorphous nature of the ZCT layers and the nanocrystalline Ta layers.

As shown in Fig. 4-23(a), the ZCT 50 nm/Ta 50 nm multilayer thin films possess the diffraction of nanocrystalline Ta layers and the scattering of ZrCuTi amorphous layers. Two higher peaks at 33.8^{o} and 38.9^{o} belong to the diffraction of β-Ta (002) and (212) planes, respectively. Between the two peaks, a broadened hump exists between the diffraction peaks, corresponding to the ZrCuTi amorphous phase. Compared with the ZCT 50 nm/Ta 50 nm multilayer thin films, a thinner Ta thickness exhibits the weaker diffraction intensity, as shown in Fig. 4-23(b). However, the nanocrystalline peaks are not clear in the multilayer with thinner Ta crystalline layers.

4-2-4 Nanoindentation results of amorphous ZrCuTi/nanocrystalline Ta multilayer nanocomposites

Compared with co-sputtered ZrCuTiTa TFMGs, Ta can be introduced into ZrCuTi

TFMGs and serves as the reinforcement layers by the alternative deposition technique. The multilayer nanocomposites composed by the ZrCuTi and Ta layers were fabricated. Figure 4-24(a) shows the relationship between the elastic modulus and loading rate. A small deviation of the elastic modulus from 0.05 to 1 mNs^{-1} means all tests are located in quasi-state condition. In addition, the rate effect also does not play the major role in deformation, as shown in Fig. 2-24(b).

Figures 2-25(a) and (b) shows the P-h curves, indicating no pop-in event was tracked. These results are similar to the co-sputtered Ta-rich ZrCuTiTa TFMGs. In terms of the indentation marks, Fig. 4-26(a) shows a large quantity of shear band traces near the indentation mark.

4-3 Microcompression properties of $Zr_{55}Cu_{31}Ti_{14}$ pillars with Ta addition

4-3-1 Pre-load effect in microcompression test

Considering the fabrication of micropillar utilizing FIB, the taper angle would lead to the overestimation of the elastic strain. To solve this problem, a modified test for microcompression is brought up. The microcompression test can be divided into two cycles. The first cycle is the elastic deformation which applied load is set at below yield strength; the second cycle is set after yielding. Before introducing the two-cycle test in microcompression test, we need to understand the influence of the applied stress in the elastic region. The test material is the $Zr_{31}Cu_{15}Ti_{10}Ta_{44}$ micropillar (1 μm in diameter and 2 μm in height). The test condition is at the load equal to 1.2 mN at $6x10^{-4}$ s^{-1}. The holding time at the peak load is 2 seconds. The engineering stress-strain curve, as shown in Fig. 4-27, indicates no strain burst in the elastic deformation.

The data of the unloading segment is from the upper peak load (1.2 mN) to the lower peak load (0.12 mN), 10% of the upper peak load (1.2 mN). The corresponding recovery displacement is from ~75 nm to ~20 nm. The residual displacement after fully elastic recovery is ~10 nm, estimated by the linear extrapolation. Thus, the volume change can be discussed in two cases: the perfect ideal pillar (no taper) and the tapered one. Considering the perfect micropillar in 1 μm diameter, the pillar height is set at 2 μm. The pillar volume is equal to 1.57×10^9 nm^3. After deformation, the decrease of the pillar height is ~10 nm. The change of the diameter after compression is smaller than 3 nm. Due to the SEM resolution, the change in diameter might not be found. From the calculation for the ideal case, the influence from the pre-load effect can be neglected.

Thus, in the real case we can measure the change of the top and bottom diameter before and after deformation, as shown in Figs. 4-28(a) and (b). Compared with the morphology of the as-fabricated and elastic-deformed micropillar, as shown in Figs. 4-28(a) and (b), no shear band traces are observed at the appearance of the micropillar, indicating the deformation in the elastic region can be seen as homogenous deformation. Moreover, the change of the pillar diameter at the top is too small to be measured due to the limit of the SEM resolution. These results mean that the change of the diameter in the tapered pillar can also be neglected, the same as the perfect pillar.

To summarize these results, the pre-load effect can provide a stable contact between the surface of the tip and the top of the micropillar. The accidents while the tip surface contacts the top of the micropillar can be effectively reduced.

4-3-2 Microcompression results of ZrCuTiTa thin film metallic glasses

As mentioned in Section 4-1, the ZrCuTiTa thin films were fabricated by co-sputtering. The micropillars of $Zr_{55}Cu_{31}Ti_{14}$, $Zr_{45}Cu_{27}Ti_{15}Ta_{13}$, $Zr_{31}Cu_{15}Ti_{10}Ta_{44}$ and $Zr_{14}Cu_{7}Ti_{5}Ta_{74}$ TFMGs in 1 μm diameter were fabricated by Ga^{+} ion milling in FIB. The microcompression tests of $Zr_{55}Cu_{31}Ti_{14}$, $Zr_{45}Cu_{27}Ti_{15}Ta_{13}$, $Zr_{31}Cu_{15}Ti_{10}Ta_{44}$, and $Zr_{14}Cu_{7}Ti_{5}Ta_{74}$ TFMGs and nanocrystalline Ta were performed on the Agilent nanoindenter XP system. After tests, first of all, the strain rate ($\dot{\varepsilon}$) can be obtained by the following equation,

$$\dot{\varepsilon} = \frac{1}{h_p}\frac{dh}{dt}, \tag{4-9}$$

where h and h_p are the measured displacement and the pillar height, respectively, and t is test time. Utilizing this transformation, the corresponding strain rates in these tests are all at the level equal to 10^{-4} s^{-1}, listed in Table 4-5.

The load-displacement curves of these specimens can be readily converted into the engineering stress-strain curves by the transformation from load to engineering stress and displacement to engineering strain. As shown in Figs. 4-29(a)-(d), these figures combine the load-displacement and engineering stress-strain curves, and indicate an obvious transition point from elastic-to-plastic characteristic, and the signals of the plastic deformation is discontinuous, i.e. the strain bursts. In terms of the deformation of amorphous alloys, this kind of the plastic deformation is caused by shear band propagation. Since the micropillar is tapered, the stress would be concentrated at the top of the pillars due to the smaller contact area. Moreover, we define the stress at the first strain burst event as the yield stress from the engineering stress-strain curve. As shown in Figs. 4-29(a)-(d), the yield stress increases with increasing Ta content from 1.74 to 3.26 GPa, listed in Table 4-5. The increasing trend of the yield stress matches that of hardness measured by nanoindenter. Figures 4-30(a)-(c) show the deformed $Zr_{55}Cu_{31}Ti_{14}$, $Zr_{45}Cu_{27}Ti_{15}Ta_{13}$, and $Zr_{31}Cu_{15}Ti_{10}Ta_{44}$ micropillars. The results indicate that shear bands are emitted from the top of pillars, corresponding to the strain-burst events. In these three specimens, almost all shear bands are emitted parallel to each other. No cross trace of shear bands is observed.

Contrarily, no obvious strain-burst events are observed in the engineering stress-strain curves of the $Zr_{14}Cu_7Ti_5Ta_{74}$ micropillar, as shown in Fig. 4-29(d), indicating the continuous-like characteristic occurred in the microcompression. However, the deformed pillar of $Zr_{14}Cu_7Ti_5Ta_{74}$ still shows the emission of shear bands similar to the typical deformation characteristic of amorphous alloys. Different from other three pillars in Figs. 4-30(a)-(c), an obvious crossing of shear bands is found at the top of the $Zr_{14}Cu_7Ti_5Ta_{74}$ pillar, presented in Fig. 4-30(d). Compared with the previous results of Lai et al. [85], the Zr-based 1-μm-diameter micropillar shows no crossing shear bands the surface. The discrepancy implies that the deformation phenomena of $Zr_{14}Cu_7Ti_5Ta_{74}$ seem to be influenced by the compositional or structural effect.

4-3-3 Microcompression results of nanocrystalline Ta micropillars

To understand the deformation characteristic of nanocrystalline Ta, the microcompression of nanocrystalline Ta micropillar was performed. The engineering stress-strain curve indicates, as shown in Fig. 4-31, an obvious yielding characteristic at 5.77 GPa. The SEI image of the deformed pillar is shown in Fig. 4-32, showing that the plastic deformation is homogenous different from that in the monolithic amorphous alloys.

4-3-4 Microcompression results of ZrCuTi/Ta amorphous/nanocrystalline multilayered composites

Compared with the monolithic ZrCuTiTa TFMGs in Section 4-3-2, the multilayer micropillars composed by ZCT 50 nm/Ta 5 nm and ZCT 50 nm/Ta 50 nm are also tested. As shown in Figs. 4-33(a) and (b), the engineering stress-train curves show a similar characteristic to co-sputtered monolithic ZrCuTiTa micropillars, indicating an obvious elastic-to-plastic transition. The yield stress determined at the transition point from the first strain-burst event is obtained from the departure load divided by the top area, listed in Table 4-5. Compared with co-sputtered ZrCuTiTa amorphous micropillars, the yielding stress of ZrCuTi 50 nm/Ta 5 nm is 1.91 GPa, slightly greater than that of $Zr_{55}Cu_{31}Ti_{14}$ (1.74 GPa). The deviation of the yield stress would be caused by the ~10 vol% introduction of the nanocrystalline Ta layers. Also, the typical strain burst events are shown in Figs. 4-34(a) and 4-34(b), similar to that for the 50/5 and 50/50 multilayered micropillars, the phenomena of the strain burst are similar to that of $Zr_{55}Cu_{31}Ti_{14}$. It indicates no apparent effect on the basic deformation mechanism by inserting 5 or 50 nm Ta layers.

In the case of ZCT 50 nm/Ta 50 nm, the yielding strength is 3.46 GPa, much higher than that of ZCT 50 nm/Ta 5 nm, attributing to the 50 vol% nanocrystalline Ta. As listed in Table 4-5, ZCT 50 nm/Ta 50 nm exhibits the highest yield stress, about ~100% improvement to the base $Zr_{55}Cu_{31}Ti_{14}$. It indicating the introduction of the high-strength Ta layers can not only improve the yield stress but also postpone the emission of shear band propagation.

4-3-5 Microcompression results of ZrCuTi 50 nm/Ta 50 nm before strain burst

As mentioned above, inserting nanocrystalline Ta layers can effectively improve the mechanical properties of amorphous alloys. In addition, through the interaction between amorphous ZrCuTi layers and nanocrystalline Ta layers, the propagation of shear bands is effectively postponed. The critical strain where the first strain burst occurs is at ~7%. Before strain burst, the yielding characteristic can be found at ~2% strain. For comparison, the 2% strain at the occurrence of yielding is named as first yielding, and the ~7% strain at the first shear banding is named as second yielding. To understand the deformation behavior, two different strain stages were set at the strain before 7% and after 7% for the comparison of the as-deformed micropillar and as-sheared one. The stress-strain curves of the as-deformed and as-sheared micropillars are shown in Fig. 4-33(b) and Fig. 4-35(a), respectively. It is interesting that the stress-strain curve exhibits the signal of yielding characteristic. However, as illustrated in Fig. 4-36(b), the micropillar of ZrCuTi 50 nm/Ta 50 nm at ~5% is roughly similar to un-deformed one, implying the plastic deformation is located in the interior of the micropillar.

Chapter 5 Discussion

5-1 Enhancement of mechanical properties of ZrCu and ZrCuTi TFMGs via sub-T_g annealing

As mentioned in Section 4-1-4, the mechanical properties, especially hardness, can be enhanced via annealing. In Fig. 4-10, the improvement of hardness is up to ~30%. According to the literature of Yavari et al. [99], the mechanical properties would be strongly related to the structural evolution, defect evolution, and gas atmosphere during annealing. In this section, we would discuss the factors influencing the mechanical properties, as listed below:

(1) Oxygen effect during annealing,

(2) Formation of medium range order (MRO),

(3) Structural relaxation effect.

5-1-1 Oxygen effect

Both Ti and Zr have a high oxygen affinity, thus oxygen pick-up during vacuum annealing must be considered. Auger electronic spectrum (AES) depth-profile measurements from the three samples were done, as shown in Fig. 5-1 [100]. Curve A is found that the oxygen content in the as-deposited ZCT is limited to a thickness of about 8 nm from the surface. Oxygen profile for ZCT200 (curve B) is similar to that for as-deposited $Zr_{52}Cu_{29}Ti_{19}$ TFMGs, suggesting that oxygen absorption at 473 K is insignificant. By contrast, Curve C for $Zr_{52}Cu_{29}Ti_{19}$ TFMGs, which was annealed at 563 K for 1 h, shows some oxygen pick up. However, oxygen absorption is still limited within 12 nm from the film surface. The thickness of the oxygen pickup layer is ~0.5% of the thickness of the films. These surface layers are not expected to significantly affect the hardness values, which were obtained from an indentation depth of ~200 nm. As shown in Fig. 5-2, the relationship between hardness and thickness of oxygen layer suggests that the increasing level of hardness (~30%) is much larger than that of oxygen layer (<0.5%). Therefore, the oxygen absorption should not play a major role in the hardness increase.

5-1-2 Formation of medium range ordering (MRO) structure

Structure relaxation can proceed by various routes. During the relaxation, although long-range diffusion is not likely to occur, the thermal energy is sufficient to rearrange atoms locally for 1~2 nm and to form more stable MRO structures [101,102]. Structural examinations using TEM and HRTEM do not reveal the presence of crystalline phase greater than 2 nm. For example, Fig. 5-3(a) is a HRTEM image of ZCT. The encircled area exhibits a scattering pattern which is different from its surrounding region, suggesting the presence of MRO structure. The corresponding Fourier transformed diffraction patterns from the MRO region taken with a selected square area of 1 nm still show faint and diffuse contrast, indicating it is not a crystalline phase. It is noted, however, the density of MRO structure in the as-sputtered ZCT TFMGs is relatively low. The population of MRO increases in ZCT200 in Fig. 5-3(b) and ZCT290 in Fig. 5-3(c). The population of MRO clusters in specimen ZCT290 is higher than those in ZCT200 and ZCT. The presence of these MRO clusters in a glass matrix is expected to increase the resistance for shear band propagation, thereby the strength or hardness. This is similar to the case of having nanocrystals in a glass matrix [103]. A higher sub-T_g annealing temperature or longer annealing time is expected to produce more MRO clusters and, therefore, a higher hardness [100].

5-1-3 Annihilation of excess free volume

The XRD pattern from the as-deposited $Zr_{52}Cu_{29}Ti_{19}$ thin film exhibits the typical broad peak, indicating an amorphous structure. After annealing at 473 K ($0.8T_g$) and 563 K ($0.9T_g$), the film still remains amorphous, according to the XRD spectra. The full widths at the half maximum (FWHM) intensity of the amorphous hump, indicative of the inter-atomic distance, are measured and the data are plotted in Fig. 5-4(a). Similarly, the FWHM value for the SADs are measured and plotted in Fig. 5-4(b). Again, the values show a decreasing trend upon annealing. With decreasing value, the inter-atomic distance appears to slightly reduce as a result of the sub-T_g annealing. Compared with the decreasing trend of FWHM, the hardness increases with increasing annealing temperature, as shown in Fig. 5-4(c).

Furthermore, Spaepen [72] indicates the relationship between applied stress and the free-volume density. The strain rate is a function of the average free volume of an atom υ_f and the applied stress, σ, as listed in Eq. 5-1. When the strain rate (or indentation rate) is fixed and at room or low temperatures, the relation can be simplified as

$$\sigma = \frac{2kT}{\varepsilon_0 \upsilon_0}\left(2\beta + \frac{\gamma\upsilon^*}{\upsilon_f}\right), \tag{5-1}$$

where k is the Boltzman constant, T is the temperature, ε_0 is the strain of a flow unit, υ_0 is the volume of a flow unit, β is a constant, γ is a geometrical factor, υ^* is the effective hardsphere size of the atom, and υ_f is the average free volumes of an atom. Assume further that shear band formation is proportional to the average free volume density υ_f, it is evident that the strength of the material increases with a decreasing υ_f. In other words, the observed hardness increase after structural relaxation is a result of the reduction of free volume caused by sub-T_g annealing. The amount and distribution of free volumes obviously play the major role in the formation of shear bands. [72] Amorphous alloys synthesized via sputtering usually contain a significant amount of atomic size defects [99], as illustrated in Fig. 5-5. In as-cast metallic glasses, open-volume defects could be broken into two categories: intrinsic voids surrounded by nine or less atoms and larger holes surrounded by ten or more atoms [104-106]. The intrinsic voids which are typically smaller than an atom exhibited certain similarity with Bernal's canonical holes. These voids cannot be removed by thermal annealing. By contrast, the larger holes with size approximately equal to an atom or termed as the atomic size holds were mainly nonspherical with some resemblance to crystalline vacancies. They can be removed by annealing. During the nanoindentation of the as-deposited film (sample ZCT), the atomic size holes serve as the sites for stress release during the initial stage of deformation. These results in a softer material and the delay of the onset of shear band formation, i.e., pop-in events (Fig. 5-6). It was pointed out by Schuh et al. [107] that shear band would not nucleate unless STZ cluster has reached the critical size. This requires multiple STZs operating in a sequential fashion, assisted by the deformation-induced free volume. Thus, the onset of pop-in does not occur until the exhaustion of the atomic size holes and the creation of sufficient amounts of deformation-induced free volume.

During sub-T_g annealing, atoms can rearrange locally without long-range diffusion, which reduces the average distance among atoms. The majority of atomic size holes were gradually annealed out and the structures in samples ZCT200 and ZCT290 are partially relaxed. Upon indentation, because of the lack of the atomic size holes to absorb deformation strain, pop-in events occur much earlier in these samples, as shown by arrows in Fig. 5-7(b) for specimen ZCT200. Similar situation occurs for specimen ZCT290, as shown in Fig. 5-7(c).

In conclusion, the sub-T_g annealing (structural relaxation) provide a considerable improvement in hardness [100]. Nevertheless, the structural relaxation make the yielding (the formation of shear band) earlier due to the annihilation of the excess free volume. The phenomenon is called as embrittlement [94]. After relaxation, the mechanical properties of the relaxed amorphous alloys are similar to the amorphous ceramic materials because of the annihilation of the excess free volume.

5-1-4 Relationship between time-dependent mechanical response and sub-T_g annealing

As mentioned in Section 5-1-2-2, the strengthening of ZrCuTi TFMGs can be achieved by sub-T_g annealing, as result of the structural relaxation. According to Yo et al. [108], the atomic-sized defects can be annihilated in reversible and irreversible forms. The previous type would be related to the non-equilibrium deformed structure (open-volume atomic-size defects), meaning these defect would recover after the unloading of the stress [109,110]. The later one can be annihilated through thermal annealing. The difference between these two forms is the Gibbs free-energy level, as shown in Fig. 5-8 [108]. The Gibbs free-energy level in the reversible type is similar; that in the irreversible type exhibits a larger energy gap. Utilizing the time-dependent mechanical test, the relaxation characteristics between as-deposited and relaxed ZCT TFMGs can be qualitatively measured. Due to the lack of strain rate sensitivity in amorphous alloys, the holding test is set at the 5 mN for 30 seconds. For ZCT, ZCT200 and ZCT290, the holding tests are performed at MTS nanoindenter platform. For comparison, the test condition is set at 5, 1, and 0.05 mNs^{-1}, and the load functions are shown in Fig. 5-9.

Considering the effect of annealing temperature, the anelastic deformation tested at 5 mNs^{-1} (Fig. 5-10(a)) decreases with increasing annealing temperature, implying that the thermal unstable free volume is gradually annihilated with increasing annealing temperature.

Moreover, the results tested at 1 and 0.05 mNs^{-1} (Figs. 5-10(b) and 5-10(c)) are similar, meaning that the phenomenon of structural relaxation can be detected in all test conditions. Different test conditions just influence the magnitude of the anelastic phenomena.

As we know, the non-equilibrium deformed structure (open-volume atomic-size defects) occurring in the loading segment would relax at the holding segment [109,110]. At 5 mNs^{-1}, the open-volume atomic-sized defects are not completely relaxed in the loading segment because the short loading time can not provide a sufficient time for the relaxation of this kind defects. In other words, the displacement in the holding segment might be attributed to the relaxation of thermally unstable defects and open-volume regions. Contrarily, the open-volume atomic-size defects tested at 0.05 mNs^{-1} would be almost completely relaxed in the loading segment, indicating that the holding segment can only be attributed to the relaxation of the thermally unstable defects. Whatever the effect of the loading rate in time-dependent nanoindentation tests, the displacement decreases with increasing annealing temperature. This is another indirect evidence to prove the reduction of excess volumes.

5-2 Evolution of mechanical properties of ZrCuTi TFMGs by addition of immiscible Ta

5-2-1 Estimation of the mechanical properties in ZrCuTiTa alloy thin films

5-2-1-1 Estimation of the mechanical properties of ZrCuTiTa alloy

To understand the effect of immiscible Ta to the ZrCuTi amorphous matrix, the rule of mixture is a good tool to analyze the evolution of mechanical properties with a variation of Ta content. Based on the Voigt (iso-strain) and Reuss (iso-stress) model, the elastic modulus of the ZrCuTiTa alloy thin films can be estimated by the following equation,

$$E_{alloy} = E_{ZrCuTi} f_{ZrCuTi} + E_{Ta} f_{Ta} \ , \tag{5-2}$$

$$E_{alloy} = \left(\frac{f_{ZrCuTi}}{E_{ZrCuTi}} + \frac{f_{Ta}}{E_{Ta}}\right)^{-1} , \tag{5-3}$$

where E_{alloy}, E_{ZrCuTi}, E_{Ta} are the elastic modulus of estimated values. For ZrCuTiTa alloys, $Zr_{55}Cu_{31}Ti_{14}$, and tetragonal Ta, respectively, and f_{ZrCuTi} and f_{Ta} are the volume ratio of ZrCuTi and Ta, respectively. Also, the hardness (H) can be estimated by the same model, as shown below,

$$H_{alloy} = H_{ZrCuTi} f_{ZrCuTi} + H_{Ta} f_{Ta} \ , \tag{5-4}$$

$$H_{alloy} = \left(\frac{f_{ZrCuTi}}{H_{ZrCuTi}} + \frac{f_{Ta}}{H_{Ta}}\right)^{-1} . \tag{5-5}$$

In the rule of mixture, the solubility of Ta is assumed to be zero, meaning Ta would precipitate completely in the ZrCuTi amorphous matrix forming a composite, the resulting elastic modulus and hardness can be estimated via rule of mixture, either the Voigt or the Reuss model as the upper or lower bound [74]. Using the SEM-EDS results, at% can be transferred to vol%. Table 1 lists the basic properties of Zr, Cu, Ti, $Zr_{55}Cu_{31}Ti_{14}$, BCC-Ta, and tetragonal Ta. Thus, the volume ratio can be estimated. As shown in Figs. 5-11(a) and 5-11(b), little deviation of the elastic modulus and hardness is found between the calculations using atomic percent and volume percent. Hence, the estimation by atomic percent would be directly used for comparison with experiment results in the next section.

5-2-1-2 Comparison between estimated and experimental nanoindentation results

In terms of mechanical properties, the elastic modulus of the $Zr_{55}Cu_{31}Ti_{14}$ and β-Ta films were first measured by nanoindentation; the values are 93.5 and 220.6 GPa, respectively. These calculated ROM values can be compared with the experimentally measured ones by nanoindentation, as shown in Fig. 5-12. Figure 5-12(a) shows the variation of elastic modulus as a function of Ta content, in which the data can be divided into region I (ZrCuTi-rich TFMGs), region II (Ta-rich TFMGs), and region III (nanocrystalline β-Ta). The variation of elastic modulus would indicate the change of atomic packing with increasing Ta content. In region I, the measured elastic modulus initially remains nearly constant (~105 GPa) over the Ta content from 0 to 50 at%. Then, the elastic modulus value starts to increase within the Ta content 50-75 at% in region II (reaching ~140 GPa). Finally, a high elastic modulus appears when Ta content is higher than 75 at% in region III (reaching ~220.6 GPa), corresponding to the formation of crystalline β-Ta phase. For regions I and II, the increase of elastic modulus does not exhibit a linear trend but has a transition point near 50 at% Ta, implying there undergoes a drastic change in atomic packing when the Ta content exceeds 50 at%, as discussed in the next section.

In Fig, 5-12(a), the measured modulus data exhibit a large deviation except region III. The discrepancy might be caused by many reasons. One factor influencing the modulus or hardness of metallic glasses is the free volume amount [96]. According to Charleux et al. [111], the elastic modulus increases with increasing annealing time through the process of crystallization and reduction of free volume. But contrarily, the current elastic modulus of ZrCuTiTa alloy thin films is much lower than the prediction, implying the reduction of free volume should not be the cause. The other important factor is the local atomic bonding and packing in metallic glasses. Note that the hypothesis (no solubility of Ta in the ZrCuTi amorphous matrix) made for the theoretical predictions is in fact incorrect based on the XRD and TEM observations. Ta atoms do get involved with other elements in the local atomic packing structure and would affect the elastic properties of the resulting ZrCuTiTa alloy thin films. This will be discussed in the next section.

The measured hardness also exhibits a similar trend, as presented in Fig. 5-12(b). With increasing content of Ta, the measured hardness increases. For the maximum hardness in regions I and II of such TFMGs, the enhancement of hardness is about 100% with respect to the hardness without the addition of immiscible Ta. The hardness levels of the ZrCuTi-rich and Ta-rich TFMGs reach ~7 and ~10 GPa, respectively. Except for the W-, Fe-, Co-, Ni-based amorphous alloys, Ta-based amorphous alloys exhibit the highest hardness [112]. As Ta is precipitated out in region III, the hardness increases rapidly to a level ~20 GPa.

Similar to elastic modulus, the hardness of the ZrCuTiTa films is also theoretically calculated by the Voigt and Reuss model between ZrCuTi (5.27 GPa) and β-Ta (20 GPa). As shown in Fig. 5-12(b), the overall agreement is also poor, particularly for region II. With increasing Ta content, the amorphous structure gradually transfer to the crystalline structure. Hence, the hardness jumps from 10 to 16 GPa or higher, corresponding to the nanocrystalline β-Ta with Zr, Cu and Ti solutes.

5-2-2 Structural evolution of ZrCuTiTa alloy thin films via XRD analysis

As discussion in Chapter 4, the variation of Ta concentration is sensitive to the film structure. Figure 4-14 presents the XRD scans of the as-deposited ZrCuTiTa thin films, showing the diffuse broad hump characteristic of an amorphous nature for films with Ta content from 0 to 75 at%. The ZrCuTi amorphous films with 0-75 at% Ta are demonstrated to be successfully fabricated without the precipitation of nanocrystalline particles. As the Ta content is higher than ~75 at%, the structure transfers to nanocrystalline structure corresponding to the crystalline Ta which major composed by tetragonal β-Ta, as also confirmed by TEM observations.

The solubility of immiscible Ta in the current sputtered ZrCuTiTa films can be up to ~75 at%. The XRD hump positions are seen to shift slightly to higher 2θ values with increasing Ta content. Through the mathematical operation, the diffraction spectrum can be described using the Voigt model [113], as shown in Eq. 5-5. The peak position of amorphous hump in 2θ, named x, in ZrCuTiTa TFMGs can be determined [113], as shown below,

$$I = I_0 + A \cdot \frac{2\ln(2)}{\pi^{3/2}} \frac{w_L}{w_G^2} \cdot \int_{-\infty}^{\infty} \frac{e^{-x^2}}{(\sqrt{\ln 2}\,\frac{w_L}{w_G})^2 + (\sqrt{4\ln 2}\,\frac{x-x_c}{w_G} - t)^2} dx, \tag{5-6}$$

where I and x are the value of intensity and 2θ, respectively. I_0 and A are the fitting parameter. x_c, w_G, and w_L are the peak position, FWHM of Gaussian profile, and FWHM of Lorentz profile, respectively. The value of R^2 in all specimens are greater than 0.95. Utilizing the Voigt model for peak fitting, the hump positions of the ZrCuTiTa as a function of Ta content are presented in Fig. 5-13. It can be seen that the 2θ positions exhibit a linear trend at the ZrCuTi-rich side, implying that Ta atoms are indeed present as solutes in the ZrCuTi-rich amorphous matrix and form a monolithic amorphous solid solution. With increasing Ta content greater than 50 at% at the Ta-rich side, the 2θ positions do not increase but keep nearly constant, implying that the high addition of Ta starts to form local Ta clustering or Ta-Ta bonding. The 2θ shift can reflect the Ta role in the sputtered films.

5-2-3 Influence of Ta content on mechanical properties

For the current series of ZrCuTiTa TFMGs, the supersaturated Ta solute appears to be the key in influencing the mechanical properties. Through the mathematical operation, the peak position of inter-atomic distance in ZrCuTiTa TFMGs can be determined using Eq. 5-7. Fig. 5-14 exhibits the relationship between peak position and elastic modulus of ZrCuTiTa TFMGs, indicating that the peak position decreases with increasing elastic modulus. The peak position continuously shifts to smaller values in region I and remains constant in region II. As we know, elastic modulus can be determined by the following equation [56],

$$E = \frac{1}{r_0}\left(\frac{1}{dr}\left(\frac{dU}{dr}\right)\right)_{r_0}, \tag{5-7}$$

where E and U are the elastic modulus and the inter-atomic potential function, respectively. r and r_0 are the average distance among atoms and the bonding length, respectively. Ta is a material with a melting point of 3269 K, much higher than Zr (2125 K), Cu (1356 K), and Ti (1933 K), as compared in Table 5-1. Moreover, the elastic modulus of crystalline Ta (>170 GPa) is also much higher than those of crystalline Zr (129 GPa) [114], Cu (135 GPa) [115], and Ti (128 GPa) [116]. As mentioned in previous section, a large deviation exists between the predicted and experimental modulus values. The key is considered to be the formation of Ta-Ta bonding. Considering the possibility of neighbor atoms among Zr, Cu, Ti, and Ta, the bonding can be divided into three types: miscible type (Zr-Cu, Zr-Ti, and Cu-Ti), immiscible type (Zr-Ta, Cu-Ta, and Ti-Ta), and self type (Zr-Zr, Cu-Cu, Ti-Ti, and Ta-Ta). Only the formation of substantial Ta-Ta self bonds would lead to the apparent increase of elastic modulus.

According to Eq. 5-7, an increase of elastic modulus can be caused by the reduction of bonding length or the increment of thermal stability. In the case of ZrCuTiTa thin films, a minor addition of immiscible Ta in region I slightly decreases the bonding length (the XRD hump to a higher 2θ value), but the major bonding would still be composed by the miscible and immiscible types. In other words, the amorphous nature would not change much with the addition of immiscible Ta in region I. However, in region II, Ta serves as the major element in the amorphous structure, indicating the self type of Ta-Ta bonds would form with a high population. The schemes in region I and region II are shown in Fig. 5-15.

5-2-4 Microstructure of ZrCuTiTa thin film metallic glasses

As mentioned above, the effect of Ta addition is roughly estimated, implying that Ta might serve as the solute in the ZrCuTi amorphous matrix at a low Ta addition or the solvent as well as the amorphous matrix at a high Ta addition. Through the analyses of XRD spectrums using the Voigt model, the effect of Ta content can be easily measured. The peak position of the amorphous humps can be determined using Eq. 5-6. Moreover, FWHM of the Voigt profile (w_V) is empirically expressed as the following equation [113],

$$w_V \approx 0.5346 w_L + \sqrt{0.2166 w_L^2 + w_G^2} \ , \tag{5-8}$$

where w_L and w_G are the FWHM of Lorentz function and Gaussian function, respectively. After mathematical operation, the relationship among the Ta content, peak position of amorphous hump, and FWHM of amorphous hump is shown in Fig. 5-16. The value of FWHM in a series of ZrCuTiTa TFMGs (0 to 74 at% in Ta), exhibits a sudden jump from 5.47 to 5.75 and then gradually decrease to 4.35. Finally, the value of FWHM keeps a constant equal ~4.35. The non-linear change implies that Ta atoms react with Zr, Ti, and Cu atoms. There are two possible reactions. The first one is the formation of intermediate phase, such as intermetallic compound; another is phase separation in composition or structure. As shown in the TEM results (Figs. 4-15(a)-(f)), no crystalline peaks were found, indicating the intermediate phases do not form. In other words, the phase separation is the possible candidate leading to the evolution of FWHM. Considering the phase separation in composition or structure, two different TEM techniques were used for analysis, as presented in next.

5-2-4-1 Ta solute in ZrCuTi amorphous matrix

As discussed in Section 5-2-3, Ta content is the major effect influencing the microstructure. As shown in Figs. 5-17(a)-(c), the high angle annular dark field (HAADF) images of $Zr_{45}Cu_{27}Ti_{15}Ta_{13}$, $Zr_{41}Cu_{23}Ti_{12}Ta_{24}$, and $Zr_{31}Cu_{15}Ti_{10}Ta_{44}$ exhibit the inhomogeneous contrast. The intensity of the HAADF image (I_{HAADF}) can be roughly expressed as the following equation [117],

$$I_{HAADF}(M) \propto V_M(\sigma_M Z_M^{1.85}), \tag{5-9}$$

where M is target element. V_M, σ_M and Z_M are the volume of the matter intercepted focus plane, atomic packing density and atomic number, respectively. Assuming the thickness of the TEM specimen is constant, the value of V_M would be constant. The atomic packing density can be calculated by the following equation,

$$\sigma_M = \frac{V_{atoms}}{V_c}, \tag{5-10}$$

where V_{atoms} and V_c are the volume of the atoms occupying in the unit cell and the volume of the unit cell. Due to the lack of the long-range ordering structure, this term is hard to calculate. As shown in Fig. 5-18 [118], the change of the packing density in Cu_xZr_{1-x} amorphous alloy (x=50-75 at%) is ~0.5%, indicating that the change can be neglected in Z-contrast image. By simplifying Eq. 5-10, the intensity of the HAADF image is directly determined by atomic number.

For the $Zr_{41}Cu_{23}Ti_{12}Ta_{24}$ and $Zr_{31}Cu_{15}Ti_{10}Ta_{44}$ TFMGs, the composition of the bright and dark regions can be measured using the point analysis. In $Zr_{41}Cu_{23}Ti_{12}Ta_{24}$, the compositions of the bright and dark regions are averaged by five tests. As shown in Table 5-3, the difference of Zr, Cu, Ti and Ta content between the white and dark domains is smaller than 5 at%, implying that the compositional deviation is very small. Moreover, the results of the $Zr_{31}Cu_{15}Ti_{10}Ta_{44}$ TFMGs, as shown in Table 5-4, exhibit a tiny deviation in composition between the white and dark domains, too. However, from Eq. 5-9, it is reasonable to suggest that the white domains would be composed with a higher Ta content.

From the aspect of the thermodynamics, Section 5-2-3 mentions the competition of the bonding among miscible, immiscible and self types. The HAADF results indeed support our prediction and fix the boundary condition between regions I and II from ~50 to ~44 at% of Ta, as shown in Fig. 5-19.

5-2-4-2 Zr, Cu, and Ti solutes in Ta amorphous matrix

Regarding the ZrCuTiTa TFMGs in region II, there are several indirect evidence, including the XRD results, elastic modulus, and hardness, indicate that the short-range ordering structure (amorphous structure) gradually transfers to long-range ordering structure (crystalline structure). The non-linear change in elastic modulus and hardness implies the unknown phase might influence the phase transformation phenomena. The intermediate phase or the formation of the precursor of crystalline phase would be the possibility [59,119]. Based on the Ta-Zr, Ta-Cu, and Ta-Ti binary phase diagram, as shown in Figs. 3-4(a)-(c), no intermetallic phase exists in the three alloy systems, implying this reaction can not occur spontaneously. The possible reaction would be attributed to the formation of precursors or embryos of the crystalline phase. Moreover, Fig. 5-20 exhibits the X-ray diffraction patterns at different annealing temperatures, indicating that the obvious crystallization reaction roughly starts in the interval from 550 to 600^{o}C. The apparent crystalline peaks can be found at 650^{o}C annealing, forming the BCC (α-phase) and tetragonal (β-phase) Ta. It means the precursor would be the embryos of the crystalline tantalum phase.

Utilizing HRTEM analysis technique, the influence of Ta addition in structural aspect can be examined. For the region I in ZrCuTiTa TFMGs, the HRTEM image of $Zr_{45}Cu_{27}Ti_{15}Ta_{13}$ TFMG is shown in Fig. 5-21(a), with the Fast Fourier transform (FFT) spectrum shown in Fig 5-21(b). No clear lattice fringes can be found, indicating the absence of the precursor of the crystalline phase even crystalline particles. With increasing Ta content, the results of $Zr_{41}Cu_{23}Ti_{12}Ta_{24}$ (Figs. 5-21(c) and (d)) and $Zr_{31}Cu_{15}Ti_{10}Ta_{44}$ (Figs. 5-21(e) and (f)) do not show crystalline fringes, too. Contrarily, the $Zr_{23}Cu_{12}Ti_{8}Ta_{57}$, $Zr_{19}Cu_{6}Ti_{7}Ta_{68}$, and $Zr_{14}Cu_{7}Ti_{5}Ta_{74}$ TFMGs exhibit different phenomena in HRTEM observation, as presented in Figs. 5-22(a), (c), and (e) with the corresponding FFT patterns are shown in Figs. 5-22 (b), (d) and (f), respectively. Clear lattice fringes can be found in $Zr_{19}Cu_{6}Ti_{7}Ta_{68}$ and $Zr_{14}Cu_{7}Ti_{5}Ta_{74}$ TFMGs. Moreover, Fig. 5-23 exhibits the magnified lattice image, indicating clear clusters. The observation of cluster formation in $Zr_{14}Cu_{7}Ti_{5}Ta_{74}$ TFMGs is also another evidence for proving the apparent elastic modulus increment.

5-3 Mechanical behaviors in amorphous ZrCuTiTa micropillars

The signals of the strain bursts in microcompression tests represent the events of the shear band propagation. The time versus strain rate curves of $Zr_{55}Cu_{31}Ti_{14}$, $Zr_{45}Cu_{27}Ti_{15}Ta_{13}$, $Zr_{31}Cu_{15}Ti_{10}Ta_{44}$, and $Zr_{14}Cu_{7}Ti_{5}Ta_{74}$ TFMGs are shown in Figs. 5-24 to 5-27, respectrively. In Fig. 5-24, the events of strain bursts occur at 1.74, 1.97, 2.17, 2.39, and 2.58 GPa. We define $\dot{\varepsilon}_e$ and $\dot{\varepsilon}_b$ to be the strain rates at the elastic region, and the peak value for the strain burst, respectrively. For the $Zr_{55}Cu_{31}Ti_{14}$ TFMGs, it is easy to find the following relationship,

$$\dot{\varepsilon}_e << \dot{\varepsilon}_b . \tag{5-11}$$

In addition, the strain rate after strain bursts returns to $\dot{\varepsilon}_e$. As shown in Figs. 5-25 and 5-26, the $Zr_{45}Cu_{27}Ti_{15}Ta_{13}$ and $Zr_{31}Cu_{15}Ti_{10}Ta_{44}$ TFMGs also exhibit the similar phenomnon. With increasing Ta content, the results of $Zr_{14}Cu_{7}Ti_{5}Ta_{74}$ TFMGs is different from the previous three specimens, shown in Fig. 5-27. From the time versus strain rate curve, the strain burst is obviously smaller than that of the previous three specimens. The relationship in the $Zr_{14}Cu_{7}Ti_{5}Ta_{74}$ TFMG can be expressed as following equation,

$$\dot{\varepsilon}_e < \dot{\varepsilon}_b . \tag{5-12}$$

To compare these results, $\dot{\varepsilon}_b$ is normalized by $\dot{\varepsilon}_e$; and the stress, (σ) is normalized by the elastic modulus (E), for the four alloys as illustrated in Fig. 5-28. For the $Zr_{55}Cu_{31}Ti_{14}$, $Zr_{45}Cu_{27}Ti_{15}Ta_{13}$, and $Zr_{31}Cu_{15}Ti_{10}Ta_{44}$ TFMGs, the values of $\dot{\varepsilon}_b$ are almost ~10^3 times of $\dot{\varepsilon}_e$ except for the early stage. In the case of the $Zr_{14}Cu_{7}Ti_{5}Ta_{74}$ TFMG, most of strain burst is at 10^1 s^{-1} except for the final stage. As marked by circle in Fig. 5-28, the values for the strian bursts are 10^1~10^2 s^{-1}.

According to the literature of Schuh et al. [15,62], the inhomogeneous deformation is also called as shear banding, in amorprhous alloys. The shear strain rate of shear bands ($\dot{\gamma}$) can be described by the following constitutive equation for the transient yield strength of a metallic glass prior to any glass structure change by deformation,

$$\dot{\gamma} = \dot{\gamma}_s \exp\left(-\frac{\Delta G_s}{kT}\right), \tag{5-13}$$

where $\dot{\gamma}_s$ and ΔG_s are a characteristic strain rate related to the critical local strain of STZs at the beginning of shear bands and the activation free enthalpy to initiate deformation. Through Argon's analysis [15], ΔG_s can be simplified to a form common in solid mechanics,

$$\Delta G_s \approx C_s \Omega_s \frac{(\tau_s - \tau)^2}{\tau_s}, \tag{5-14}$$

where $C_s \approx 4.6$ is a constant, τ_s is the athermal stress required to initiate the critical shear event, which occupies an activation volume Ω_s.

Based on Eq. 5-13, the evolution of the $\dot{\gamma}$ value is dependent on $\dot{\gamma}_s$ and ΔG_s. Considering the value of $\dot{\gamma}_s$, this concept is similar to the activation of dislocation, shearing a line of atoms to neighbor sites at some specific slip planes. The basic unit of dislocation is the Burger's vector. Similarly, according to Argon's literature [15], the critical strain ($\dot{\gamma}_s$) to activate one shear band would be the same in all amorphous alloys. We assume that the value of $\dot{\gamma}_s$ is constant in each alloy system. ΔG_s (Eq. 5-14) would be the key influencing the strain burst at steady state. To initiate the shear band, ΔG_s is equal to zero while τ is equal to τ_s, meaning that shear band can start spontaneously. After the start of shear bands, in this equation, we can discuss in two parts. The first is Ω_s; another is $(\tau_s - \tau)^2/\tau_s$. In the initial stage, since $(\tau_s - \tau)^2/\tau_s$ is so small, Ω_s depending on the alloy systems dominates the key for Eq. 5-14. A higher Ω_s would lead to a slower strain burst. For the $(\tau_s - \tau)^2/\tau_s$ term, with increasing stress greater than τ_s, $(\tau_s - \tau)^2/\tau_s$ considerably increases inducing a drop of ΔG_s. This implies that the shear bands can propagate spontaneously much easily after yielding. In Eq. 5-14, it is easily to found that the strain burst rate is influenced by the activation volume at the early stage after yielding; and by the shear stress while shear stress can activate sufficient STZs for cooperative movement.

Considering the role of Ta, the elastic modulus increases with increasing Ta content, meaning that the bonding among atoms become tough by adding Ta [120]. To initiate shear bands, a higher shear stress is needed to initiate shear bands at Ta-rich ZrCuTiTa TFMGs due to a greater threshold of shear stress (τ_s). This is one of reasons to induce an increase of ΔG_s. Moreover, another factor influencing the value of ΔG_s is activation volume, Ω_s which can be conducted using cooperative shearing model (CSM), as following [121,122],

$$\Omega_s = \frac{kT}{C'mH}, \tag{5-15}$$

where T, m, and H are temperature, strain rate sensitivity, and hardness, respectively. k is the Boltzmann constant. C’ is a function of the threshold shear resistance at temperature T. It is easily to understand that Ω_s is proportional to the inverse of mH (the product of m and H).

The measured hardness and strain rate sensitivity is shown in Fig. 5-29(a). Figure 5-29(b) indicates the value of mH increases with increasing Ta content. From Eq. 5-14, the activation volume decreases with increasing Ta content. A smaller activation volume would make less atoms move cooperatively along the shear direction. To combine Eqs. 5-14 and 5-15, we can find that the trends of τ_s and Ω_s both indicate that ΔG_s increases with increasing Ta content. The decrease of $\dot{\gamma}$ is attributed to the increment of Ta content.

From structure aspect, many researchers claim that the obstacles, such as particles, precipitates, or reinforcements, usually effectively cease shear bands [88,123,124]. Through these methods, more shear bands can be initiated at the same time, abating the shear localization. In our case, the role of Ta-rich nanoclusters is similar to the mentioned concept. However, Ta-rich nanoclusters can not arrest the shear bands because the cluster size is too small. These nanoclusters near shear bands must move along with shear band propagation. The friction between the nanoclusters and amorphous matrix would not only exhausts the kinetic energy of shear bands but also lower the free volume in shear bands, meaning that shear bands cannot prorpregate immediately. More inititiation propagation events of shear bands are needed to deform. In addition, the heat by the friction would lead to the relaxation in the region which shear bands pass throguth. To initiate another event of shear band at the same position, a higher stress is needed, called as work-hardening-like characteristic. This is the phenomanon of multiple shear bands, causing the continuous-like deformation characterisitc. The deformed $Zr_{14}Cu_7Ti_5Ta_{74}$ pillar exhibits the multiple shear bands, marked in Fig. 5-30.

As mentioned above, the scope which influences the strain rate of strain burst can be clearly described. However, the effect of activation volume still can not answer why faster strain bursts occur at the final stage of compression in the $Zr_{14}Cu_7Ti_5Ta_{74}$ pillar. The characteristic of shear band propagation at a high stress level is the same as the typical shear propagation, a rapid localized plastic deformation. A possible reason would be that the friction between nanoclusters and matrix during propagation might be neglected due to a sufficient energy input from a high applied stress, causing a cooperative movement of STZs.

5-4 Enhancement of mechanical properties of ZrCuTi TFMGs by inserting high-strength nc-Ta layers under microcompression

5-4-1 Thickness effect of nc-Ta layers

In our previous study [114], the measured modulus or yield stress of multilayered micropillars was compared with the calculated values based on the iso-stress rule of mixture (ROM), but the calculated values are usually lower than the measured ones. Using the measured modulus *E* for the ZrCuTi (94 GPa) and Ta (220 GPa), the calculated modulus for the ZrCuTi 50 nm/Ta 5 nm (99 GPa) and ZrCuTi 50 nm/Ta 50 nm (132 GPa) are still lower than the measured ones (106 and 159 GPa for the ZrCuTi 50 nm/Ta 5 nm and ZrCuTi 50 nm/Ta 50 nm, respectively). The same happens to the yield stress. With the yield stress for the ZrCuTi (1.71 GPa) and Ta (5.7 GPa), the calculated yield stress for the ZrCuTi 50 nm/Ta 5 nm (1.82 GPa) and ZrCuTi 50 nm/Ta 50 nm (2.63 GPa) are again lower than the measured (1.90 and 3.15 GPa). The iso-stress ROM systematically underestimates the modulus and yield stress for such amorphous/nanocrystalline multilayered micropillars. We intend to analyze this effect from other aspects.

The simulation on the deformation behavior on metallic glassy alloys indicates that the yield point of metallic glass mainly corresponds to the shear band propagation, not its nucleation [66]. Thus, to probe the underlying reason for the enhancement in initial yield stress of Ta-layer-composited ZrCuTi pillars, it is necessary to consider the conditions needed for shear bands propagation. Similar to crack propagation (Griffith criterion), a shear band can only propagate an incremental distance if the strain energy relief associated with the propagation is more than the energy relief increment of the shear band. Based on this assumption, Volkert et al. [125] deduced an equation to calculate the critical stress required for shear band formation:

$$\sigma = \sqrt{2^{3/2}\kappa E/H}\,, \tag{5-16}$$

where E and H are the Young modulus and the height of the pillar, respectively. The value of κ is estimated to be constant. Eq. 5-16 indicates that the magnitude of critical stress depends on two variables: Young modulus E and the characteristic height H of amorphous geometric objects, namely, $\sigma \propto (E/H)^{1/2}$. Following the physical meaning of this equation, let us firstly estimate the critical stress of ZrCuTi/Ta pillars by taking no account of the contribution of elastic deformation in metallic Ta layers to the propagation of shear band. This is because that the Ta layers are too hard to be deformed when the ZrCuTi layers start to yield. Thus, we have the remaining effective ZrCuTi height for the three pillars: 1.5 μm for the monolithic ZrCuTi pillar, 1.365 μm for the ZrCuTi 50 nm/Ta 5 nm pillar, and 0.75 μm for the ZrCuTi 50 nm/Ta 50 nm pillar, as listed in Table 5-5.

For the monolithic ZrCuTi pillar, in this case, the critical stress can be obtained by the stress-strain curves, that is about 1.71 GPa. Using this value and $\sigma \propto (E/H)^{1/2}$, the critical stress for the ZrCuTi /Ta composited pillars as a function of their effective h and E can be estimated. The theoretically calculated values and the experimentally measured data are compared in Table 5-5. Note that the calculated values on yield stress for the ZrCuTi/Ta composited pillars are in excellent agreement with the measured values, meaning that the

ZrCuTi/Ta composited pillars deform in accordance to the amorphous geometric volume only (not the hard Ta layers). Based on these yield stresses and the elastic strain levels at the yield stress for these three pillars, the elastic energy can be calculated, as also compared in Table 5-5. It can be seen that increment of yield stress and elastic energy of ZrCuTi/Ta composited pillars is originated mainly from the elastic deformation of ZrCuTi amorphous layers during its initial compressive stage. The hard Ta layers did not contribute any for the elastic energy increment.

5-4-2 Shear band propagation of Ta layer in a-ZrCuTi 50 nm/nc-Ta 50 nm micropillar

Figure 5-31 shows the high-magnification TEM bright field image of the deformed ZrCuTi/Ta composited pillars. For the ZrCuTi 50 nm/Ta 5 nm pillar compressed to the elastic-to-shear transition strain level, it is found that although the Ta layers are broken completely in accommodating the pass-through of shear bands, several shear bands have resided in the interior of sample, as marked by the white line in the Fig. 5-31(a). This means that the 5 nm-thick Ta layers could somehow retard the shear band propagation by the shear-through (or breakage) of the thin Ta layers. This can be evidenced by the observation on the deformed ZrCuTi 50 nm/Ta 50 nm composited pillar before the happening of penetrated shear banding events, as shown in Fig. 5-27(b), which shows that no shear band is visible in the interior of the pillar. However, a lot of minor shear steps could be observed at the ZrCuTi 50 nm/Ta 50 nm layer interfaces as marked by the white arrows in Fig. 5-31(b), meaning that the shear behavior has happened. Furthermore, the angles between the shear trace and the pillar top surface are also more than 45^{o}, which is in agreement with what has been reported for amorphous alloys under compression [126].

In previous literatures [127-129], there was no apparent shear event happening in the 10 nm-thickness metallic glass layers geometrically confined by crystalline layers. However, for the current 50 nm-thickness metallic glass layers, the shear events are still the main deformation route, but the inclusion of Ta layers could mediate the deformability of the ZCT/Ta composited pillars by modifying shear band propagation behavior in amorphous ZrCuTi layers.

Moreover, by establishing the variation of the strain rate ($dh/h_o \cdot dt$) as a function of time, the formation as well as subsequent propagation of shear bands can be described. As shown in Fig. 5-32, the strain rate for the ZrCuTi 50 nm/Ta 50 nm remains at 4×10^{-4} s^{-1} up to about 100 s. The strain rate at the engineering stress of 3.2 GPa rises to 6×10^{-4} s^{-1}. At 4 GPa, the strain rate, moreover, starts to speed up at 130 s. Finally, while the stress reaches 4.5 GPa, the strain burst happens at 140 s. Compared with the rapid propagation of the shear band in the monolithic amorphous alloys, as shown in Fig. 5-24, the strain-rate evolution of the strain burst is another evidence that Ta layers could retard effectively the propagation of shear bands.

Now we analyze the underlying physical mechanisms of positive effects of Ta layer on the propagation of shear bands in ZCT/Ta composited layers. Due to the significantly elastic mismatch effects, a stress concentration should arise at the amorphous ZrCuTi/Ta interface upon compression, which makes the interface being a preferentially initiation site for shear band formation. On the other hand, the microcrack-like shear bands would interact with the ductile Ta layers during the propagation process. Following classical fracture mechanics, when a crack initiated in one block approaches the interface, it may penetrate the other block or deflect along the interface. Based on the mechanical modes on ductile-brittle layers composites [124,130], the propagation way for a crack located in a brittle layer with its crack approaching to a ductile layer depends on the magnitude of a non-dimension quantity: σ/σ_0, the ratio of the applied stress σ to the uniaxial yield strength of the crystalline metal material σ_0. For the case of $\sigma/\sigma_0<1$, penetrating way applies; otherwise, deflecting way applies [130]. For this, the uniaxial yield strength of the monolithic Ta pillar with micrometer length has been measured to be 5.7 GPa in our parallel study. Thus, for 50ZCT/5Ta and 50ZCT/50Ta composited pillars, the $\sigma/\sigma_0<1$ is obtained for both cases, so the microcrack-like shear bands choose preferably the way to pass through the Ta layer rather than deflecting along the interface, in agreement with the TEM observations in Fig. 5-31(a). The penetrating way exhibits relatively large stress concentration and is expected to result in local load sharing which is beneficial for the formation of multiple shear bands.

However, for the amorphous ZrCuTi 50 nm/Ta 50 nm multilayers, the shear bands extended into Ta layer in the form of shear steps but do not propagate through the Ta layers in the elastic-to-shear stage, as shown in Fig. 5-31(b). This means that the 50 nm-thickness Ta layers could effectively restrain the propagation of shear bands, in other words, the deformation is realized by shear localization but shear bands do not evolve into cracks. This will happen when the length scale of the glassy phase, i.e., the distance for shear bands propagation becomes comparable with the plastic zone size [131]. Following this idea, it is necessary to figure out the size of plastic zone, R_p for the ZrCuTi/Ta composited pillars. The plastic zone R_p is defined as [132]:

$$\mathrm{R_p} = \mathrm{K}_{\mathrm{IC}}^2/2\pi\sigma_{\mathrm{Y}}^2, \tag{5-17}$$

where K_{IC} is plain-strain fracture toughness and σ_{Y} is the yield strength. In ductile-brittle layers composites, under penetrating way applied conditions [130],

$$K_{IC} = \sigma_Y \sqrt{2\pi \cdot h} \,, \tag{5-18}$$

where *h* is the thickness of plastic-metal layers. Consequently, an estimate of the plastic zone size on the amorphous/metallic laminates from Eqs. 5-17 and 5-18 is given:

$$R_p = h \,. \tag{5-19}$$

This means that the plastic zone of amorphous/crystalline composited pillars equals to the thickness of plastically crystalline layers. For the 50ZCT/50Ta composited pillars, the size of plastic zone R_p (=h=50 nm) is comparable to the characteristic length for shear propagation in the amorphous ZrCuTi constrained layers. Thus, the deformation will occur by shear localization but shear bands do not involve into cracks. However, with the rapid increment of yield stress, the strain energy will increase to a critical value leading to the happen of shear event penetrating the whole pillar. On the other hand, for the ZrCuTi 50 nm/Ta 5 nm composited pillar, the characteristic length for shear propagation is much larger than the R_p (=h=5 nm), accordingly, shear bands can pass through the Ta layers. Nevertheless, the break of Ta layers by extensively plastic deformation can still absorb some kinetic energy of shear bands, and thus reduces the likelihood to form one that is as excessively hot and dangerous as those in monolithic amorphous samples [132].

In evaluating the effects of Ta layers on the propagation of shear bands of amorphous/crystalline composited pillars, a lot of assumptions should be made about the formation and propagation of shear bands. Nevertheless, the basic assumption of microcrack-like shear banding behavior used in our study is acceptable because it is deduced by an energy-driving viewpoint, in which a shear band will only propagate if this results in a reduction in the energy of the system. Thus, energetic arguments can predict directionally the metallic layer-mediated mechanical response in amorphous/crystalline composited pillars, independent of the other detailed assumptions.

Concluding speaking, the analysis of the deformed a-ZrCuTi/nc-Ta nanolaminate micropillar indicates that the deformation always starts from the weakest position. In the a-$Zr_{55}Cu_{31}Ti_{14}$/nc-Ta system, the weaker material is a-$Zr_{55}Cu_{31}Ti_{14}$ layers with an yield strength of ~1.7 GPa. Supposing that the a-$Zr_{55}Cu_{31}Ti_{14}$ layer is the material yielding first, we can estimate a model to describe how a-ZrCuTi/nc-Ta micropillar deforms, as shown in Fig. 5-33. At the initial stage (stage A), there is the micropillar without stress and strain. With increasing stress, the shear bands are initiated at the top a-$Zr_{55}Cu_{31}Ti_{14}$ layer along the shear plane of ~46^{o} to the interface. During the shear band propagation (stage B), the strain reaching ~2% corresponds to the 1st yielding. The nc-Ta layers serve as the obstacle for the shear band propagation. Hence, we can understand that the arising stress is needed to overcome the shear resistance of the obstacle layers. Two types of interaction between a-$Zr_{55}Cu_{31}Ti_{14}$ layers and nc-Ta ones occur. The first type is the deflection of shear band along the layer-layer interfaces [133]. In their calculation, the threshold stress inducing the deflection is much lower than that of shearing [134] This means the deflection of shear bands always occurs at the compressive stress. Another one is the localized shear of the nc-Ta layer caused by the shear bands from the a-layers [135]. At this time, the shear bands start to speed up because of the activation and connection of the shear transition zones. With increasing stress, the nc-Ta layers gradually lose the shear resistance due to the thinner thickness at the position of the shear localization. However, from these results, these two types of the deformation would occur at the same time. At this stage (stage C), the strain reaching ~7% speed up again, implying the nc-Ta layer almost lose the shear resistance. At the last stage

(stage D), the shear bands entirely overcome the obstacle and propagate rapidly, corresponding to the 2nd yielding.

Chapter 6 Conclusion

(1) Utilizing the magnetron sputtering deposition technique, the binary $Zr_{69}Cu_{31}$ thin films were successfully fabricated exhibiting amorphous structure. The measured elastic modulus and hardness are ~96 GPa and 5.1 GPa, respectively.

(2) By adding Ti in ZrCu amorphous matrix, the $Zr_{52}Cu_{29}Ti_{19}$ TFMGs were also fabricated. Comparing between $Zr_{69}Cu_{31}$ TFMGs, The addition of Ti lead to a slightly ~6% improvement both in elastic modulus and hardness.

(3) Utilizing sub-T_g annealing, the hardness of $Zr_{52}Cu_{29}Ti_{19}$ increases from 5.2 GPa to 6.9 GPa (~30% increment). However, the elastic modulus almost remains constant from 102 to 111 GPa, meaning no crystallization occurs during sub-T_g annealing. The hardness increment is attributed to the denser atomic packing due to the annihilation of excess free volume and the formation of medium-range ordering structure. The pronounced increment in strength offers great opportunity for making a stronger MEMS device.

(4) After structural relaxation, a looser, un-relaxed amorphous structure becomes a denser, or relaxed amorphous structure. Due to the absence of excess free volume, relaxed amorphous alloys would activate shear bands easily, leading to more pop-in events occur in relaxed $Zr_{69}Cu_{31}$ and $Zr_{52}Cu_{29}Ti_{19}$ TFMGs.

(5) According to the time-dependent mechanical characteristics of as-deposited and relaxed $Zr_{52}Cu_{29}Ti_{19}$ TFMGs, the non-equilibrium deformed structure (open-volume atomic-size defects) occurring in the loading segment would relax at the holding segment. Whatever the effect of the loading rate in time-dependent nanoindentation tests, the displacement decreases with increasing annealing temperature. This is another indirect evidence to prove the reduction of the excess volume.

(6) To strengthen the amorphous alloys by adding the high-strength Ta, the ZrCuTi

amorphous alloys with immiscible Ta are successfully fabricated via co-sputtering. The glass forming range is up to ~75 at% of immiscible Ta. Compared with similar systems with the addition of immiscible element, the glass forming range via sputtering is much wider than that via liquid-quenching. Also, the mechanical properties are also influenced by the content of immiscible Ta; the elastic modulus and hardness both increase with increasing Ta content. The highest values of elastic modulus and hardness of the current TFMG films (in amorphous structure) reach ~140 GPa and ~10 GPa, respectively.

(7) Except for the W-, Ni-, Co-, and Fe-based amorphous alloys, Ta-based TFMGs exhibit the highest modulus and hardness values. According to TEM observations, no obvious difference is seen in the ZrCuTi-rich and Ta-rich TFMG films. In other words, the topological microstructure would not be the key factor in influencing the micromechanical properties, but the local atomic bonding and packing would impose direct influence. It is considered that the Ta-Ta strong self-bond is responsible for the rapid increase in elastic modulus in the Ta-rich TFMGs.

(8) From structure aspect, many researchers claim that the obstacles, such as particles, precipitates, or reinforcements, usually effectively cease shear band. Through these methods, more shear bands can be initiated at the same time, abating the shear localization. In our case, the role of Ta-rich nanocluster in Ta-rich ZrCuTiTa TFMGs is similar to the mentioned concept. However, Ta-rich nanoclusters do not arrest the shear bands because the cluster size is too small. These nanoclusters in shear bands must move following shear band propagation. The friction between these nanoclusters and matrix exhausts the kinetic energy of shear bands. Shear bands can not propregate immediately. More initiation propagation events of shear bands can are needed to deform, called multiple shear-band characteristic.

(9) The heat by the friction would lead to the relaxation in the region which shear bands pass througth. To initiate another event of shear band in the same position, a higher

stress is needed, called as work-hardening characteristic.

(10) To strengthen the amorphous alloys inserting the high-strength nanocrystalline Layers, the improved mechanical performance has been demonstrated via inserting of high-stiffness Ta layers to form composited microstructure, for micrometer-length amorphous ZrCuTi alloys. Two underlying physical mechanisms are derived to account for this phenomenon: on one hand, the ZrCuTi/Ta composited pillars deform according to the amorphous geometric volume.

(11) On the other hand, different-thickness Ta layers results in different shear behavior by forming equal-thickness plastic zone in the amorphous layers. The higher strength and some plastic flow behavior presented here suggests that the high-stiffness nanocrystalline-amorphous metallic composites approach is a viable route towards developing advanced materials for microelectromechanical system (MEMS) application.

References

[1] A.C. Lund and C A. Schuh, J. Appl. Phys., **95** (2004) 4815-4822.

[2] A. Inoue, A. Kato, T. Zhang, S.G. Kim, and T. Masumoto, Mater. Trans., JIM, **32** (1991) 606-609.

[3] J. Schroers and N. Paton, Adv. Mater. Processes, **164** (2006) 61-63.

[4] P. Sharma, W. Zhang, K. Amiya, H. Kimura, and A. Inoue, Nanoscience and Nanotech., **5** (2005) 416-420.

[5] T. Fukushige, S. Hata, and A. Shimokohbe, J. Microelectromech. Syst., **14** (2005) 243-253.

[6] A. Inoue, Mater. Sci. Eng. A, **304-306** (2001) 1-10.

[7] A. Inoue, Acta Metar., **48** (2000) 279-306.

[8] S. Mader, A.S. Nowick, and H. Widmer, Acta Metall., **15** (1967) 203-214.

[9] S. Bysakh, P.K. Das, and K. Chattopadhyay, Philos. Mag. A, **81** (2001) 2689-2704.

[10] R.B. Schwarz and W.L. Johnson, Phys. Rev. Lett., **51** (1983) 415-418.

[11] S. Hata, K. Sato, and A. Shimokohbe, Proc. SPIE, **3892** (1999) 97-108.

[12] J.P. Chu, C.T. Liu, T. Mahalingam, S.F. Wang, M.J. O'Keefe, B. Johnson, and C.H. Kuo, Phys. Rev. B, **69** (2004) 113410.

[13] Y. Liu, S. Hata, K. Wada, and A. Shimokohbe, Jpn. J. Appl. Phys., **40** (2001) 5382-5388.

[14] M.W. Chen, Annu. Rev. Mater. Res., **38** (2008) 14.1-14.25.

[15] A.S. Argon, Acta Metall., **27** (1979) 47-58.

[16] W. Klement, R. H. Willens, and P. Duwez, Nature, **187** (1960) 869-870.

[17] H.S. Chen and D. Turnbull, Acta Metall., **17** (1969) 1021-1031.

[18] H.S. Chen, Acta Metall., **22** (1974) 1050-1511.

[19] E.J. Cotts, W.J. Meng, and W.L. Johnson, Phys. Rev. Lett., **57** (1986) 2295-2298.

[20] H.W. Kui, A.L. Greer, and D. Turnbull, Appl. Phys. Lett., **45** (1984) 615-616.

[21] Q.M. Chen, Y.D. Fan, and H.D. Li, Mater. Lett., **6** (1988) 311-315.

[22] J. Dudonis, R. Brucas, and A. Miniotas, Thin Solid Films, **275** (1996) 164-167.

[23] H.U. Krebs, O. Brement, M. Stormer, and Y.S. Luo, Appl. Surf. Sci., **86** (1995) 90-94.

[24] J. Sakurai, S. Hata, and A. Shimokohbe, International Conference on Advanced Technology in Experimental Mechanics 2003, (2003) 10-12.

[25] G.P. Zhang, Y. Liu, W. Wang, and J. Tan, Appl. Phys. Lett., **88** (2006) 013105.

[26] G.P. Zhang, Y. Liu, and B. Zhang, Scripta Mater., **54** (2006) 897-901.

[27] R. Yamauchu, S. Hata, J. Sakurai, and A. Shimokohbe, Mater. Res. Soc, Symp. Proc., **894** (2006) 0894-LL02-05.1-0894-LL02-05.5.

[28] S. Hata, T. Fukushige, and A. Shimokohbe, Proceedings of CPT2002, (2002) 162-167.

[29] G.P. Zhang, Y. Liu, and B. Zhang, Adv. Eng. Mater., **7** (2005) 606-609.

[30] A. Inoue, T. Nakamura, and N. Nishiyama, Mater. Trans., JIM, **33** (1992) 937-945.

[31] Z.P. Lu, H. Tan, Y. Li, and S.C. Ng, Scripta Mater., **42** (2000) 667-673.

[32] Z.P. Lu and C.T. Liu, Acta Metar., **50** (2002) 3501-3512.

[33] X.H. Du, J.C. Huang, C.T. Liu, and Z.P. Liu, J. Appl. Phys., **101** (2007) 086108.

[34] A. Inoue, T. Zhang, and Tsuyoshi, Mater. Trans., JIM, **30** (1989) 965-972.

[35] Z.P. Lu and C.T. Liu, Intermetallics, **12** (2004) 1035-1043.

[36] 吳學陞, 工業材料, **149** (1999) 154-165.

[37] W. Buckel, Z. Phys., **138** (1954) 136-150.

[38] B.X. Liu, Mater. Lett., **5** (1987) 322-327.

[39] Y.G. Chen and B.X. Liu, Appl. Phys. Lett., **68** (1996) 3096-3098.

[40] Y.G. Chen and B.X. Liu, J. Phys .D:Appl. Phys., **30** (1997) 510-516.

[41] Y.P. Deng, Y.F. Guan, J.D. Fowlkes, S.Q. Wen, F.X. Liu, G.M. Pharr, P.K. Liaw, C.T. Liu, and P.D. Rack, Intermetallics, **15** (2007) 1208-1216.

[42] H.M. Chen, Y.C. Chang, T.H. Hung, X.H. Du, J.C. Huang, J.S.C. Jang, and P.K. Liaw, Mater. Trans., **48** (2007) 1802-1805.

[43] T.G. Nieh, T.W. Barbee, and J. Wadsworth, Scripta Mater., **41** (1999) 929-935.

[44] J. Rivory, J.M. Frigerio, M. Harmelin, A. Quivy, Y. Calvayrac, and J. Bigot, Thin Solid Films, **89** (1982) 323-327.

[45] F. Pan and B.X. Liu, J. Phys.: Condens. Matter, **8** (1996) 383-388.

[46] R.F. Zhang, Z.C. Li, and B.X. Liu, Jpn. J. Appl. Phys., **42** (2003) 7009-7012.

[47] E. Ma and M. Atzmon, Mater. Chem. Phys., **39** (1995) 249-267.

[48] S. Ohsaki, S. Kato, N. Tsuji, T. Ohkubo, and K. Hono, Acta Mater., **55** (2007) 2885-2895.

[49] R. Banerjee, S. Bose, A. Genc, and P. Ayyub, J. Appl. Phys., **103** (2008) 033511.

[50] N.A. Mara, D. Bhattacharyy, R.G. Hoagland, and A. Misra, Scripta Mater., **58** (2008) 874-877.

[51] N.A. Mara, T. Tamayo, A.V. Sergueeva, X. Zhang, A. Misra, and A.K. Mukherjee, Thin Solid Films, **515** (2007) 3241-3245.

[52] H.L. Knoedler, G.E. Lucas, and C.G. Levi, Mater. Trans. A, **34A** (2003) 1043-1054.

[53] K.W. Kwon, H.J. Kee, and R. Sinclair, Appl. Phys. Lett., **75** (1999) 935-937.

[54] S. Gohil, R. Banerjee, S. Bose, and P. Ayyub, Scripta Mater., **58** (2008) 842-845.

[55] P. Taneja, R. Banerjee, and P. Ayyub, Phys. Rev. B, **64** (2001) 033405.

[56] F. Zeng, Y. Gao, L. Li, D.M. Li, and F. Pan, J. Alloys Compd., **389** (2005) 75-79.

[57] A. Misra and R.G. Hoagland, J. Mater. Res., **20** (2005) 2046-2054.

[58] C. Michaslsen, C. Gente, and R. Bormann, J. Appl. Phys., **81** (1997) 6024-6030.

[59] A. Puthucode, M.J. Kaufman, and R. Banerjee, Mater. Trans. A, **39A** (2008) 1578-1584.

[60] D. Kawase, A.P. Tsai, A. Inoue, and T. Masumoto, Appl. Phys. Lett., **62** (1992) 137-139.

[61] B. Gun, K.J. Laws, and M. Ferry, J. Non-cryst. Solids, **352** (2006) 3887-3895.

[62] C.A. Schuh, T.C. Hufnagel, and U. Ramamurty, Acta Mater., **55** (2007) 4067-4109.

[63] A.V. Sergueeva, N.A. Mara, J.D. Kuntz, E.J. Lavernia, and A.K. Mukherjee, Philo. Mag., **85** (2005) 2671-2687.

[64] X.K. Xi, D.Q. Zhao, M.X. Pan, W.H. Wang, Y. Wu, and J.J. Lewandowski, Phys. Rev. Lett., **94** (2005) 125510.

[65] F.H. Dalla Torre, A. Dubach, J. Schallibaum, and J.F. Loffler, Acte Mater., **56** (2008) 4635-4646.

[66] F. Shimizu, S. Ogata, and J. Li, Acta Mater., **54** (2006) 4293-4298.

[67] W. C. Crone, H. Brock, and A. Creuziger, Exp. Mech., **47** (2007) 133-142.

[68] H. Ljungcrantz, M. Oden, L. Hultman, J.E. Greene, and J.E. Sundgren, J. Appl. Phys., **80** (1996) 6725-6733.

[69] J. Chen, W. Wang, L.H. Qian, and K. Lu, Scripta Mater., **49** (2003) 645-650.

[70] S.Y. Chang, Y.K. Chang, and Y.S. Lee, Electrochem. Solid-State Lett., **9** (2006) C73-C76.

[71] A.L. Greer, A. Castellero, S.V. Madge, I.T. Walker, and J.R. Wilde, Mater. Sci. Eng. A, **375-377** (2004) 1182-1185.

[72] F. Spaepen, Acta Metall., **25** (1977) 407-415.

[73] W.C. Oliver and G.M. Pharr, J. Mater. Res., **7** (1992) 1564-1583.

[74] R.L. Zong, S.P. Wen, F. Zeng, Y. Gao, and F. Pan, J, Alloys Compd., **464** (2007) 544-549.

[75] S. Reyntjens and R. Puers, J. Micromech. Microeng., **11** (2001) 287-300.

[76] A. Misra, Z.L. Wu, M.T. Kush, and R. Gibala, Philo. Mag. A, **78** (1998) 533-550.

[77] H. Bei and E.P. George, Acta Mater., **53** (2005) 69-77.

[78] H. Bei, S. Shim, E.P. George, M.K. Miller, E.G. Herbert, and G.M. Pharr, Scripta Mater., **57** (2007) 397-400.

[79] S.S. Brenner, J. Appl. Lett., **27** (1956) 1484-1956.

[80] S.S. Brenner, J. Appl. Phys., **28** (1957) 1023-1026.

[81] A.H. Clauer, B.A. Wilcox, and J.P. Hirth, Acta Mater., **18** (1970) 367-379.

[82] G. Simmons and H. Wang, Single Crystal Elastic Constants and Calculated Aggregate Properties - A Handbook, MIT Press, Conbridge, Massachusetts, 1971.

[83] A.H. Cottrell, Dislocations and Plastic Flow in Crystals, Clarendon Press, Oxford, 1953.

[84] R.W.K. Honeycombe, Plastic Deformation of Metals, Second ed., Edward Arnold, London, 1984.

[85] Y.H. Lai, C.J. Lee, Y.T. Cheng, H.S. Chou, H.M. Chen, X.H. Du, C.I. Chang, J.C. Huang, S.R. Jian, J.S.C. Jang, and T.G. Nieh, Scripta Mater., **58** (2008) 890-893.

[86] J.J. Lewandowski, W.H. Wang, and A.L. Greer, Philo. Mag. Lett., **85** (2005) 77-87.

[87] R.D. Conner, R.B. Dandliker, and W.L. Johnson, Acta Mater., **46** (1998) 6089-6102.

[88] J.S.C. Jang, J.Y. Ciou, T.H. Hung, J.C. Huang, and X.H. Du, Appl. Phys. Lett., **92** (2008) 011930.

[89] Z.Z. Tang, J.H. Hsieh, S.Y. Zhang, C. Li, and Y.Q. Fu, Surf. Coat. Technol., **198** (2005) 110-113.

[90] O.J. Kwon, Y.K. Lee, S.O. Park, J.C. Lee, Y.C. Kim, and E. Fleury, Mater. Sci. Eng. A, **449-451** (2007) 169-171.

[91] Y.T. Shen, L.Q. Xing, and K.F. Kelton, Philo. Mag., **85** (2005) 3673-3682.

[92] G. He, Z. Bian, and G. L. Chen, Mater. Sci. Eng. A, (1999) 291-298.

[93] H.H. Liebermann and F.E. Luborsky, Acta Metall., **29** (1981) 1413.

[94] U. Ramamurty, M.L. Lee, J. Basu, and Y. Li, Scripta Mater., **47** (2002) 107-111.

[95] P. Murali and U. Ramamurty, Acta Mater., **53** (2005) 1467-1478.

[96] T. Egami and Y. Waseda, J. Non-cryst. Solids, **64** (1984) 113-134.

[97] F.R. de Boer, R. Boom, W.C.M. Mattens, A.R. Miedema, and A.K. Niessen, Cohesion

in Metals, North-Holland, New York, 1988.

[98] W.C. Oliver and G.M. Pharr, J. Mater. Res., **19** (2004) 3-20.

[99] A.R. Yavari, A.L. Moulec, A. Inoue, N. Nishiyama, N. Lupu, E. Matsubara, W.J. Botta, G. Vaughan, M.D. Michel, and A. Kvick, Acta Mater., **53** (2005) 1611-1619.

[100] H.S. Chou, J.C. Huang, L.W. Chang, and T.G. Nieh, Appl. Phys. Lett., **93** (2008) 191901.

[101] X.J. Liu, G.L. Chen, H.Y. Hou, X. Hui, K.F. Yao, Z.P. Liu, and C.T. Liu, Acta Mater., **56** (2008) 2760-2769.

[102] Y. Hirotsu, T.G. Nieh, A. Hirata, T. Ohkubo, and N. Tanaka, Phys. Rev. B, **73** (2006) 012205.

[103] A. Inoue, H.M. Kimura, and T. Zhang, Mater. Sci. Eng., **294-296** (2000) 727-735.

[104] J. Sieetsma and B.J. Thijsse, Phys. Rev. B, **52** (1995) 3248-3255.

[105] D.B. Miracle, T. Egami, K.M. Flores, and K.F. Kelton, Mater. Res. Soc. Bulletin, **32** (2007) 629-634.

[106] K.M. Flores, E. Sherer, A. Bharathula, H. Chen, and Y.C. Jean, Acta Mater., **55** (2007) 3403-3411.

[107] C.A. Schuh, A.C. Lund, and T.G. Nieh, Acta Mater., **52** (2004) 5879-5891.

[108] B.G. Yo, J.H. Oh, Y.J. Kim, K.W. Park, J.C. Lee, and J.I. Jang, Intermetallics, **18** (2010) 1898-1901.

[109] D. Suh, R.H. Dauskardt, P. Asoka-Kumar, P.A. Sterne, and R.H. Howell, J. Mater. Res., **17** (2002) 1153-1161.

[110] A. Castellero, B. Moser, D.I. Uhlenhaut, F.H. Dalla Torre, and J.F. Loffler, Acta mater., **56** (2008) 3777-3785.

[111] L. Charleux, S. Gravier, M. Verdier, M. Fivel, and J.J. Blandin, J. Mater. Res., **22** (2007) 525-532.

[112] M. Ohtsuki, R. Tamura, S. Takeuchi, S. Yoda, and T. Ohmura, Appl. Phys. Lett., **84**

(2004) 4911-4913.

[113] J.J. Olivero and R.L. Longbothum, J. Quant. Spec. and Rad. Trans., **17** (1977) 233-236.

[114] M.C. Liu, J.C. Huang, H.S. Chou, Y.H. Lai, C.J. Lee, and T.G. Nieh, Scripta Mater., **61** (2009) 840-843.

[115] T.H. Fang and W.J. Chang, Microelec. Eng., **65** (2003) 231-238.

[116] F.K. Mante, G.R. Baran, and B. Lucas, Biomaerials, **20** (1999) 1051-1055.

[117] S. Benlekbir, Ph.D. Thesis, STEM-HAADF nanotomography:application to nanomaterials, French engineering university Lyon, 2009

[118] K.W. Park, J.I. Jang, M. Wakeda, Y.J. Shibutanic, and J.C. Lee, Scripta Mater., **57** (2007) 805-808.

[119] H.R. Wang, Y.F. Ye, Z.Q. Shi, X.Y. Teng, and G.H. Min, J. Non-cryst. Solids, **311** (2002) 36-41.

[120] H.S. Chou, J.C. Huang, and L.W. Chang, Surf. Coatings Technol., **205** (2010) 587-590.

[121] W.L. Johnson and K. Samwer, Phys. Rev. Lett., **95** (2005) 195501.

[122] D. Pan, A. Inoue, T. Sakurai, and M.W. Chen, Proc. Nat. Acad. Sci., **105** (2008) 14769-14772.

[123] S. Pauly, S. Gorantla, G.Wang, U. Kühn, and J. Eckert, Nature Mater., **9** (2010) 473-477.

[124] D.C. Hofmann, J.Y. Suh, A.Wiest, G. Duan, M.L. Lind, M.D. Demetriou, and W.L. Johnson, Nature, **451** (2008) 1085-1089.

[125] C.A. Volkert, A. Donohue, and F. Spaepen, J. Appl. Phys., **103** (2008) 083539.

[126] H.C. Cao and A.G. Evans, Acta Mater., **39** (1991) 2997-3005.

[127] Y. Wang, J. Li, A.V. Hamza, and T.W. Barbee Jr., Proc. Natl. Acad. Sci., **104** (2007) 11155-11160.

[128] T.G. Nieh and J. Wadsworth, Intermetallics, **16** (2008) 1156-1159.

[129] C.A. Volkert and E.T. Lilleodden, Philo. Mag., **86** (2006) 5567-5579.

[130] A.G. Evans, M.C. Lu, S. Schmauder, and M. Ruhle, Acta Metall., **34** (1986) 1643-1655.

[131] R.D. Conner, W.L. Johnson, N.E. Paton, and W.D. Nix, J. Appl. Phys., **94** (2003) 904-911.

[132] C. Fan, H.Q. Li, L.J. Kecskes, K.X. Tao, H. Choo, P.K. Liaw, and C.T. Liu, Phys. Rev. Lett., **96** (2006) 145506.

[133] T.C. Hufnagel, C. Fan, R.T. Ott, J. Li, and S. Brennan, Intermetallics, **10** (2002) 1163-1166.

[134] S.Y. Kuan, H.S. Chou, M.C. Liu, X.H. Du, and J.C. Huang, Intermetallics, **18** (2010) 2453-2457.

[135] Y.M. Wang, A.M. Hodge, P.M. Bythow, T.W. Barbee Jr., and A.V. Hamza, Appl. Phys. Lett., **89** (2006) 081903.

Table 2-1 Summary of compressive yield strengths obtained in this study for molybdenum alloy micropillars of various sizes [78].

Nominal pillar size, a (μm)	Number of valid tests	Measured area, A (μm^2)	Compressive yield strength (GPa)
1.00	5	1.00 ± 0.02	9.17 ± 0.44
0.75	4	0.58 ± 0.02	9.24 ± 0.77
0.50	12	0.26 ± 0.02	9.30 ± 0.48
0.36	9	0.13 ± 0.02	9.18 ± 1.16

[a] Area were not measured for individual tests but based on 36 randomly chosen pillars.

Table 2-2 Summary of the compressive stress/elastic modulus of the $Zr_{63.5}Ni_{16.2}Cu_{15}Al_5$ glass at different rates [85].

Sample size	$\dot{\varepsilon} \sim 1 \times 10^{-4}\ s^{-1}$	$\dot{\varepsilon} \sim 1 \times 10^{-3}\ s^{-1}$	$\dot{\varepsilon} \sim 1 \times 10^{-2}\ s^{-1}$
Bulk 2 mm	1600 MPa/80~90 GPa	1712 MPa/--	1847 MPa/--
3.8 μm	2088 MPa/77 GPa	1992 MPa/80 GPa	2054 MPa/79 GPa
1 μm	2496 MPa/63 GPa	2357 MPa/81 GPa	2365 MPa/85 GPa
700 nm	2972 MPa/81 GPa	2590 MPa/88 GPa	2733 MPa/72 GPa

Table 3-1 Detail of the fabricated alloy thin films.

Specimen name	Process	Condition			Thickness (nm)
		Zr	Cu	Ti	
$Zr_{69}Cu_{31}$	Co-sputtering	DC 305 W	Cu DC 50 W	N/A	~2000
$Zr_{52}Cu_{29}Ti_{19}$	Co-sputtering	DC 250 W	Cu 200 W	DC 140 W	~2200

Specimen name	Process	ZrCuTi	Ta	Thinkness
$Zr_{55}Cu_{31}Ti_{14}$	Alloy deposition	ZrCuTi DC 300W	N/A	~2000
Ta	deposition	N/A	Ta DC 300W	~2400
$Zr_{45}Cu_{27}Ti_{15}Ta_{13}$	Co-sputtering	ZrCuTi DC 300W	Ta DC 50W	~2200
$Zr_{41}Cu_{23}Ti_{12}Ta_{24}$	Co-sputtering	ZrCuTi DC 300W	Ta DC 100W	~2200
$Zr_{31}Cu_{15}Ti_{10}Ta_{44}$	Co-sputtering	ZrCuTi DC 300W	Ta DC 200W	~2400
$Zr_{23}Cu_{12}Ti_{8}Ta_{57}$	Co-sputtering	ZrCuTi DC 300W	Ta DC 300W	~2400
$Zr_{19}Cu_{6}Ti_{7}Ta_{68}$	Co-sputtering	ZrCuTi DC 200W	Ta DC 300W	~2200
$Zr_{14}Cu_{7}Ti_{5}Ta_{74}$	Co-sputtering	ZrCuTi DC 150W	Ta DC 300W	~2200
$Zr_{9}Cu_{5}Ti_{3}Ta_{83}$	Co-sputtering	ZrCuTi DC 100W	Ta DC 300W	~2200
$Zr_{4}Cu_{3}Ti_{1}Ta_{92}$	Co-sputtering	ZrCuTi DC 50 W	Ta DC 300W	~2200
ZrCuTi/Ta 50/50	Alternative deposition	ZrCuTi DC 300W	Ta DC 200W	~1600
ZrCuTi/Ta 50/5	Alternative deposition	ZrCuTi DC 300W	Ta DC 200W	~1600

Table 3-2 Microcompression test condition in a sereies of Zr-based TFMGs and nanolaminate.

Material	Final peak load (mN)	Loading time (s)
$Zr_{52}Cu_{29}Ti_{19}$	2	120
$Zr_{45}Cu_{27}Ti_{15}Ta_{13}$	2	120
$Zr_{31}Cu_{15}Ti_{10}Ta_{44}$	2	120
$Zr_{14}Cu_{7}Ti_{5}Ta_{74}$	3	180
nc-Ta	4	120
$Zr_{55}Cu_{31}Ti_{14}$ 50 nm/ Ta 50 nm	3	180
$Zr_{55}Cu_{31}Ti_{14}$ 50 nm/ Ta 5 nm	2	120

Table 4-1 Basic properties of zirconium, copper, titanium, tantalum.

	Density (g/cm^3)	Atomic weight	Atomic radii (Å)	Melting point (K)	Elastic modulus (GPa)
Zr	6.51	91.22	1.58 [92]	2125	129 [114]
Cu	8.92	63.55	1.27 [92]	1356	135 [115]
Ti	4.507	47.87	1.46 [92]	1933	128 [116]
Ta	16.65	180.95	1.49 [92]	3269	221 [120]

Table 4-2 Heat of mixing among Zr, Cu, Ti, and Ta [97]. The unit is kJ/mole.

	Zr	Cu	Ti	Ta
Zr		-23	0	+3
Cu	-23		-9	+2
Ti	0	-9		+1
Ta	+3	+2	+1	

Table 4-3 Elastic modulus of ZrCuTiTa alloy thin film at 0.05, 0.1, 0.5, 1 mNs^{-1}.

Materials	Elastic modulus (GPa)			
	0.05 mNs^{-1}	0.1 mNs^{-1}	0.5 mNs^{-1}	1 mNs^{-1}
$Zr_{55}Cu_{31}Ti_{14}$	93.5±1.79	94.3±2.60	93.9±1.28	97.9±1.31
$Zr_{45}Cu_{27}Ti_{15}Ta_{13}$	99.8±2.10	99.4±2.38	97.9±1.85	102.5±1.68
$Zr_{41}Cu_{23}Ti_{12}Ta_{24}$	103.6±4.08	101.1±2.91	102.2±3.07	106.2±3.78
$Zr_{31}Cu_{15}Ti_{10}Ta_{44}$	103.2±2.60	104.2±2.17	104.2±0.93	103.8±4.09
$Zr_{23}Cu_{12}Ti_{8}Ta_{57}$	109.9±2.21	108.0±2.55	110.6±2.32	113.8±1.49
$Zr_{19}Cu_{6}Ti_{7}Ta_{68}$	125.7±2.28	126.0±1.68	124.7±1.11	129.5±1.80
$Zr_{14}Cu_{7}Ti_{5}Ta_{74}$	139.9±3.80	135.8±2.69	139.22.19±	143.4±2.67
$Zr_{10}Cu_{5}Ti_{3}Ta_{82}$	174.5±3.36	171.5±4.45	177.0±4.79	172.9±4.54
$Zr_{4}Cu_{3}Ti_{1}Ta_{92}$	203.4±6.25	201.8±4.45	208.1±4.88	206.2±5.20
Nanocrystalline Ta	220.7±4.70	218.2±4.14	218.7±5.46	229.3±4.68

Table 4-4 Hardness of ZrCuTiTa alloy thin film at 0.05, 0.1, 0.5, 1 mNs^{-1}.

Materials	Hardness (GPa)			
	0.05 mNs^{-1}	0.1 mNs^{-1}	0.5mNs^{-1}	1 mNs^{-1}
$Zr_{55}Cu_{31}Ti_{14}$	5.2±0.13	5.4±0.11	5.2±0.11	5.2±0.11
$Zr_{45}Cu_{27}Ti_{15}Ta_{13}$	6.3±0.19	6.3±0.19	6.0±0.13	5.7±0.18
$Zr_{41}Cu_{23}Ti_{12}Ta_{24}$	6.9±0.28	6.8±0.31	6.9±0.28	6.7±0.20
$Zr_{31}Cu_{15}Ti_{10}Ta_{44}$	7.3±0.24	7.5±0.19	7.2±0.27	6.67±0.31
$Zr_{23}Cu_{12}Ti_8Ta_{57}$	7.6±0.25	7.5±0.32	7.4±0.28	7.4±0.22
$Zr_{19}Cu_6Ti_7Ta_{68}$	9.0±0.09	9.0±0.17	8.9±0.14	8.6±0.12
$Zr_{14}Cu_7Ti_5Ta_{74}$	10.0±0.14	10.0±0.18	10.0±0.30	9.7±0.23
$Zr_{10}Cu_5Ti_3Ta_{82}$	15.9±0.50	16.0±0.47	16.0±0.50	14.6±0.40
$Zr_4Cu_3Ti_1Ta_{92}$	18.8±0.48	19.0±0.77	18.5±0.53	17.8±0.58
Nanocrystalline Ta	20.0±0.4	19.8±0.90	20.2±0.94	20.0±0.67

Table 4-5 Mechanical properties of ZrCuTiTa TFMG and ZrCuTi/Ta multilayered micropillars via microcompression tests.

Material	$\dot{\varepsilon}$ (s^{-1})	E (GPa)	σ_y (GPa)	σ_y/E
$Zr_{55}Cu_{31}Ti_{14}$	4.8x10^{-4}	89.9	1.74	0.019
$Zr_{45}Cu_{27}Ti_{15}Ta_{13}$	3.7x10^{-4}	98.5	2.08	0.021
$Zr_{31}Cu_{15}Ti_{10}Ta_{44}$	3.7x10^{-4}	87.2	2.18	0.025
$Zr_{14}Cu_{7}Ti_{5}Ta_{74}$	3x10^{-4}	145.1	3.26	0.02
Nanocrystalline Ta	4x10^{-4}	170.0	5.77	0.03
ZCT 50 nm/Ta 5 nm	4x10^{-4}	106.7	1.91	0.018
ZCT 50 nm/Ta 50 nm	4x10^{-4}	158.8	3.12	0.02

Table 5-1 Basic properties Zr, Cu, Ti, β-Ta and $Zr_{55}Cu_{31}Ti_{14}$.

	Atomic weight	Structure	Melting point (k)	E (GPa)	H (GPa)
Zr	91.22	HCP	2125	129 [114]	5.22 [114]
Cu	63.55	FCC	1356	135 [115]	1.7-2.8 [115]
Ti	47.87	HCP	1933	128 [116]	2.11 [116]
$Zr_{55}Cu_{31}Ti_{14}$	76.57[a]	amorphous	--	94	5.21
β-Ta	180.95	tetragonal	3269	221	20.05

[a] is estimated from

[b] is the glass transition point

Table 5-2 Estimation of elastic modulus and hardness in ZrCuTi/Ta multilayer thin films.

Samples	Voigt model		Reuss model		Experiments	
	E (GPa)	H (GPa)	E (GPa)	H (GPa)	E (GPa)	H (GPa)
ZrCuTi 50 nm/Ta 50 nm	157.1	12.6	131.4	8.3	137.9	8.0
ZrCuTi 50 nm/Ta 5 nm	99.9	6.0	96.3	5.4	106.3	5.0

Table 5-3 Point analysis of $Zr_{41}Cu_{23}Ti_{12}Ta_{24}$ TFMG.

$Zr_{41}Cu_{23}Ti_{12}Ta_{24}$	Composition (at%)			
	Zr	Cu	Ti	Ta
White domain	41.5±1.10	20.6±2.42	11.8±1.72	26.5±1.05
Black domain	40.7±1.97	19.2±2.04	11.5±2.88	28.7±0.82

Table 5-4 Point analysis of $Zr_{31}Cu_{15}Ti_{10}Ta_{44}$ TFMG.

$Zr_{31}Cu_{15}Ti_{10}Ta_{44}$	Composition (at%)			
	Zr	Cu	Ti	Ta
White domain	31.5±3.70	13.8±3.10	10.3±2.75	44.5±3.70
Black domain	32.0±2.94	12.5±4.51	10.0±2.16	45.5±1.00

Table 5-5 The comparison of the theoretically calculated values and the experimentally measured data for ZrCuTi/Ta composited pillars.

Materials	Young's modulus, GPa	ZCT height in pillar, H, μm	H/H_{ZCT}	Calculated yield stress, GPa	Measured yield stress, GPa	Elastic energy, 10^7 J/m^3
ZCT	94	1.5	1	–	1.71	2.62
50ZCT/5Ta	106	1.365	0.91	1.90	1.91	2.82
50ZCT/50Ta	159	0.75	0.5	3.15	3.20	6.2

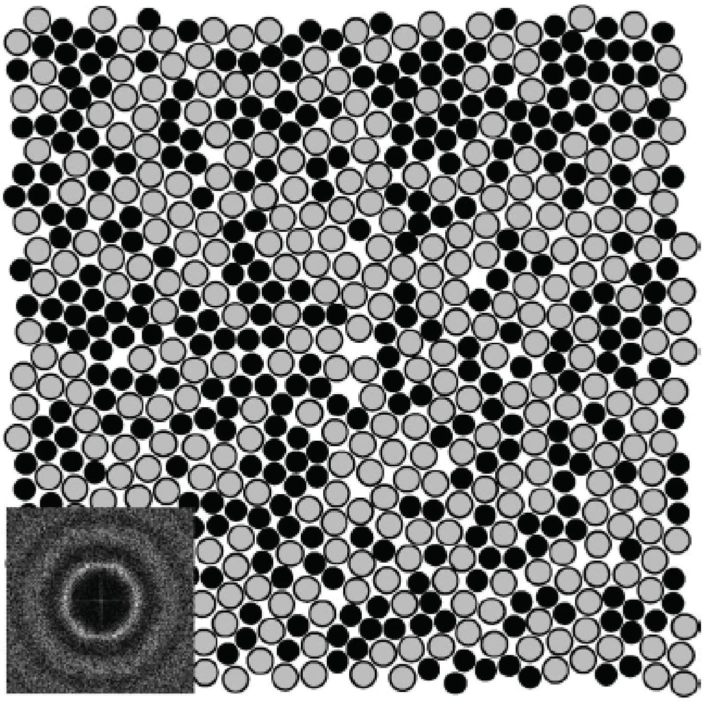

Fig. 1-1 A scheme of short-range-ordered structure [1].

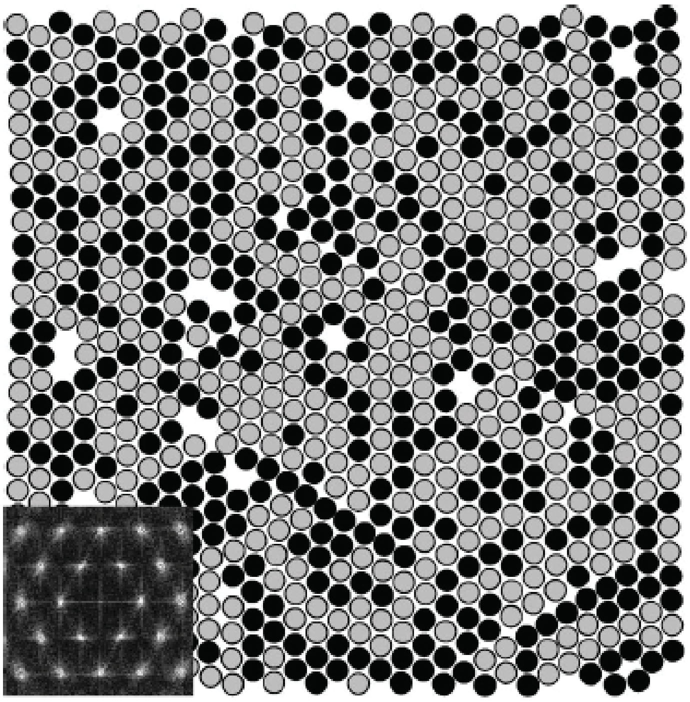

Fig. 1-2 A scheme of long-range-ordered structure [1].

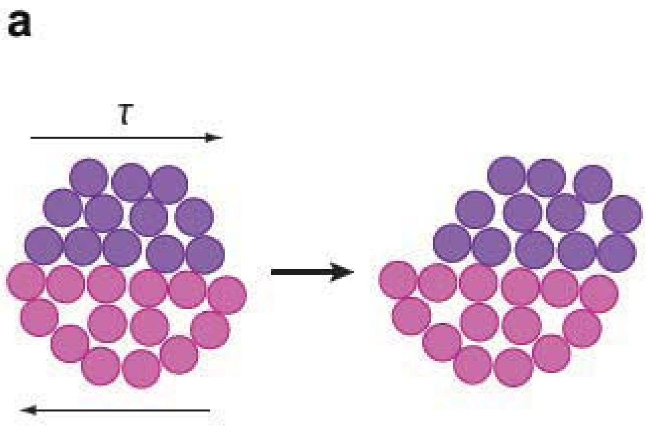

Fig. 1-3 Scheme of the shear transformation zone under shear deformation [3].

Fig. 1-4 The frame for the upscale models of the Vertu mobile phone is made of liquidmetal alloy because of its high strength, hardness, and scratch resistance [4].

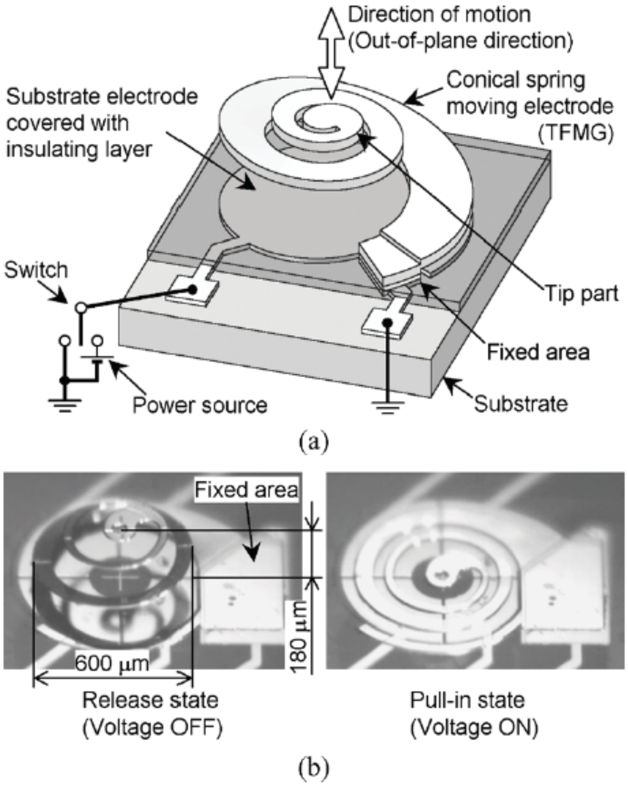

Fig. 1-5 (a) A sketch of conical spring microactuator, and (b) a fundamental structure of micro-switch made by metallic glass thin films [5].

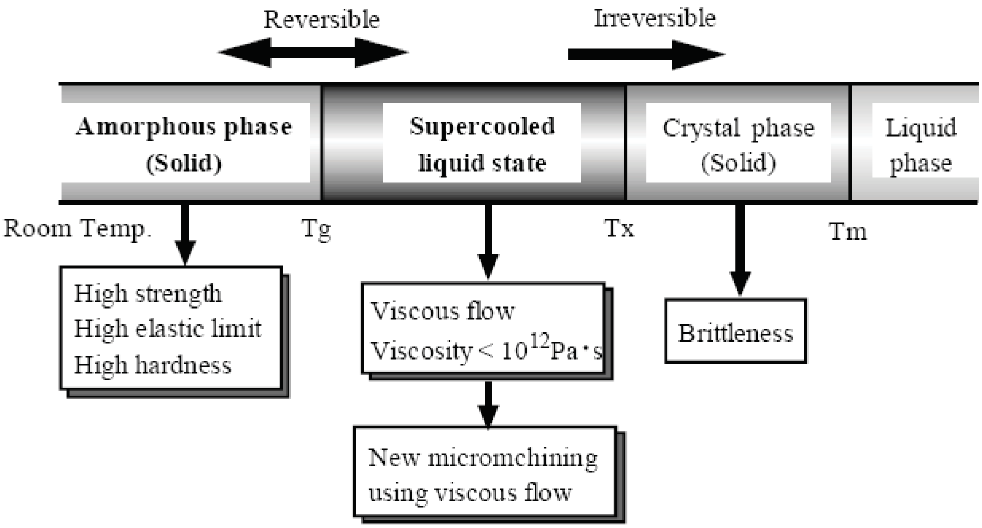

Fig. 2-1 Characteristics of metallic glasses [32].

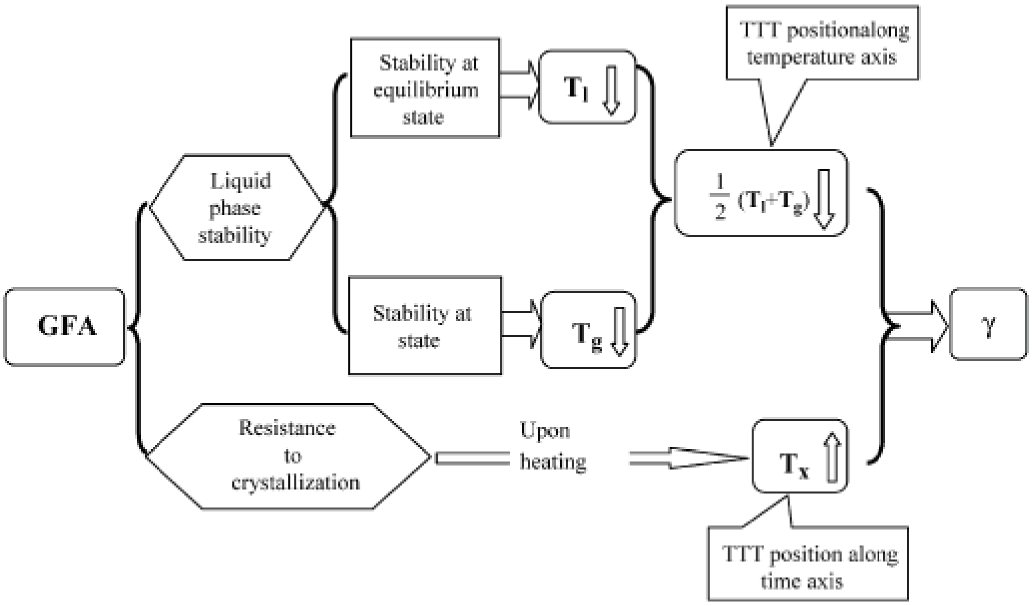

Fig. 2-2 New approach for understanding GFA of amorphous materials [35].

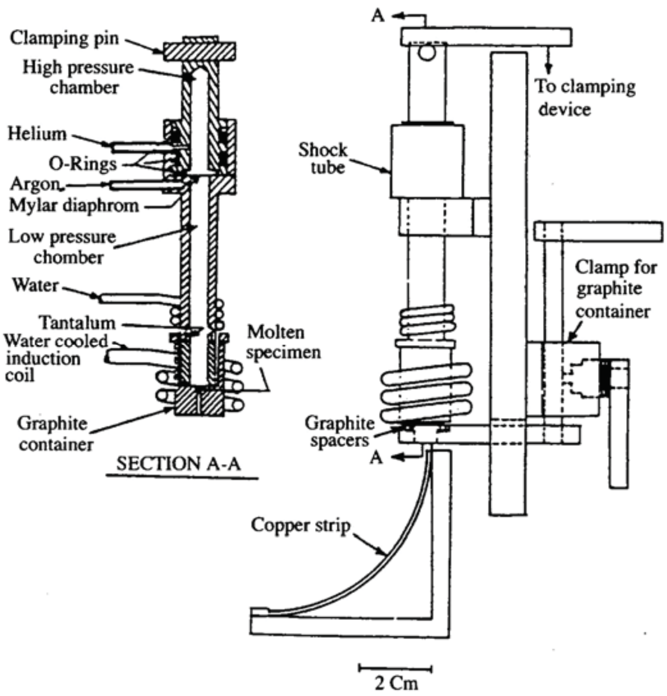

Fig. 2-3 A schematic diagram of the splat quenching methods [36].

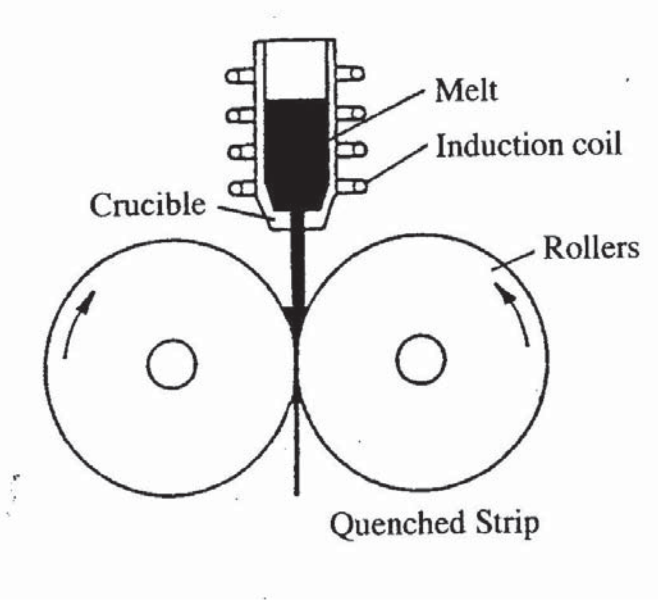

Fig. 2-4 A schematic diagram of the two roller quenching method [36].

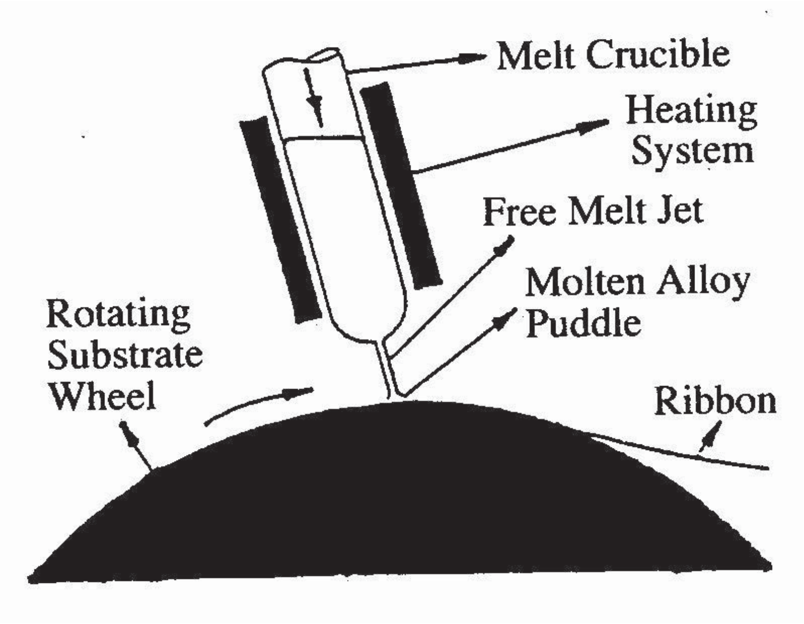

Fig. 2-5 A schematic diagram of the chill block melt spinning [36].

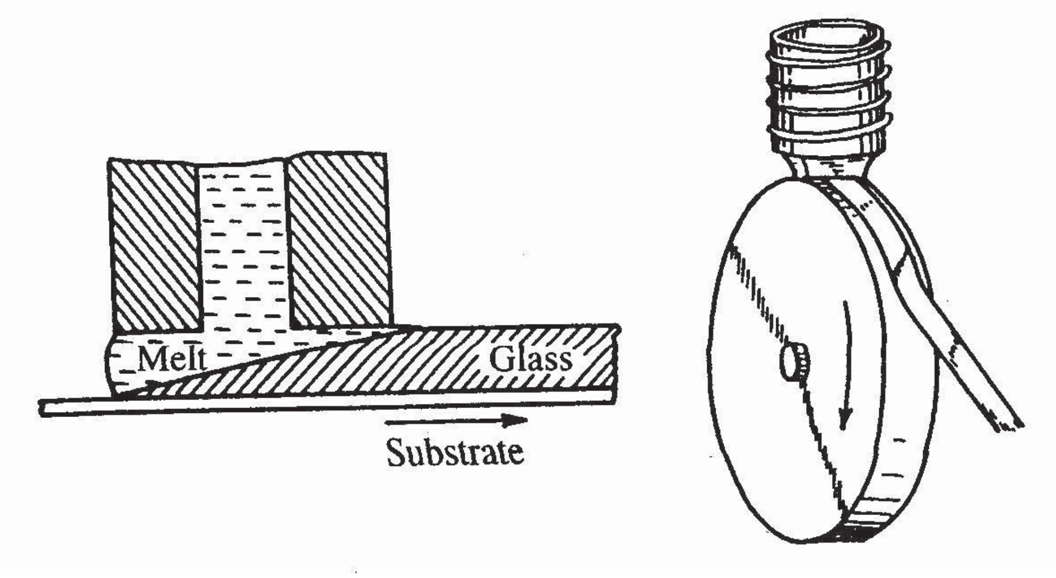

Fig. 2-6 A schematic diagram of the planar flow casting process [36].

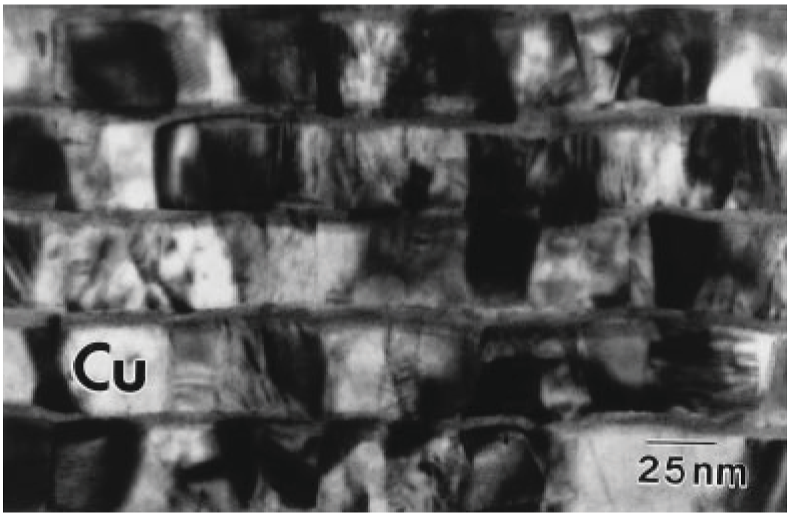

Fig. 2-7 TEM microstructure of a deposited Cu-Zr nanolaminate (38.8 nm Cu + 2.45 nm Zr). Between the Cu layers are amorphous Cu_4Zr_3 layers [43].

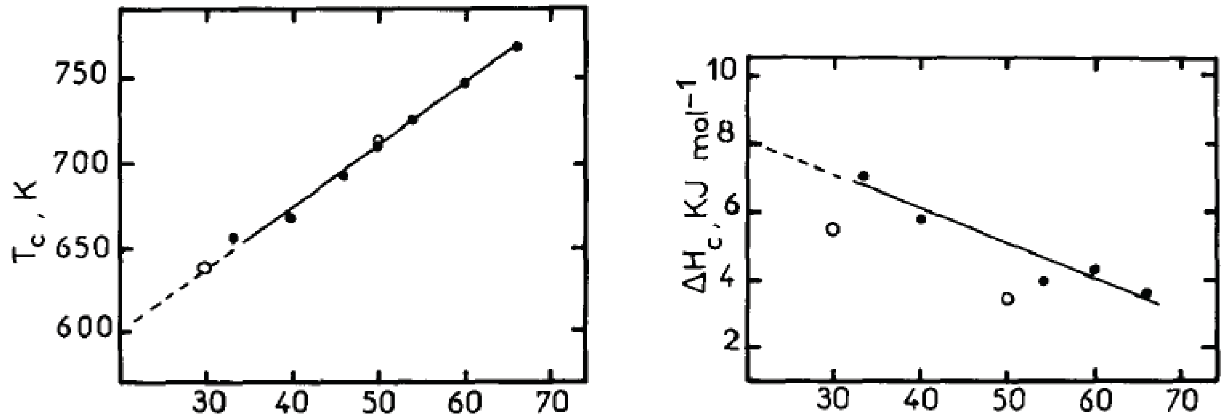

Fig. 2-8 (a) Crystallization temperatures for sputtered (○) and quenched (●) glassy Cu_xZr_{1-x} alloys as a function of the composition. (b) Crystallization enthalpies for sputtered (○) and quenched (●) glassy Cu_xZr_{1-x} alloys as a function of the composition [44].

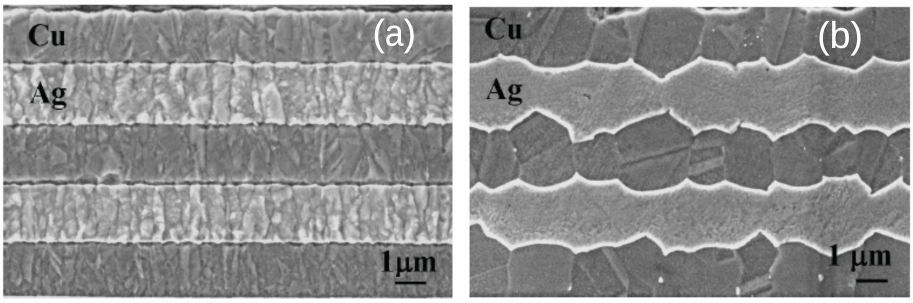

Fig. 2-9 Scanning electron micrograph of a cross section of an as-deposited Ag/Cu laminate, displaying relatively flat, well-defined interfaces, etched to reveal a columnar structure. Laminate growth was from bottom up. (b) Cross-section scanning electron micrograph of the laminate, annealed for 24 h at 900 K and etched to reveal Cu grain boundaries [52].

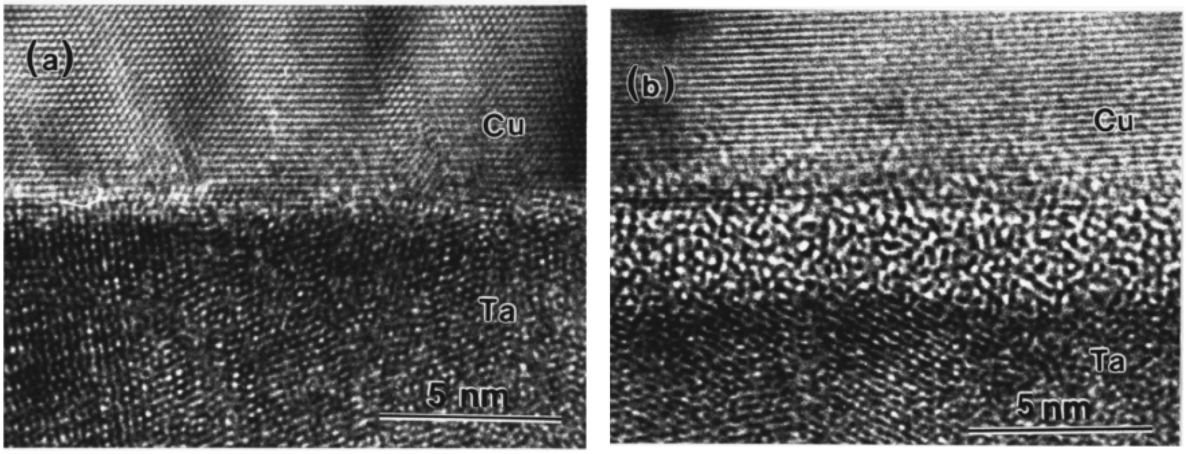

Fig. 2-10 High resolution election miscroscope images at the β-Ta/Cu interfaces of samples (a) as-deposited and (b) annealed at 400°C for 30 min [53].

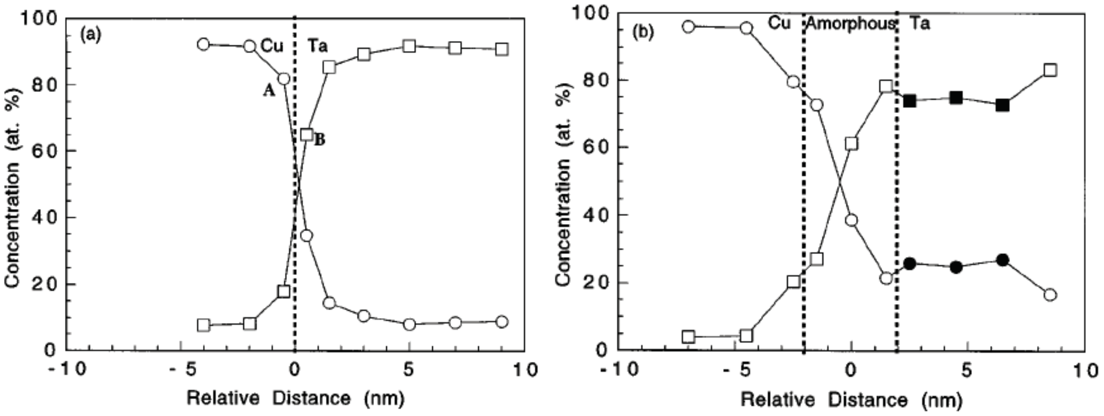

Fig. 2-11 EDS depth profiles across the interfaces of samples (a) as-deposited and (b) annealed at 400^{o}C for 30 min, respectively. The dashed lines annotated are the physical boundaries revealed in the HREM micrographs of Fig. 2-10 (a) and (b), respectively. Filled symbols in (b) denote the high content of Cu in Ta [53].

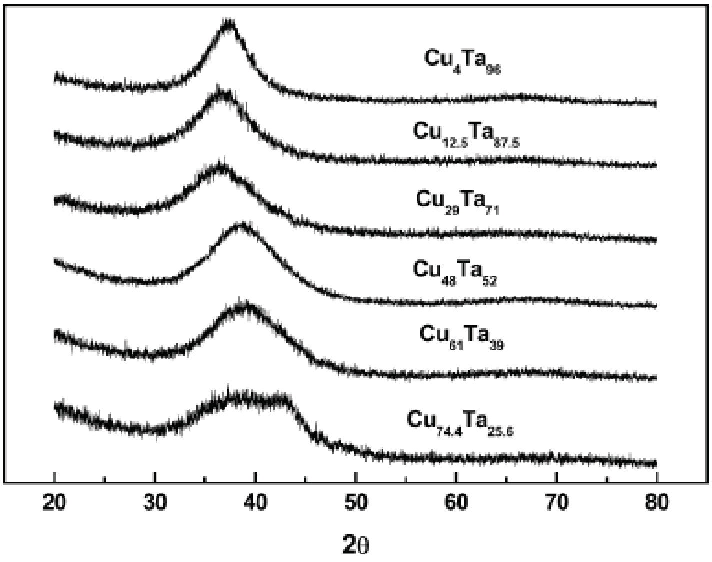

Fig. 2-12 X-ray diffraction patterns of the Cu-Ta alloy films [56].

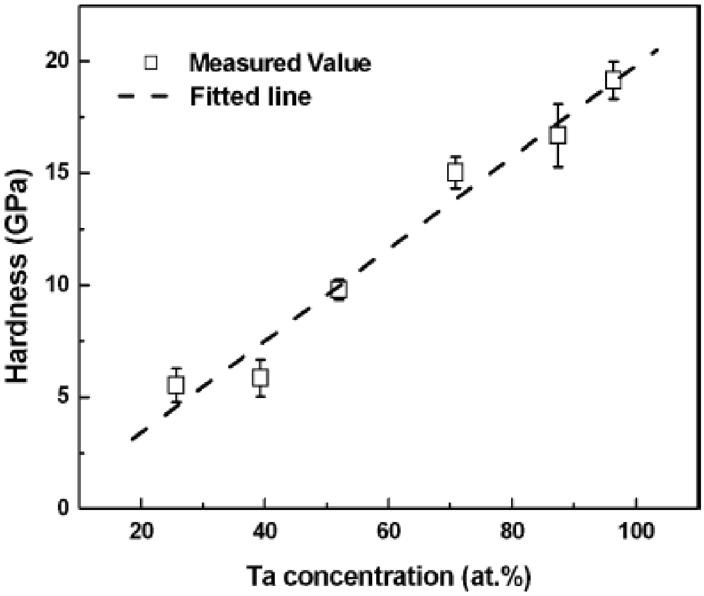

Fig. 2-13 Hardness variation with Ta concentration [56].

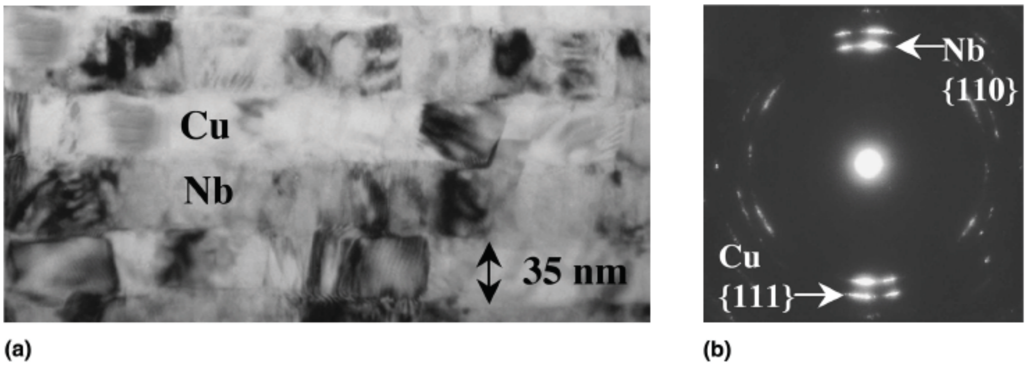

Fig. 2-14 (a) Bright-field TEM image showing the microstructure, in cross-section, of the as-deposited Cu-Nb 35 nm multilayers; (b) corresponding selected area diffraction pattern showing the {111}Cu//{110}Nb//interface plane texture [57].

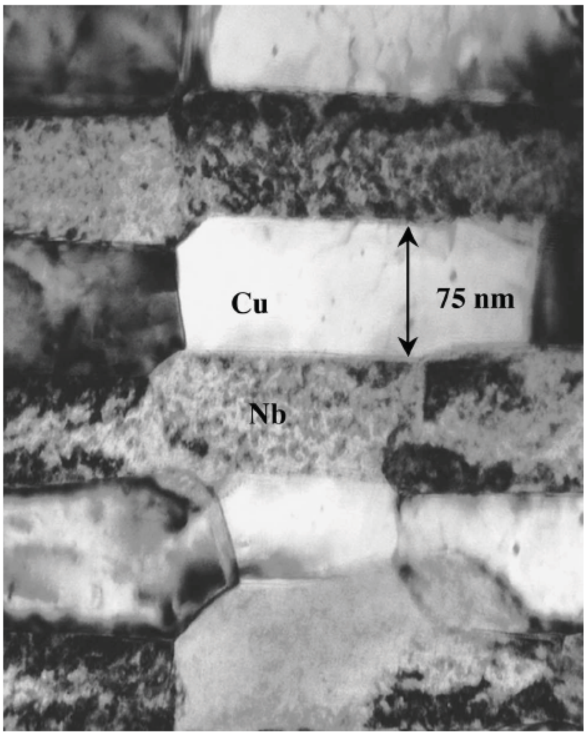

Fig. 2-15 Bright-field TEM micrograph showing the cross-sectional view of the microstructure of 75 nm Cu/Nb multilayer following 60 hours annealing at 700°C [57].

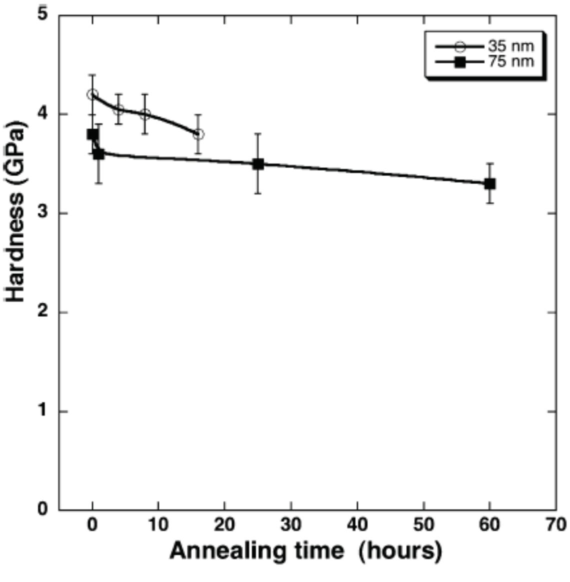

Fig. 2-16 Effect of annealing time at 700°C on the hardness of the 75 nm and 35 nm Cu/Nb multilayers [57].

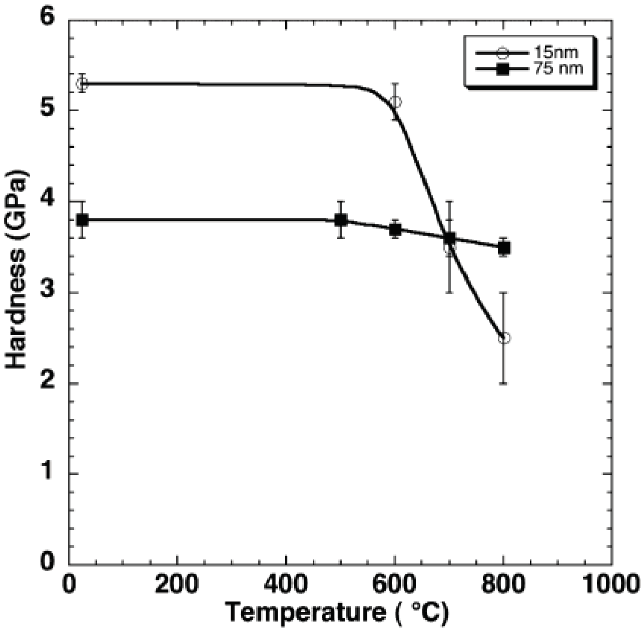

Fig. 2-17 Hardness of the 75 and 15 nm Cu/Nb multilayers following anneals for 30 minutes at the temperature shown [57].

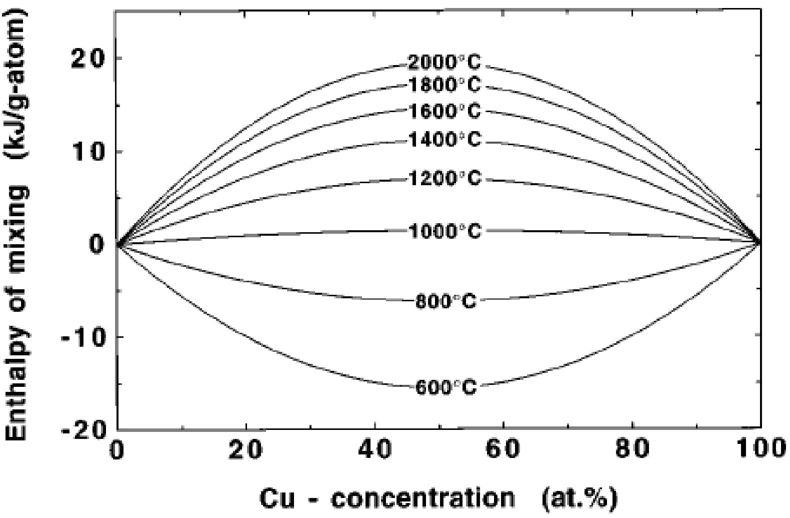

Fig. 2-18 Heats of mixing of the liquid/amorphous phase at various temperatures, calculated by the CALPHAD method. In the present CALPHAD approach, the heat of mixing is not temperature dependent below the assumed glass transition temperature of 627°C. Above this temperature, the heat of mixing increases with T^{-1} dependence [58].

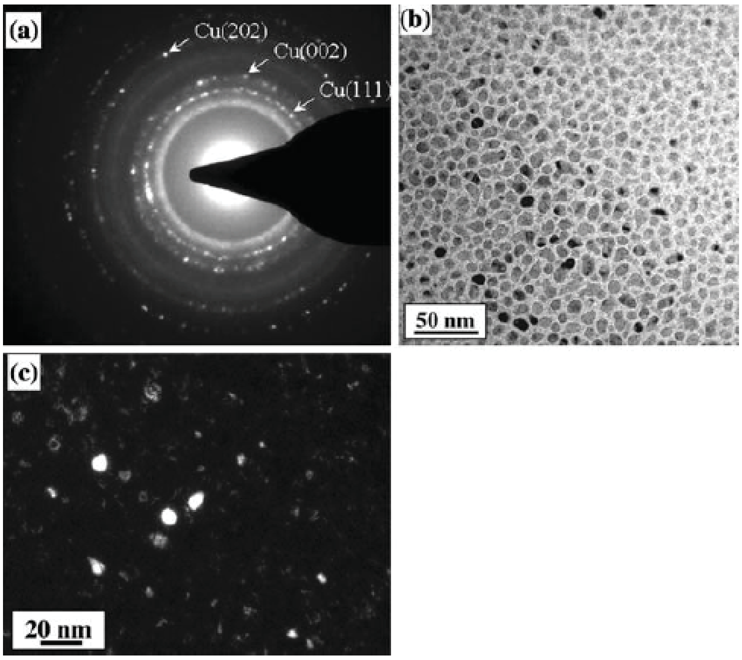

Fig. 2-19 (a) Selected area electron diffraction pattern from the Cu-45 at. pct Nb film after annealing at 200°C for 3 h. (b) Bright-field and (c) dark-field TEM images from the same film after annealing at 200°C for 3 h [59].

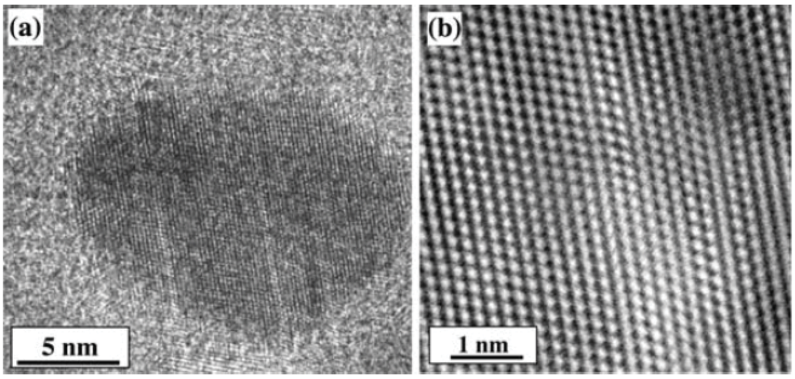

Fig. 2-20 (a) High-resolution TEM image of a single FCC nanocrystal, viewed along the [011] direction and exhibiting twin defects, embedded in the amorphous matrix of the Cu-45 at. pct Nb annealed film. (b) A higher-magnification image of the high-resolution TEM micrograph shown in (a), exhibiting the detailed atomic structure of the nanocrystal and one of the twin defects [59].

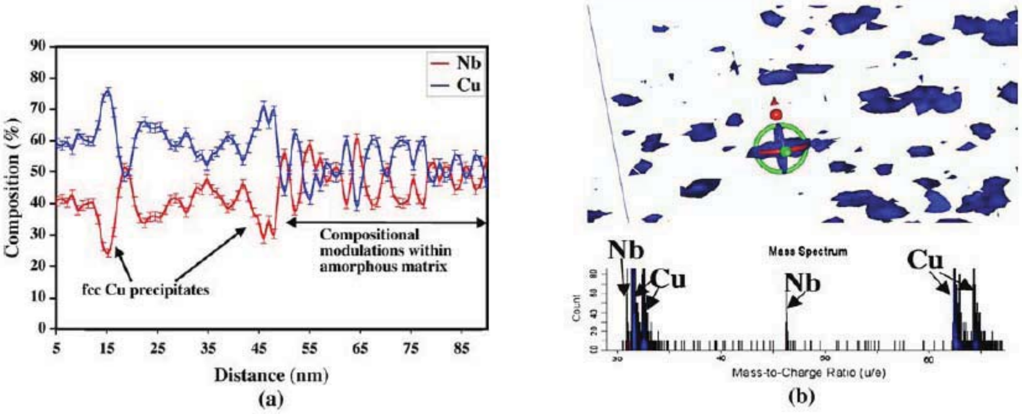

Fig. 2-21 (a) Compositional profile corresponding to the 3DAP reconstructions. This profile is averaged over a cylinder of diameter 4 nm passing through the center of the reconstruction along its axis. (b) Section of the 3DAP reconstruction showing Cu-rich regions (isosurface > 80 at. pct Cu in blue). The mass spectrum shown subsequently in (b) corresponds to the specific FCC Cu nanoprecipitate marked (the circle) in the figure [59].

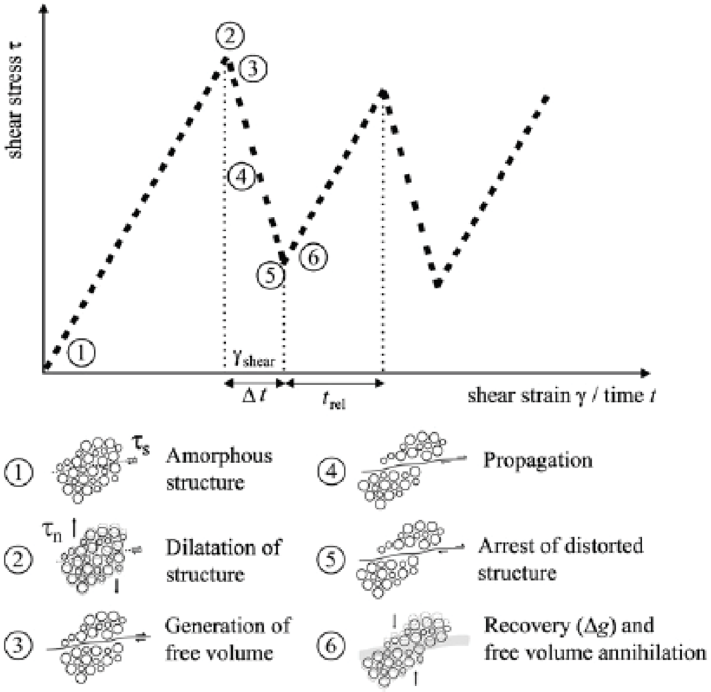

Fig. 2-22 Schematic illustration showing the proposed model for serrated flow in bulk metallic glasses [65].

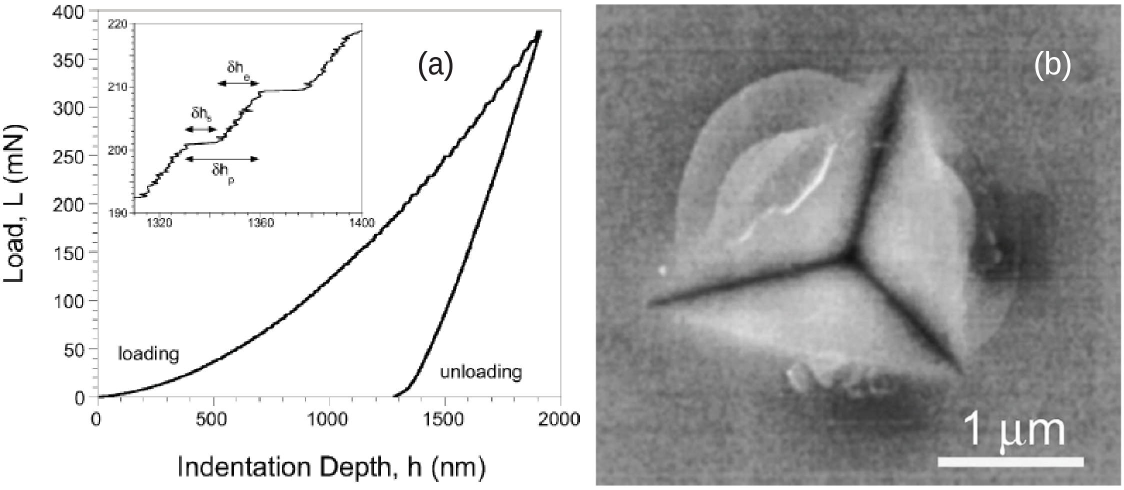

Fig. 2-23 Loading and unloading curves for the bulk glass $Pd_{40}Cu_{30}Ni_{10}P_{20}$ (at.%). The loading rate is 0.5 mNs^{-1}. The close-up of the loading curve shows the definition of the depth increments. (b) SEM micrograph of an indent in a fully amorphous $Ni_{79}Ta_{14}C_7$ thin film [71].

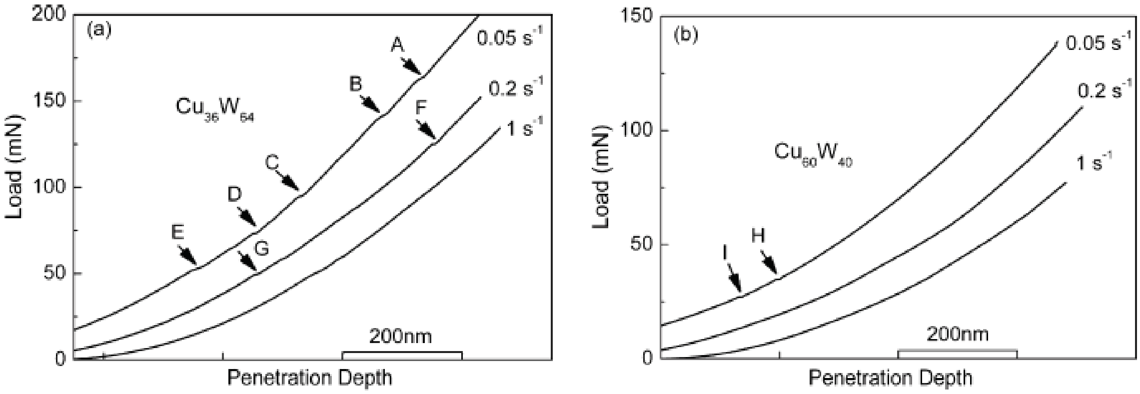

Fig. 2-24 Typical load–displacement (P–h) curves during nanoindentations at various strain rate (0.05 s^{-1}, 0.2 s^{-1}, and1 s^{-1}) for (a) $Cu_{36}W_{64}$ and (b) $Cu_{60}W_{40}$. Only the loading portions are shown and the curves are shifted [74].

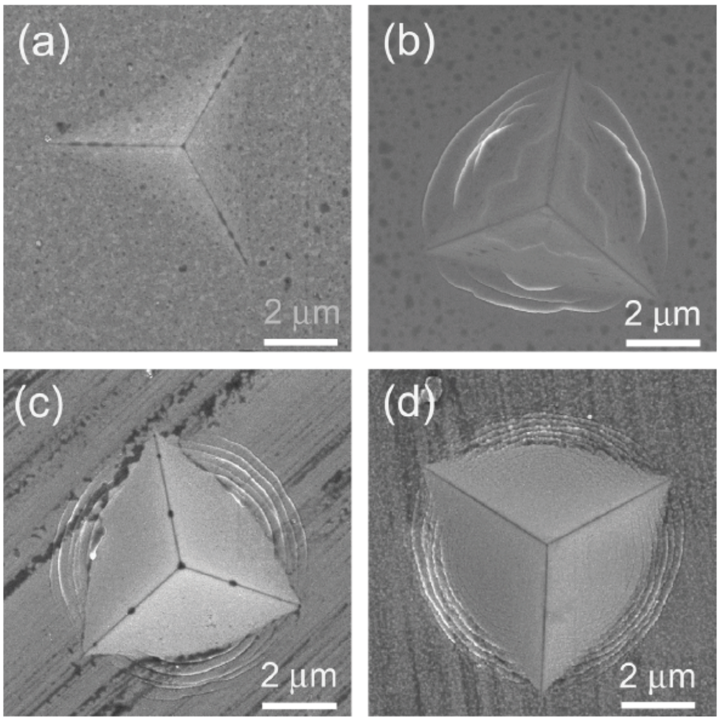

Fig. 2-25 SEM micrographs of the indents of (a) $Cu_{21}W_{79}$, (b) $Cu_{36}W_{64}$, (c) $Cu_{60}W_{40}$ and (d) $Cu_{71}W_{29}$ alloy films. The strain rate adopted is 0.05 s^{-1} [74].

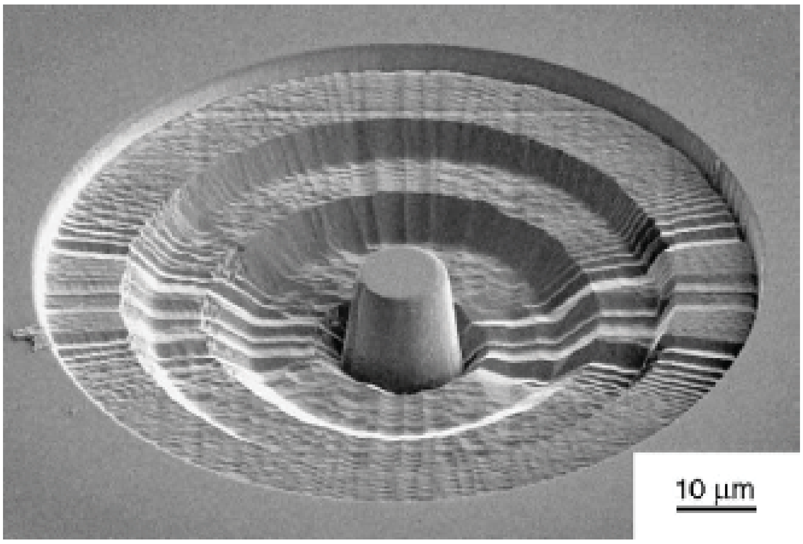

Fig. 2-26 Annular milling patterns have been used to FIB mill a roughly defined microcompression sample and surrounding cavity. The pillar in the center of the cavity will be further micro-machined to form a microcompression sample that is 5 μm in diameter and 12 μm in length. The bulk sample is a (269) oriented Ni single crystal, and the annular milling pattern was machined for 240 min using a 5 nA beam [75,76].

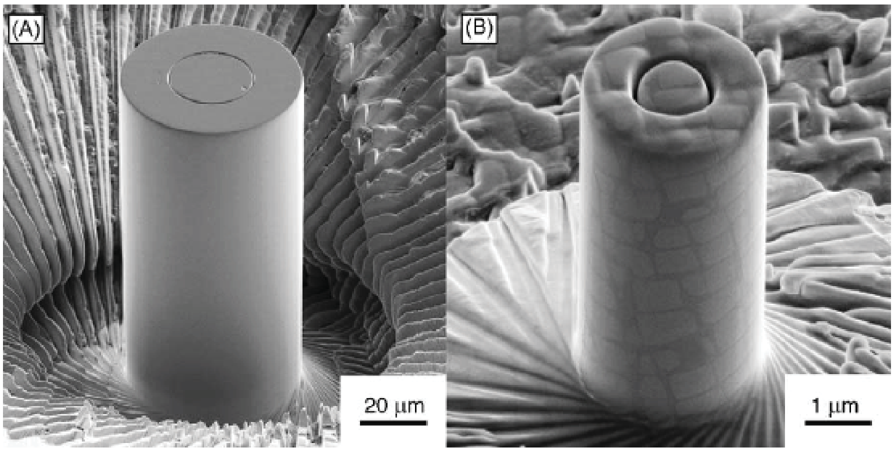

Fig. 2-27 (A) A 43 μm diameter microcompression sample machined into a $Ni_3(Al, Hf)$ single crystal, where the gage length of this sample is approximately 90 μm. The circular pattern on the top surface of the sample is a fiducial mark used as part of an automated machining program for the FIB. (B) A 2.3 μm diameter microcompression sample machined into a single-crystal Ni superalloy (UM-F19). The gage length of this micro-sample is approximately 4.6 μm. One can clearly observe the Ni_3Al precipitates on the surface of the micro-sample [75].

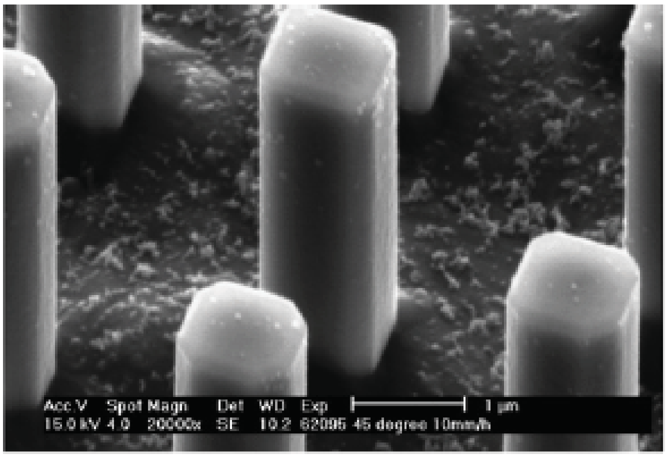

Fig. 2-28 Molybdenum alloy micropillars fabricated by selective etching of the matrix in a NiAl-Mo directionally solidified eutectic: as-fabricated pillars with a nominal edge dimension of 1 μm [77].

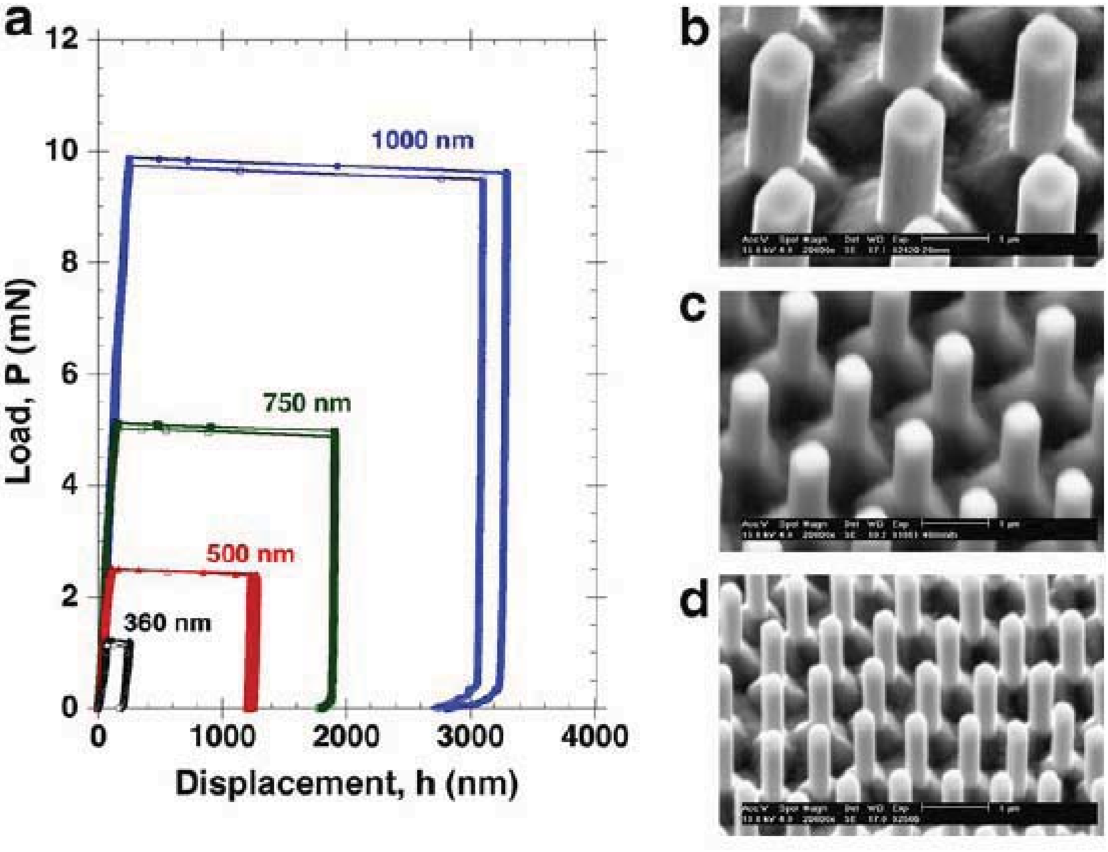

Fig. 2-29 Microcompression tests of molybdenum alloy pillars with sizes in the range 360-1000 nm: (a) compressive load–displacement curves; SEM images of micropillars with nominal edge dimensions of (b) 750 nm, (c) 500 nm and (d) 360 nm [77].

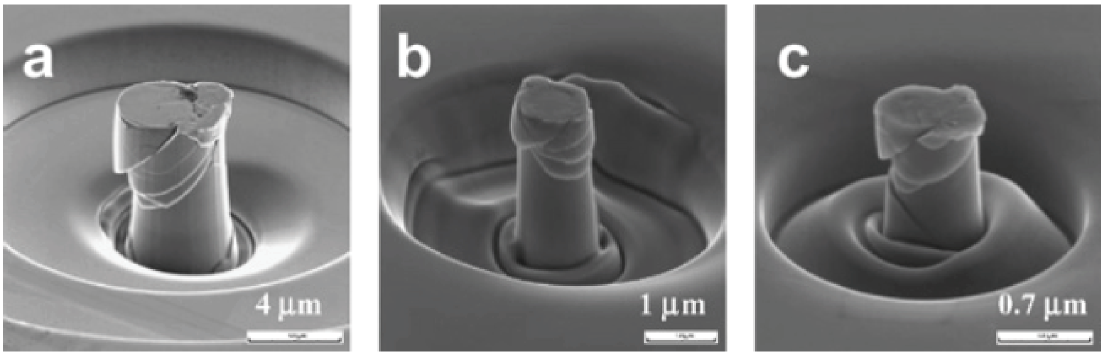

Fig. 2-30 SEM micrographs showing the appearance of deformed pillars at a strain rate $1x10^{-4}$ s^{-1}: (a) 3.8 μm, (b) 1 μm, and (c) 700 nm [85].

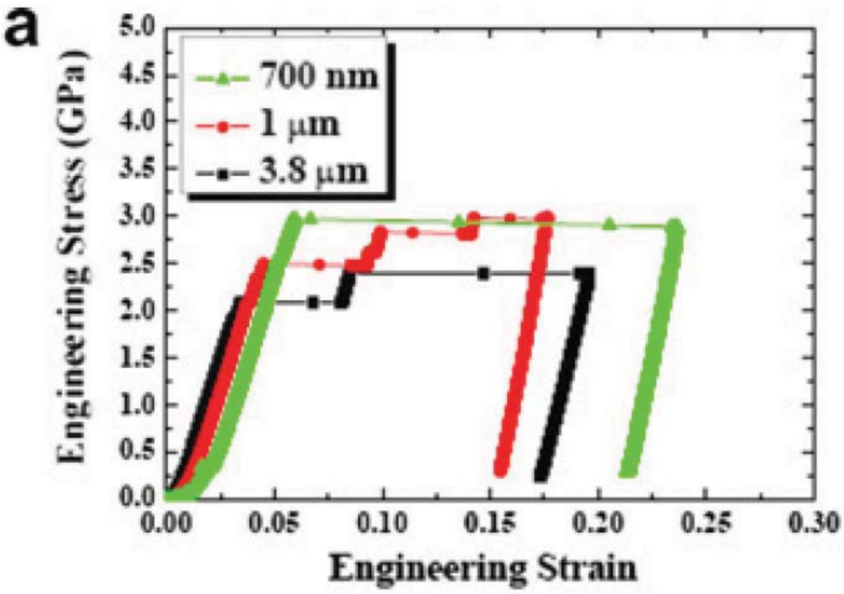

Fig. 2-31 The microcompression engineering stress–strain curves of the 3.8 μm, 1 μm and 700 nm micropillars at different strain rates of 1 x 10^{-4} s^{-1} [85].

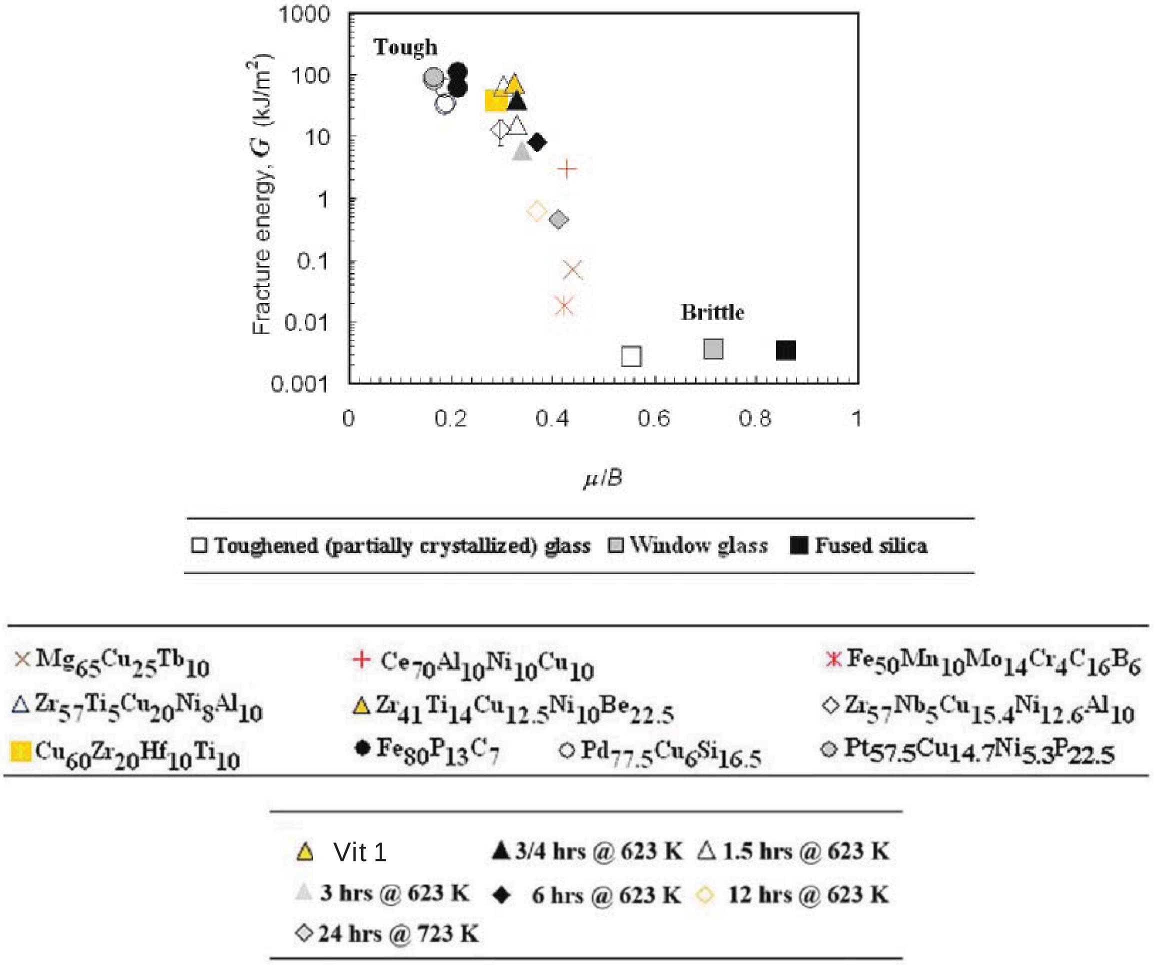

Fig. 2-32 The correlation of fracture energy G with ratio μ/B for all the collected data on metallic glasses, as well as for oxide glasses. The divide between the tough and brittle regimes is in the range $(\mu/B)_{crit}$ =0.41-0.43 [86].

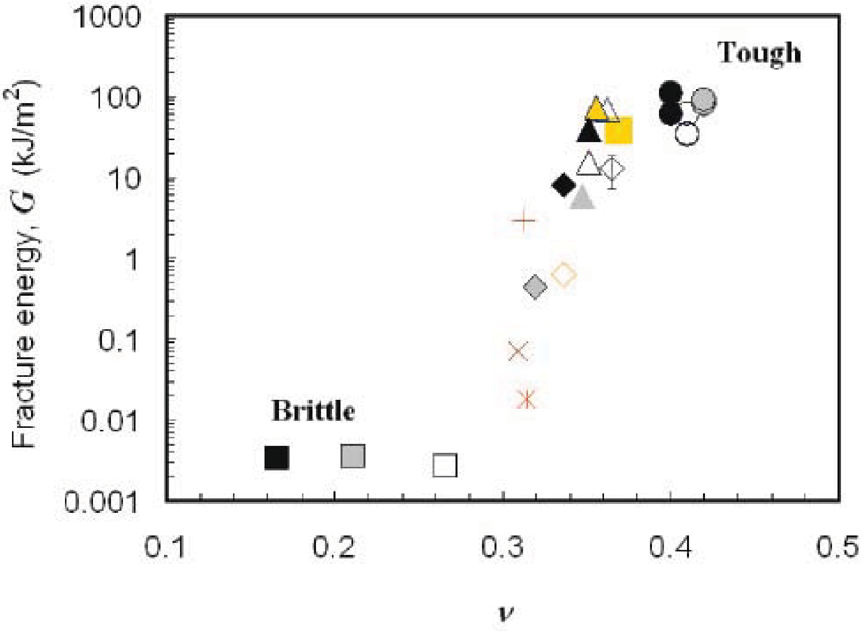

Fig. 2-33 The correlation of fracture energy G with Poisson's ratio ν for all the collected data on metallic glasses as well as for oxide glasses (the symbols are the same as Fig. 2-35). The divide between the tough and brittle regimes is in the range ν_{crit} = 0.31-0.32 [86].

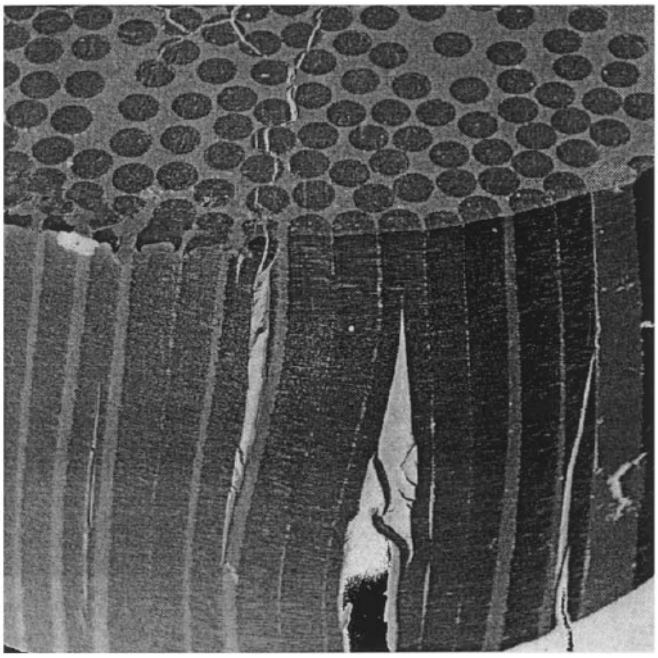

Fig. 2-34 Compressive failure of 60 V_f%-tungsten/$Zr_{41.25}Ti_{13.75}Cu_{12.5}Ni_{10}Be_{22.5}$ composite. Note that at the top cracks run from fiber to fiber, and longitudinal splitting and buckling occur in fibers [87].

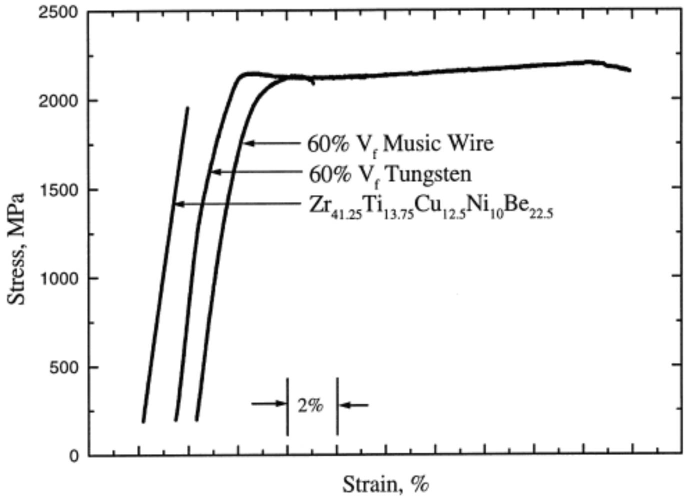

Fig. 2-35 Comparison of 40 V_f%-tungsten and steel reinforced metallic glass matrix composite compressive stress-strain properties. Ultimate strength is the same, and is not significantly different from the unreinforced $Zr_{41.25}Ti_{13.75}Cu_{12.5}Ni_{10}Be_{22.5}$ [87].

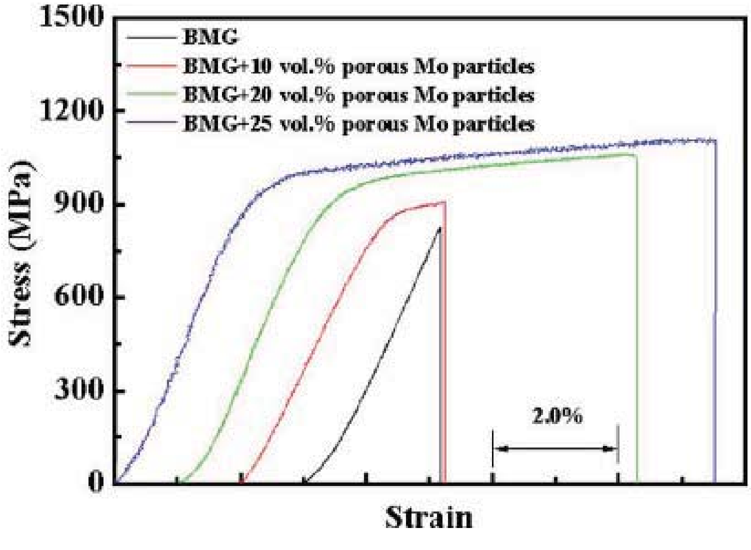

Fig. 2-36 Representative room-temperature compressive engineering stress-strain curves for the as-cast 2 mm diameter compression specimens. The curves are shifted relative to each other for clarity [88].

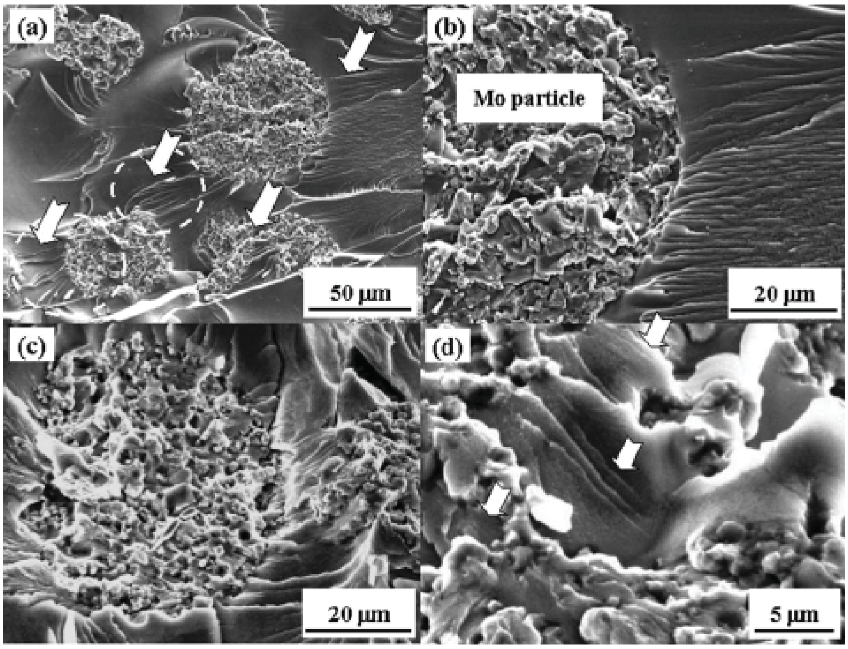

Fig. 2-37 Observations on the fracture surface. (a) and (b) SEM backscattered electron images showing the initiating and halting of microcrack traces on the interfaces of Mo particle/amorphous matrix. (c) and (d) The deformation and fracture behavior inside the porous Mo particles [88].

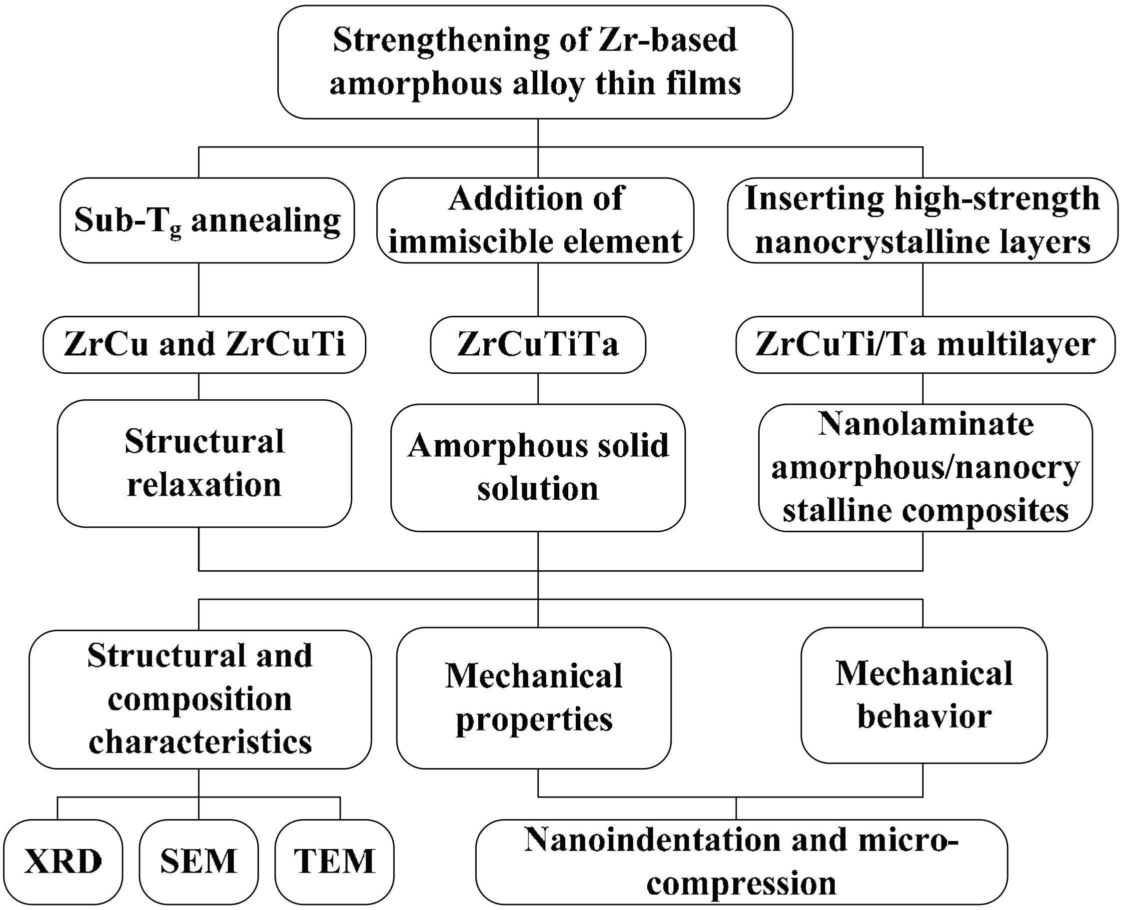

Fig. 3-1 Flow chart of the experiment procedures.

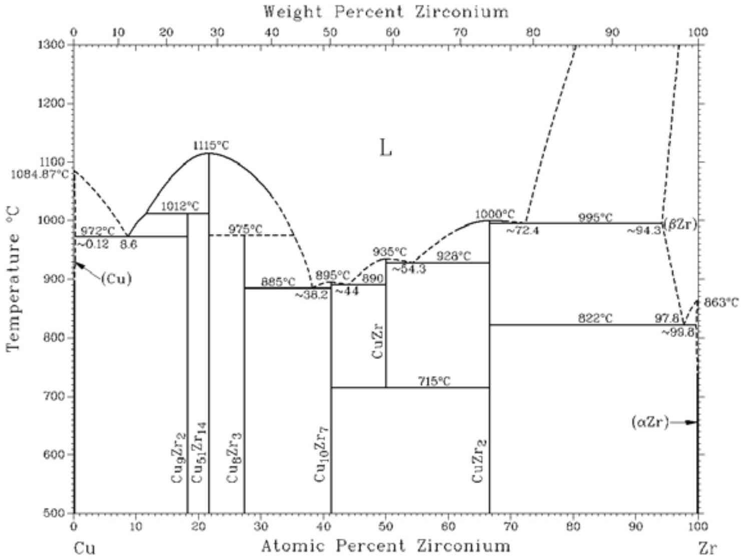

Fig. 3-2 Binary phase diagrams of Zr-Cu.

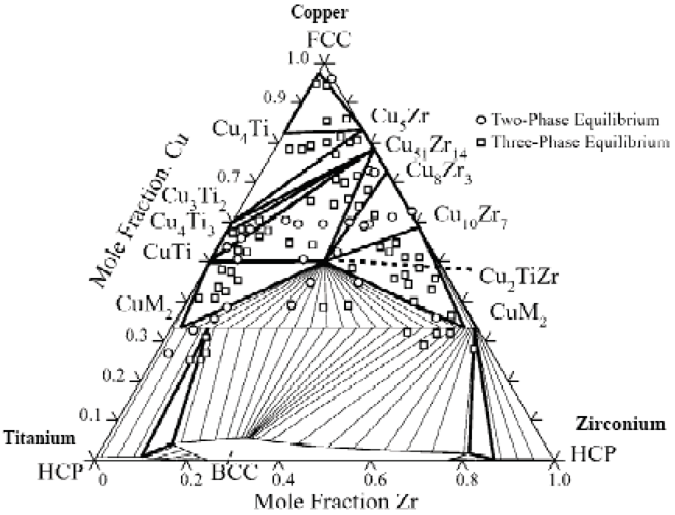

Fig. 3-3 Calculated versus experimental ternary isothermal section for the Cu-Ti-Zr system at 703°C [91].

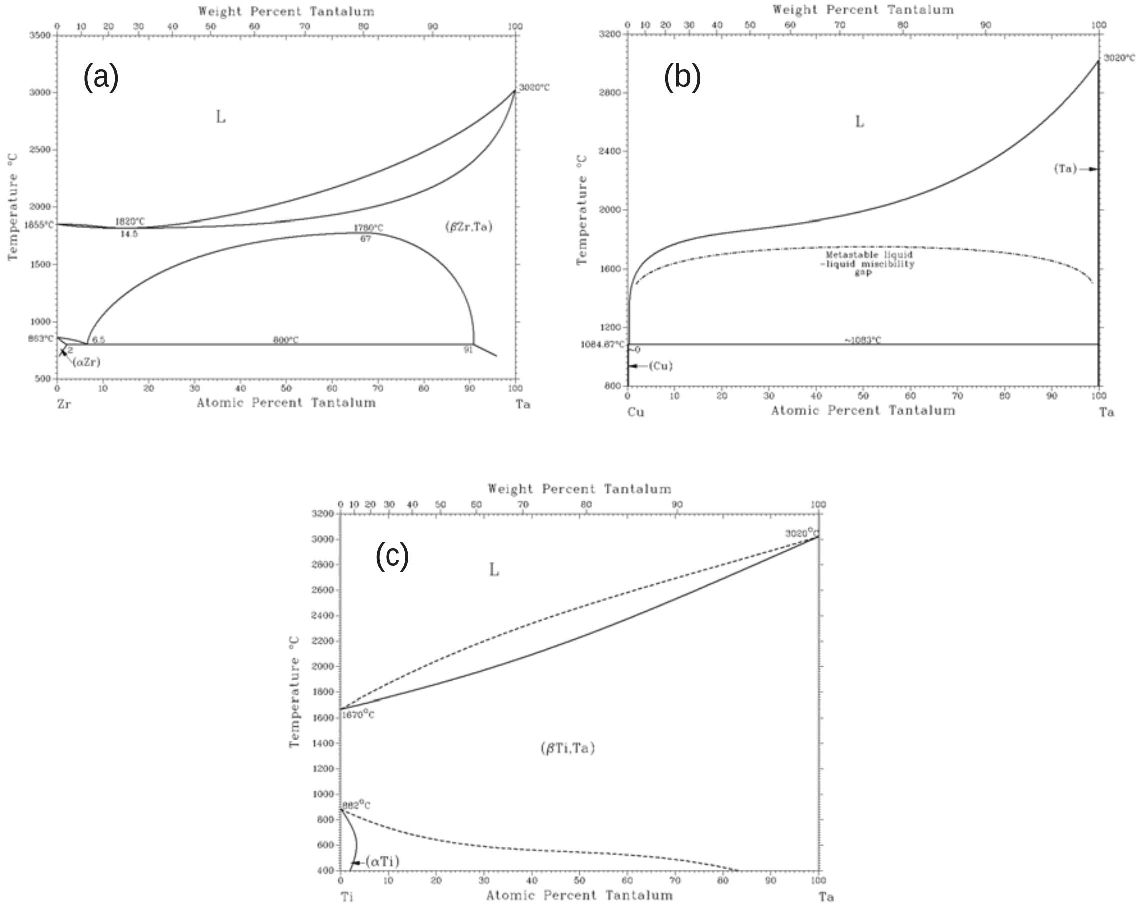

Fig. 3-4 Binary phase diagrams of (a) Zr-Ta, (b) Cu-Ta, and (c) Ti-Ta.

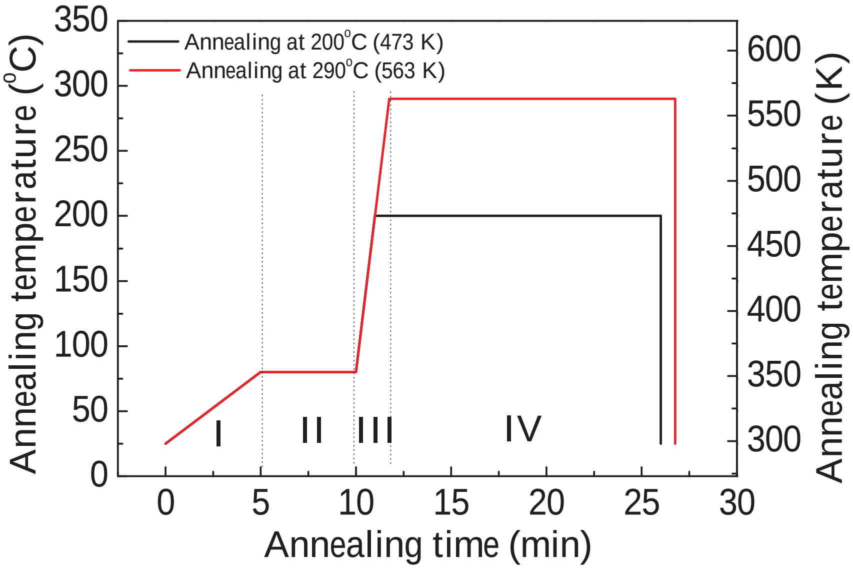

Fig. 3-5 Temperature paths of the post heat-treatment.

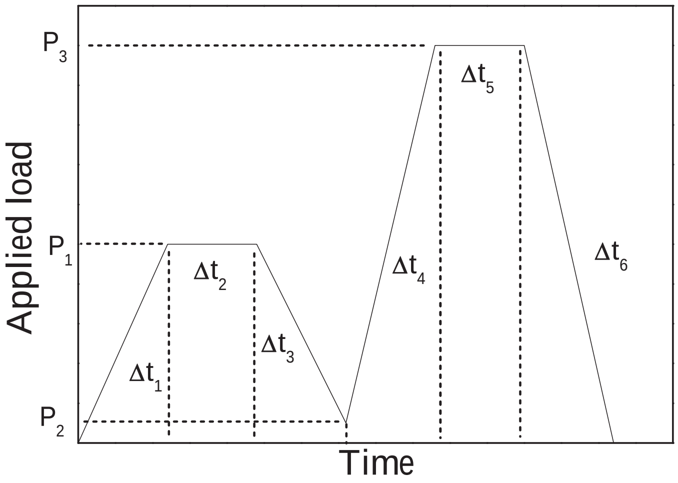

Fig. 3-6 Load function of the microcompression test.

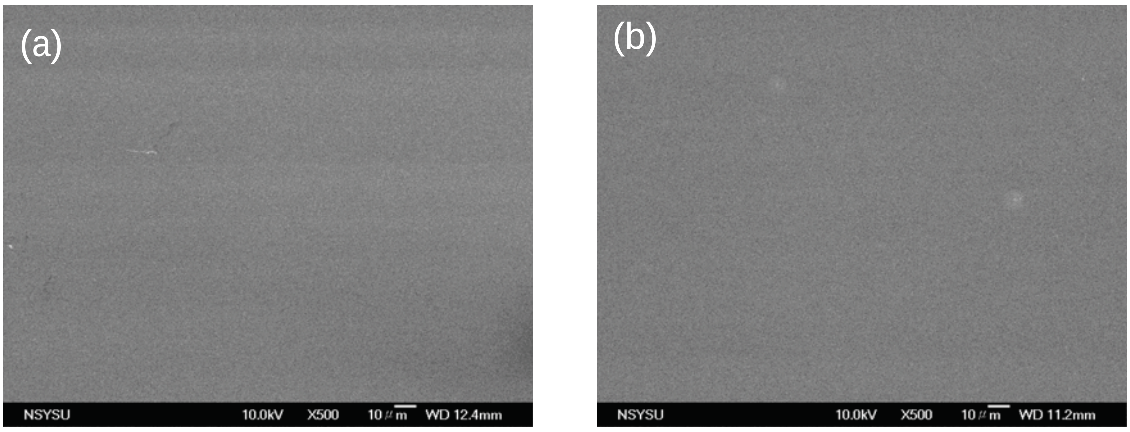

Fig. 4-1 SEI images of the as-deposited (a) ZrCu and (b) ZrCuTi thin film metallic glasses.

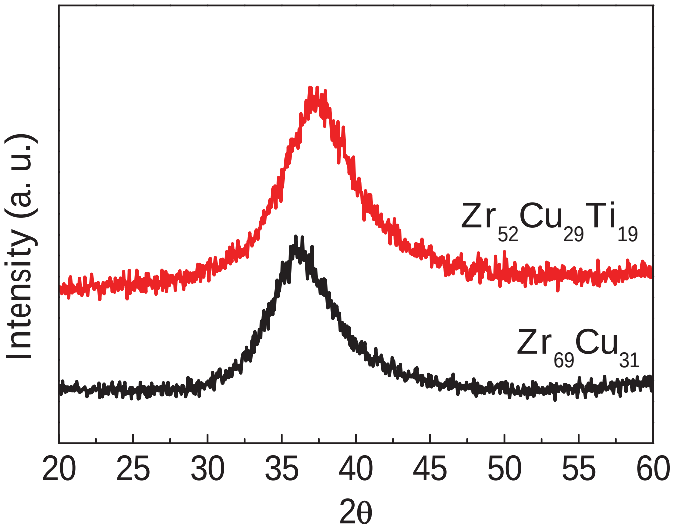

Fig. 4-2 XRD patterns of $Zr_{69}Cu_{31}$ and $Zr_{52}Cu_{29}Ti_{19}$ thin films.

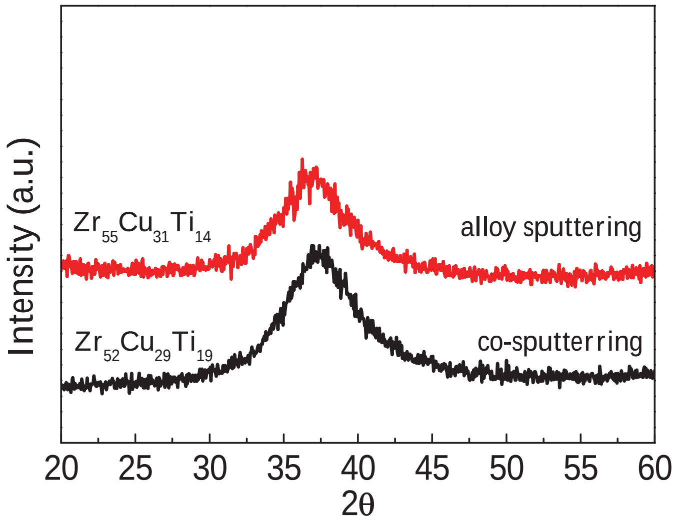

Fig. 4-3 XRD patterns of $Zr_{52}Cu_{29}Ti_{19}$ and $Zr_{55}Cu_{31}Ti_{14}$ thin films.

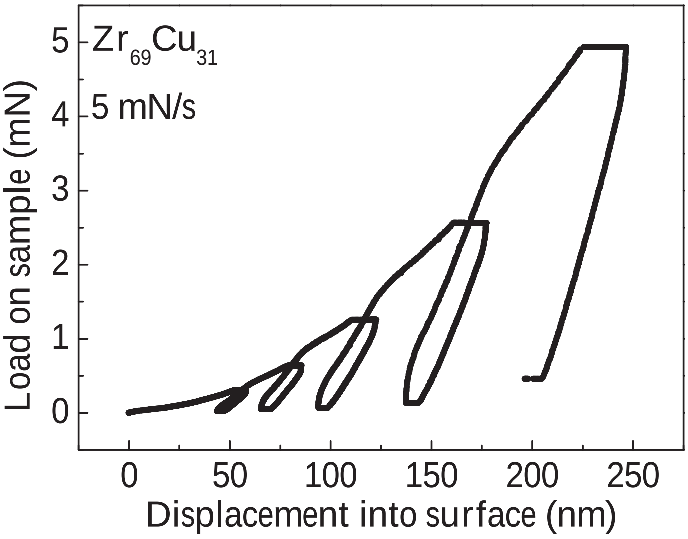

Fig. 4-4 The displacement-load curves of $Zr_{69}Cu_{31}$ thin film metallic glass with five loading cycles at 5 mN/s.

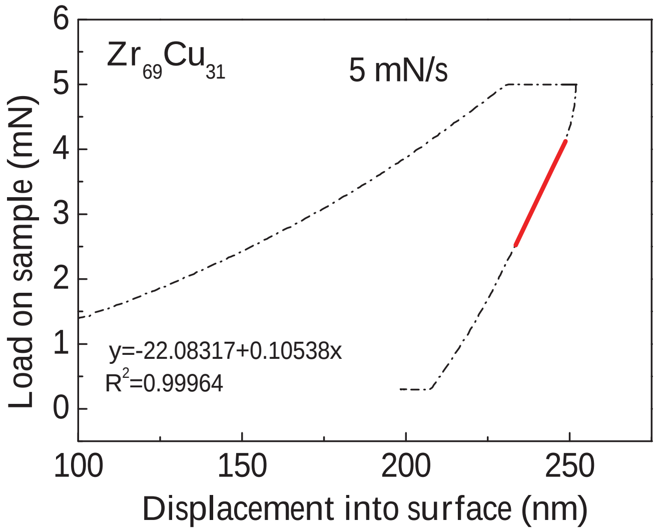

Fig. 4-5 The stiffness of $Zr_{69}Cu_{31}$ using the fitting for the linear part of the unloading curve.

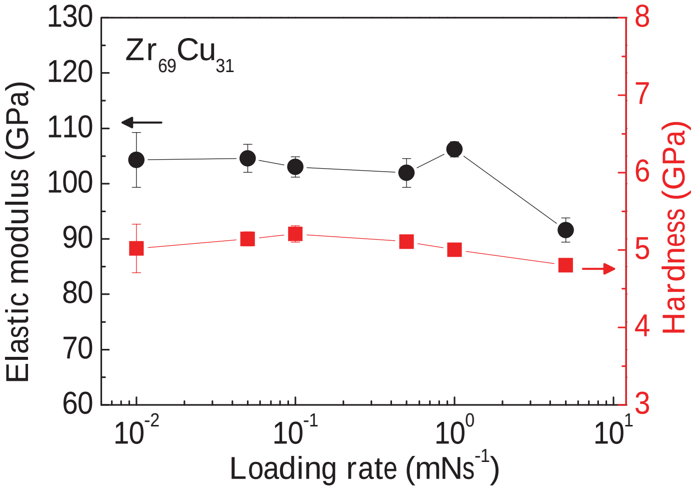

Fig. 4-6 Mechanical properties of the $Zr_{69}Cu_{31}$ thin film metallic glass at different loading rates from 0.01 to 5 mNs^{-1}.

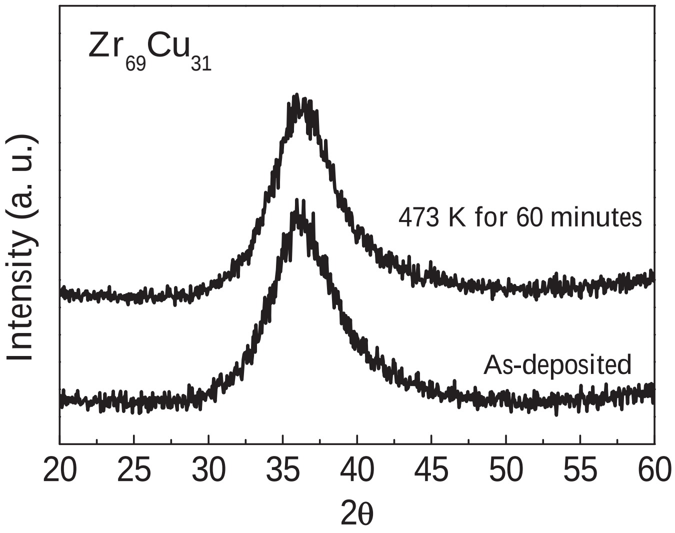

Fig. 4-7 XRD patterns of the $Zr_{69}Cu_{31}$ co-sputtered thin film metallic glasses under the as-deposited and after annealing at 473 K for 60 minutes.

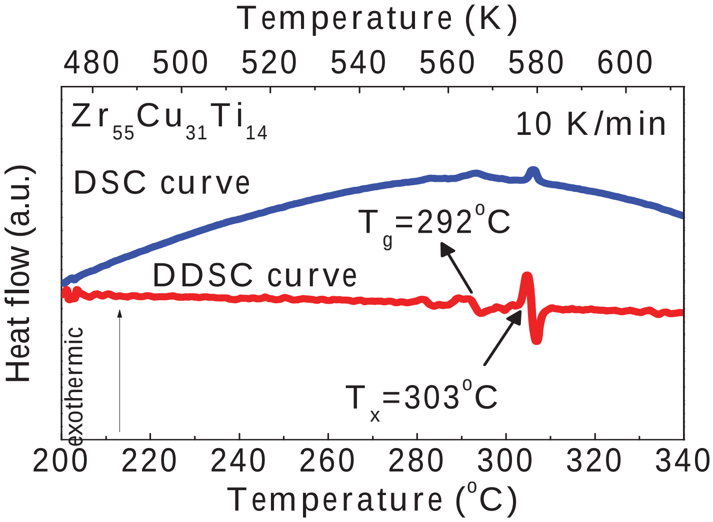

Fig. 4-8 DSC scan of the $Zr_{55}Cu_{31}Ti_{14}$ TFMGs.

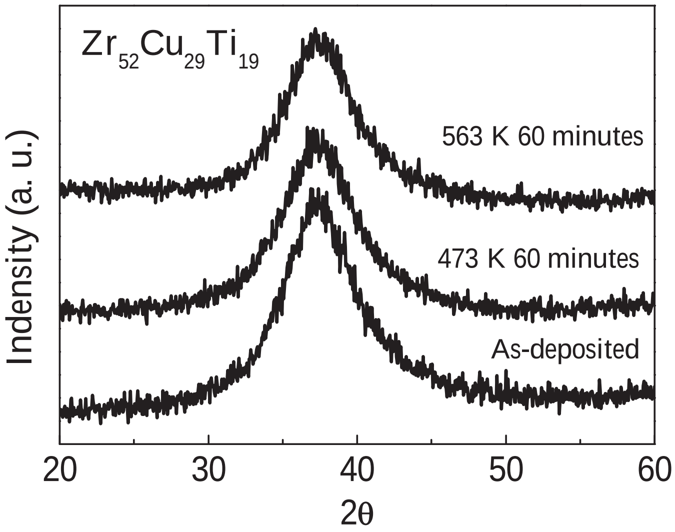

Fig. 4-9 XRD patterns of the co-sputtered ZrCuTi thin film metallic glasses undet the as-posited and after annealing at 473 K and 563 K, respectively.

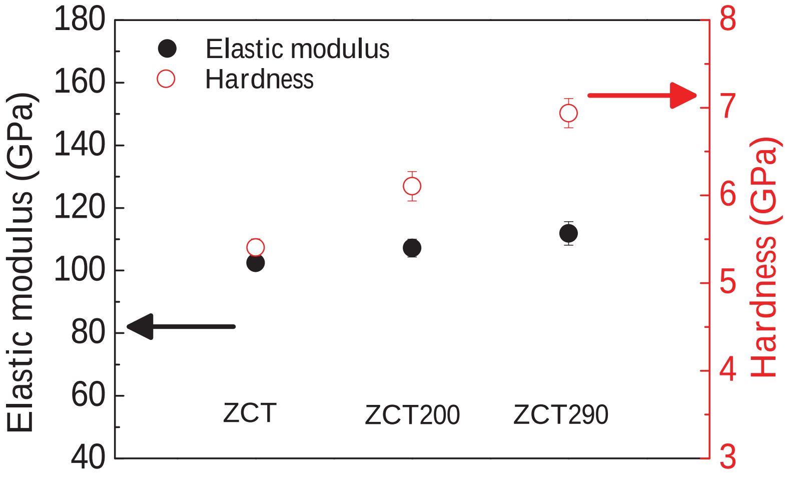

Fig. 4-10 Evolution of the elastic modulus and hardness of as-deposited and annealed $Zr_{59}Cu_{29}Ti_{19}$ TFMGs. The test rate is 0.05 mNs^{-1}.

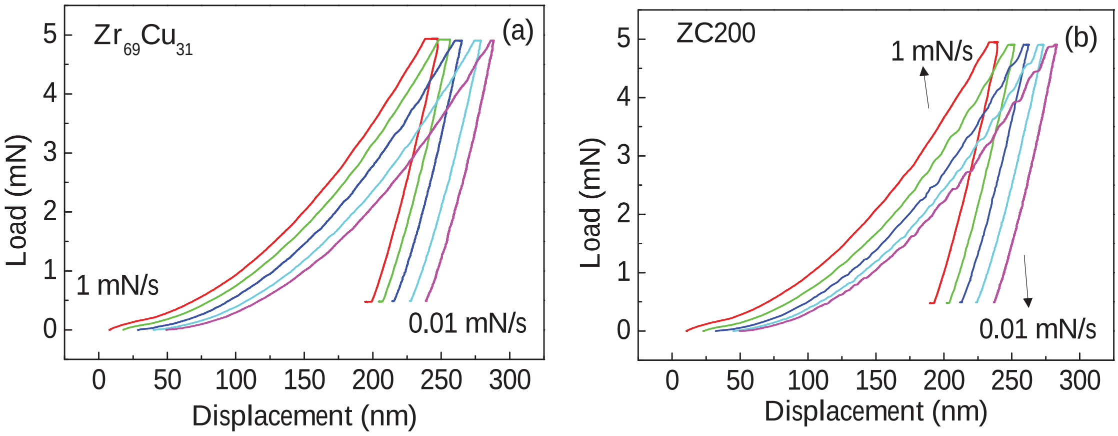

Fig. 4-11 The displacement-load curves of (a) the $Zr_{69}Cu_{31}$ (ZC) thin film metallic glass and (b) $Zr_{69}Cu_{31}$ (ZC200) thin film metallic glass annealed at 473 K for 60 minutes with different loading rates from 0.01 to 1 mN/s.

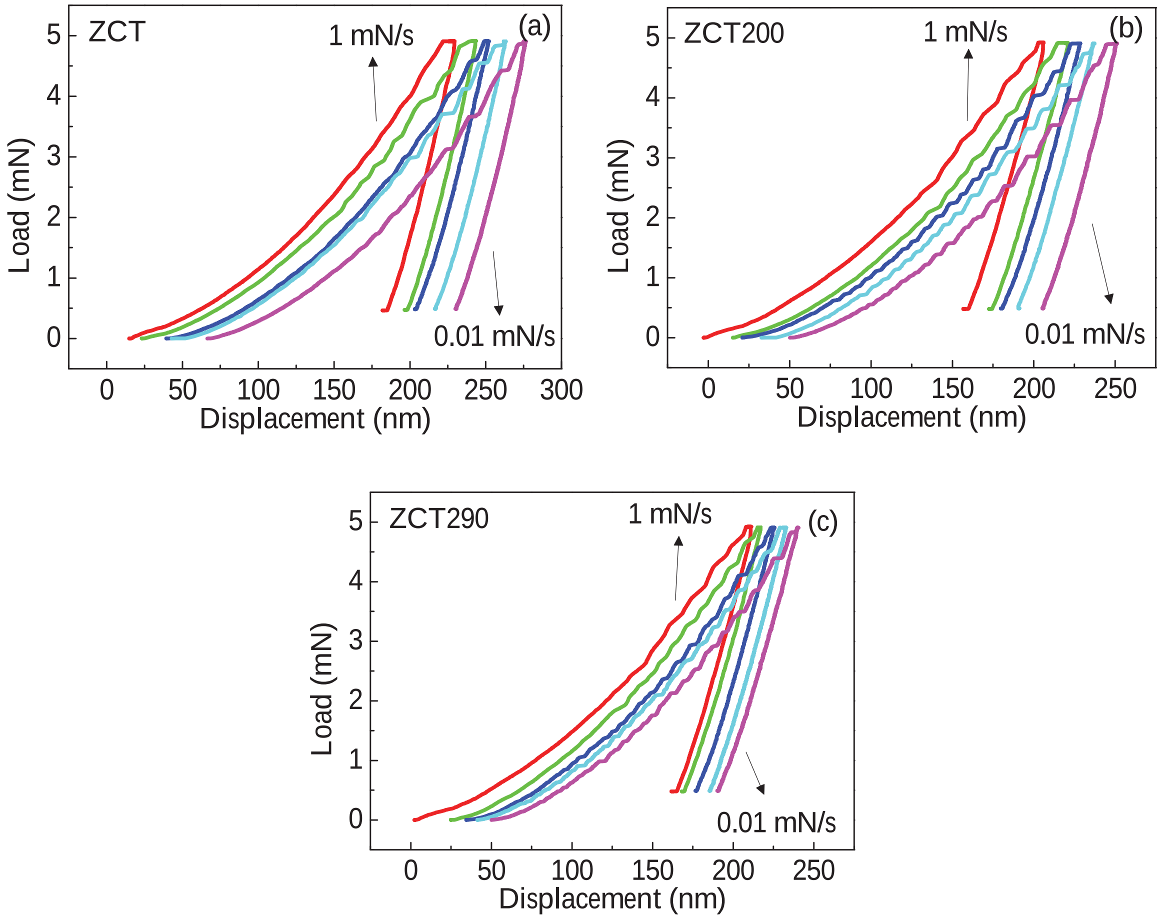

Fig. 4-12 The P-h curves of (a) ZCT, (b) ZCT200, and (c) ZCT290 specimens at different loading rates from 0.01 to 1 mN/s.

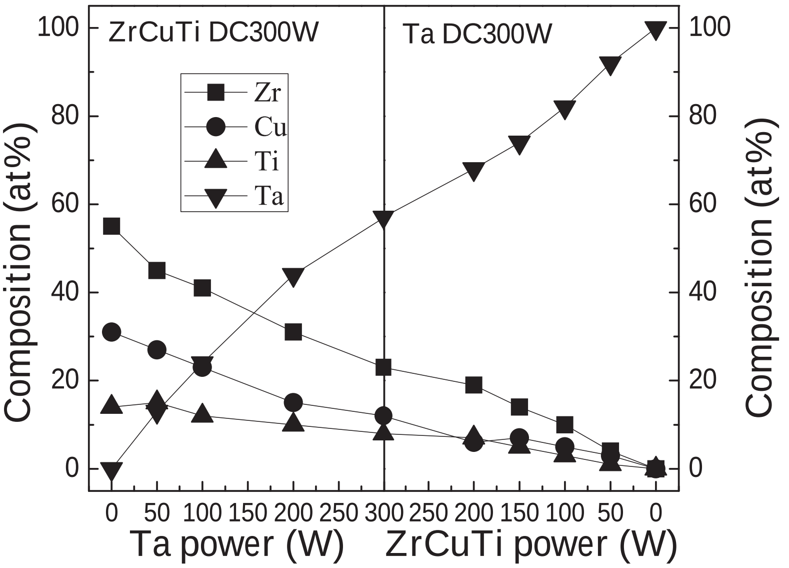

Fig. 4-13 Composition variation of the ZrCuTiTa TFMGs.

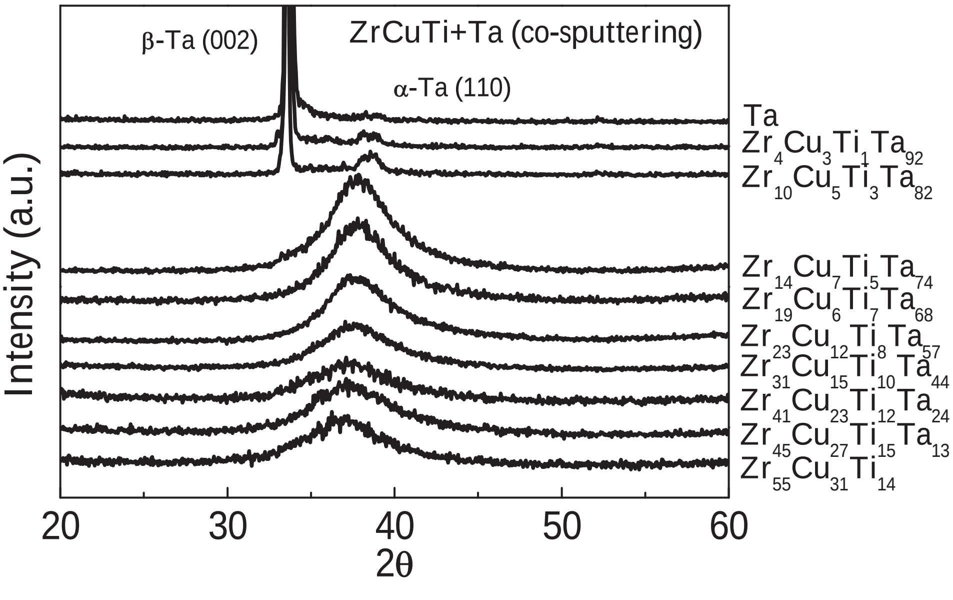

Fig. 4-14 XRD diffraction patterns of the ZrCuTiTa alloy thin films.

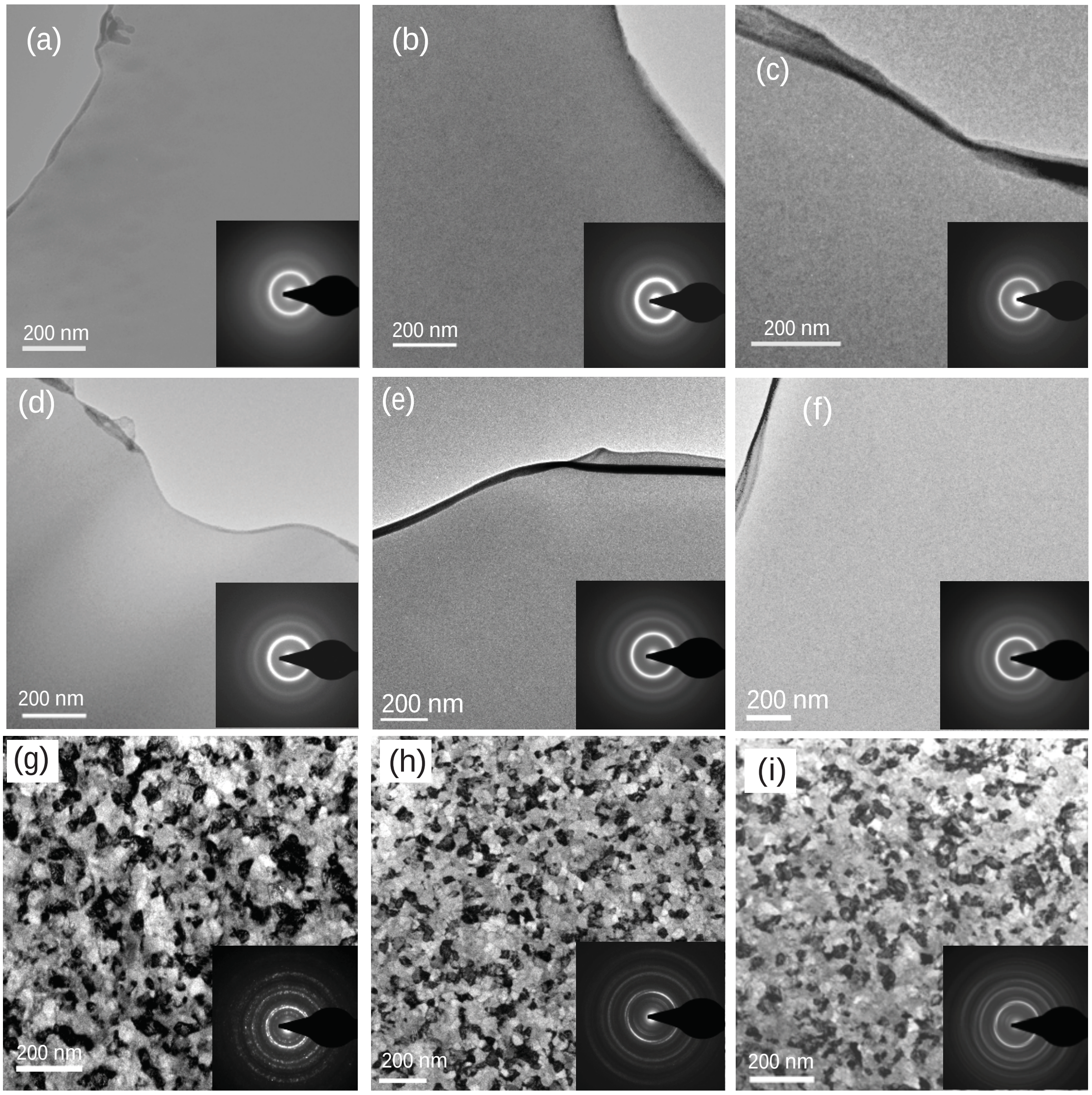

Fig. 4-15 Bright-field TEM images of (a) $Zr_{45}Cu_{27}Ti_{15}Ta_{13}$, (b) $Zr_{41}Cu_{23}Ti_{12}Ta_{24}$, (c) $Zr_{31}Cu_{15}Ti_{10}Ta_{44}$, (d) $Zr_{23}Cu_{12}Ti_8Ta_{57}$, (e) $Zr_{19}Cu_6Ti_7Ta_{68}$, (f) $Zr_{14}Cu_7Ti_5Ta_{74}$, (g) $Zr_9Cu_5Ti_3Ta_{83}$, (h) $Zr_4Cu_3Ti_1Ta_{92}$, and (i) nanocrystalline pure Ta (with inserted selected area diffraction patterns).

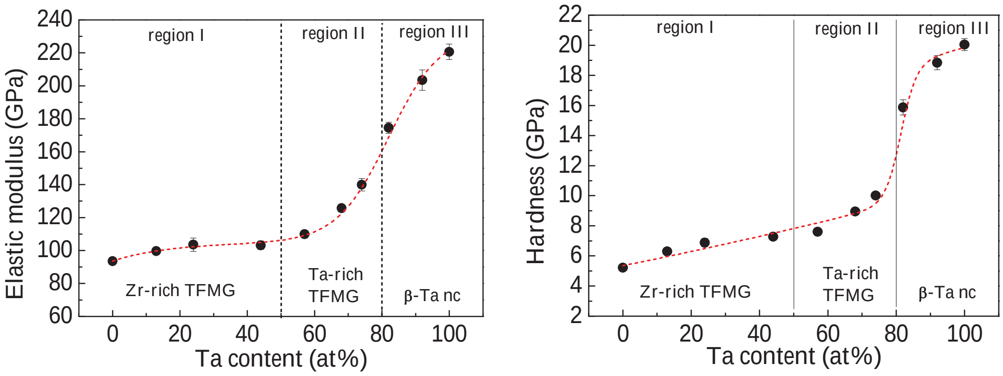

Fig. 4-16 Relationship between (a) elastic modulus and (b) hardness of ZrCuTiTa alloy thin films and Ta content. The experimental values of elastic modulus and hardness are measured by nanoindentation.

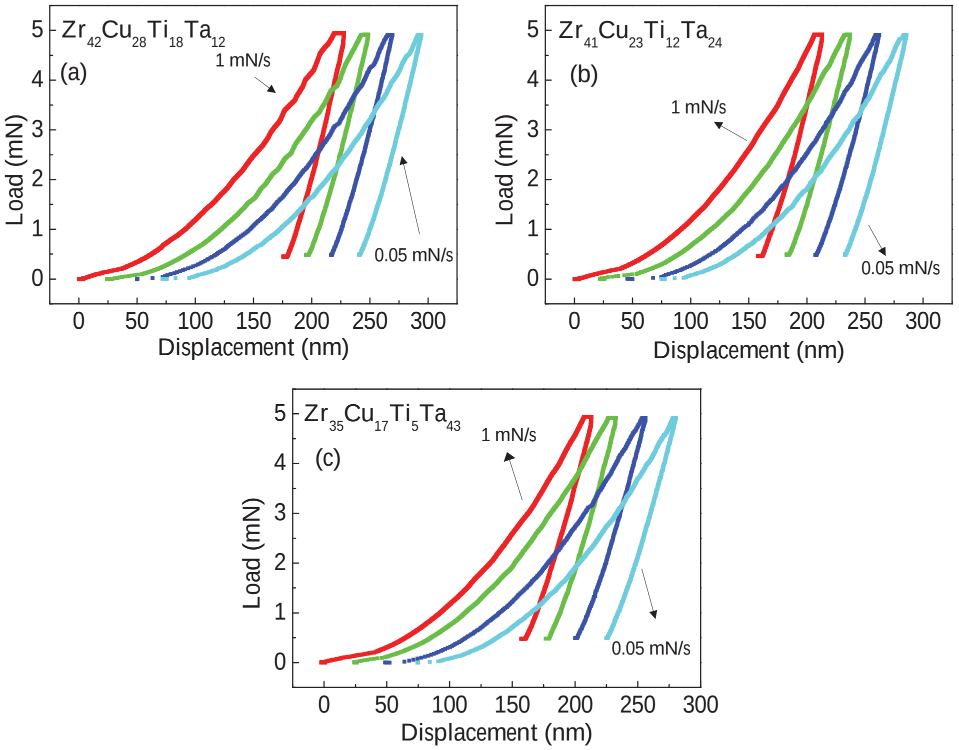

Fig. 4-17 The P-h curves of Zr-rich (a) $Zr_{45}Cu_{27}Ti_{15}Ta_{13}$, (b) $Zr_{41}Cu_{23}Ti_{12}Ta_{24}$, and (c) $Zr_{31}Cu_{15}Ti_{10}Ta_{44}$ thin film metallic glasses with different loading rates from 0.05 to 1 mN/s.

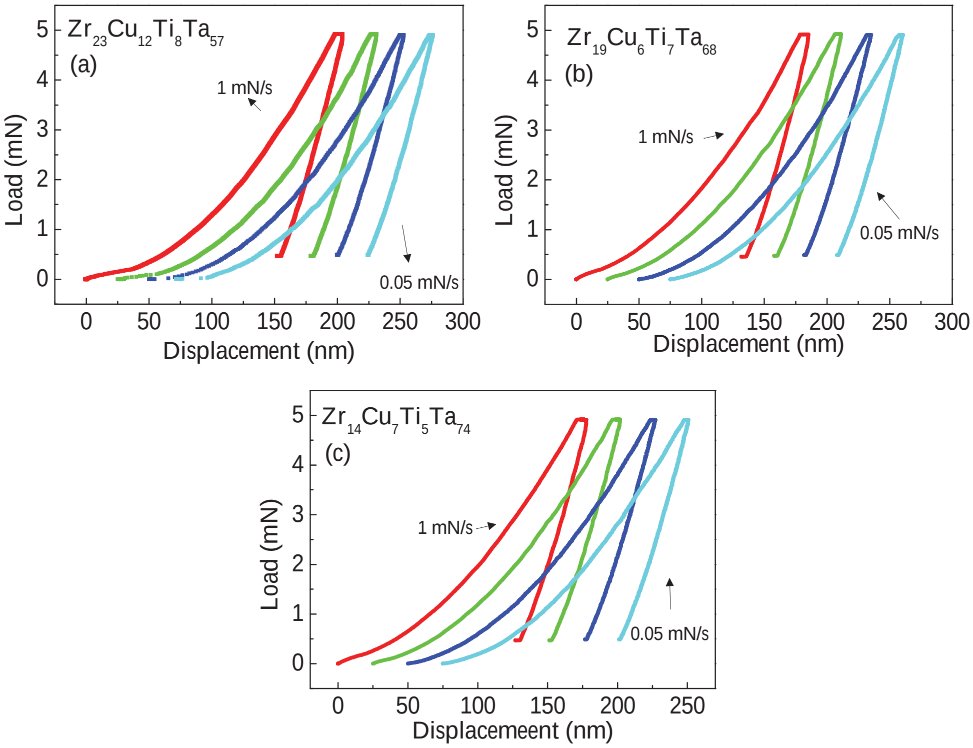

Fig. 4-18 The P-h curves of Ta-rich (a) $Zr_{23}Cu_{12}Ti_8Ta_{57}$, (b) $Zr_{19}Cu_6Ti_7Ta_{68}$, and (c) $Zr_{14}Cu_7Ti_5Ta_{74}$ thin film metallic glasses with different loading rates from 0.05 to 1 mN/s.

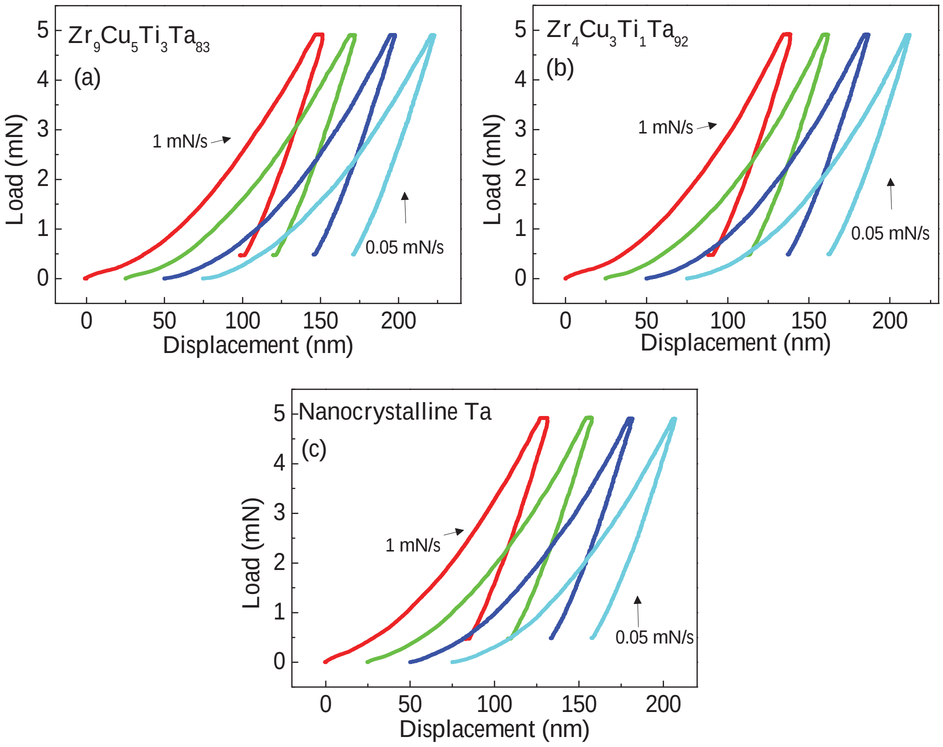

Fig. 4-19 The P-h curves of (a) $Zr_9Cu_5Ti_3Ta_{83}$, (b) $Zr_4Cu_3Ti_1Ta_{92}$, and (c) nanocrystalline pure Ta thin films with different loading rates from 0.05 to 1 mN/s.

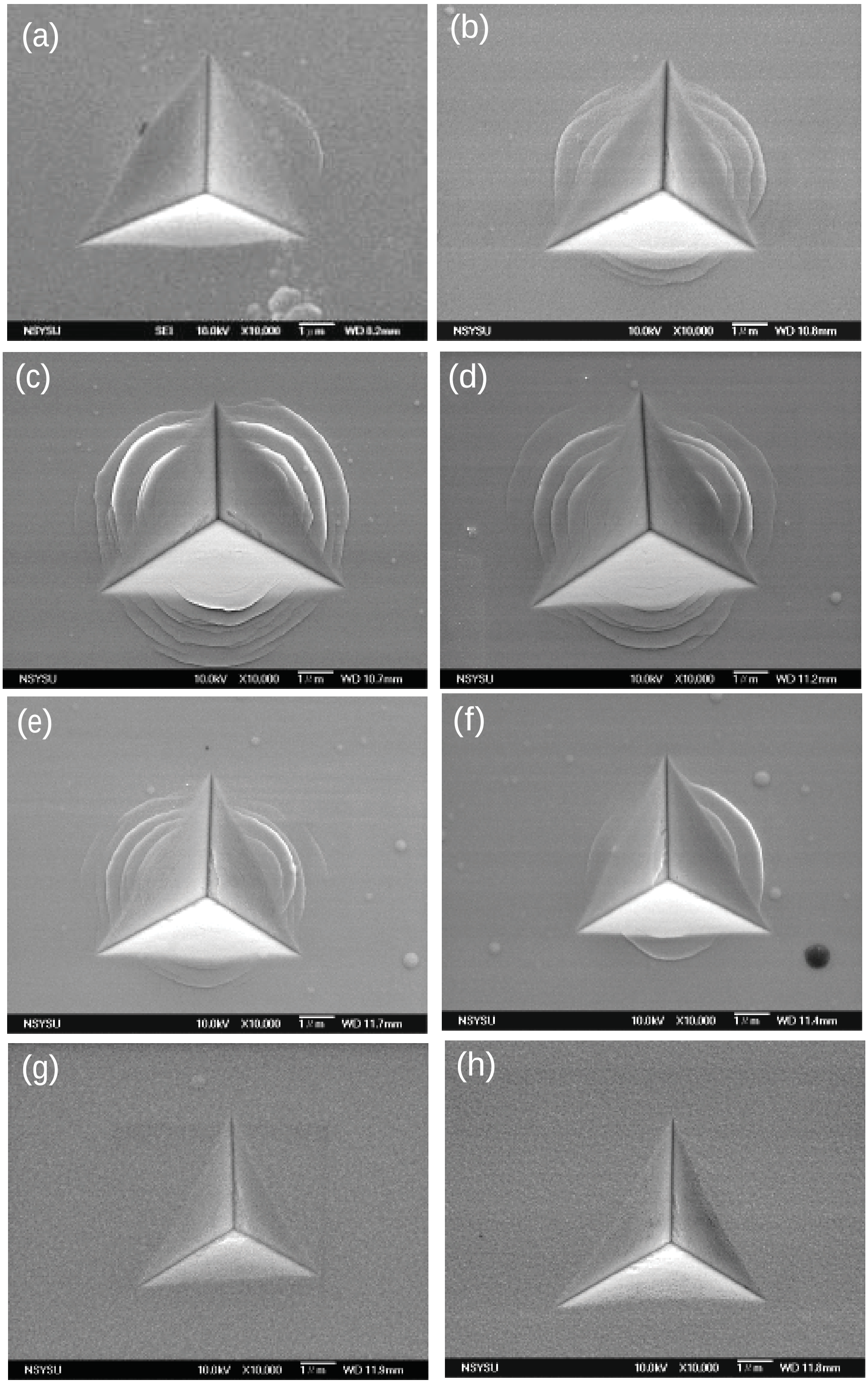

Fig. 4-20 Indentation marks of (a) $Zr_{45}Cu_{27}Ti_{15}Ta_{13}$, (b) $Zr_{41}Cu_{23}Ti_{12}Ta_{24}$, (c) $Zr_{31}Cu_{15}Ti_{10}Ta_{44}$, (d) $Zr_{23}Cu_{12}Ti_{8}Ta_{57}$, (e) $Zr_{19}Cu_{6}Ti_{7}Ta_{68}$, (f) $Zr_{14}Cu_{7}Ti_{5}Ta_{74}$, (g) $Zr_{9}Cu_{5}Ti_{3}Ta_{83}$, and (h) $Zr_{4}Cu_{3}Ti_{1}Ta_{92}$. All tests are set at 0.05 s^{-1} with a constant present of equal to 1000 nm.

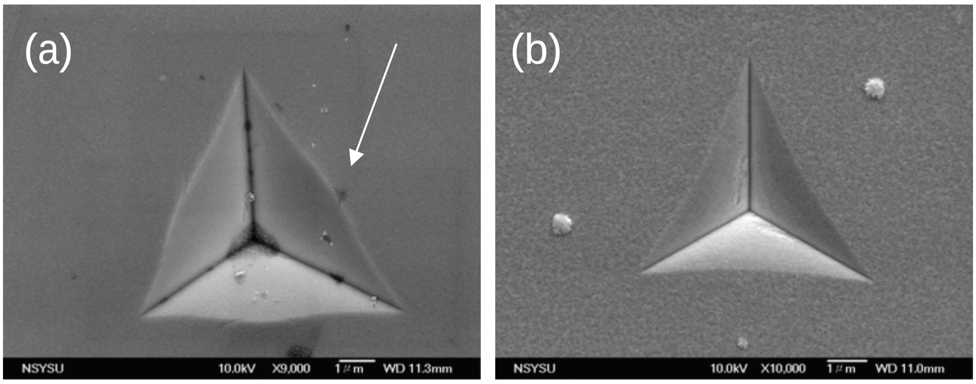

Fig. 4-21 Indentation marks of (a) $Zr_{55}Cu_{31}Ti_{14}$ and (b) β-Ta thin films.

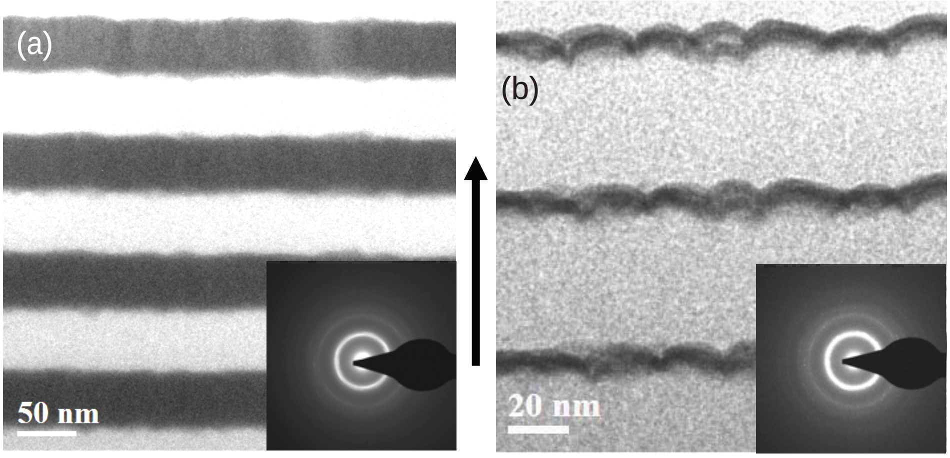

Fig. 4-22 Bright-field TEM images of the amorphous-ZrCuTi/crystalline-Ta nanocomposites consisting of (a) 50 nm/50 nm and (b) 50 nm/5 nm nanolaminate structure, respectively. The arrow direction means the deposition direction.

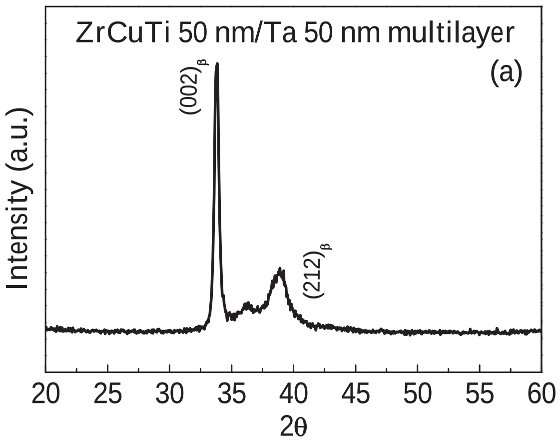

Fig. 4-23 XRD patterns of the ZrCuTi/Ta multilayered thin film consisting of (a) 50 nm/50 nm and (b) 50 nm/5 nm nanolaminate structure.

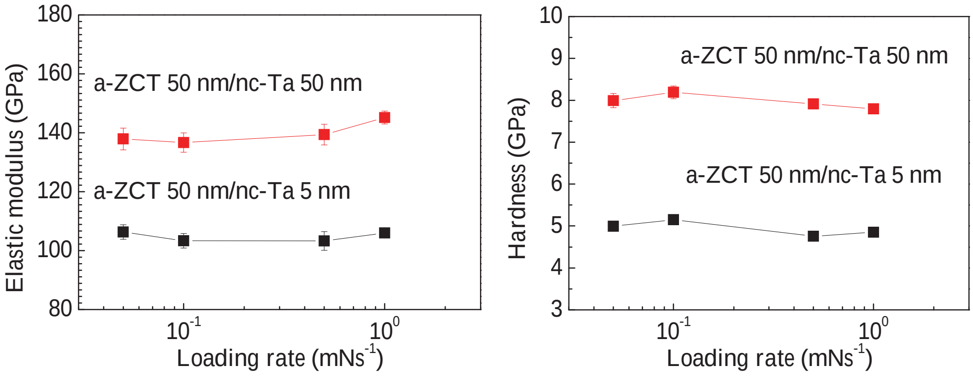

Fig. 4-24 (a) Elastic modulus and (b) hardbess of amorphous-ZrCuTi/crystalline-Ta nanocomposite consisting of 50 nm/50 nm and 50 nm/5 nm nanolaminate structure from 0.05 to 1 mN/s.

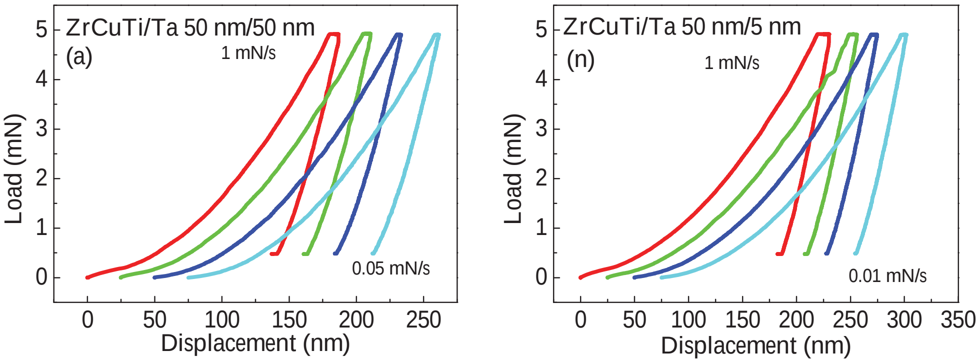

Fig. 4-25 The P-h curves of (a) amorphous-ZrCuTi/crystalline-Ta nanocomposite consisting of 50 nm/50 nm nanolaminate structure and (b) amorphous-ZrCuTi/crystalline-Ta nanocomposite consisting of 50 nm/5 nm nanolaminate structure with differenct loading rates from 0.05 to 1 mN/s.

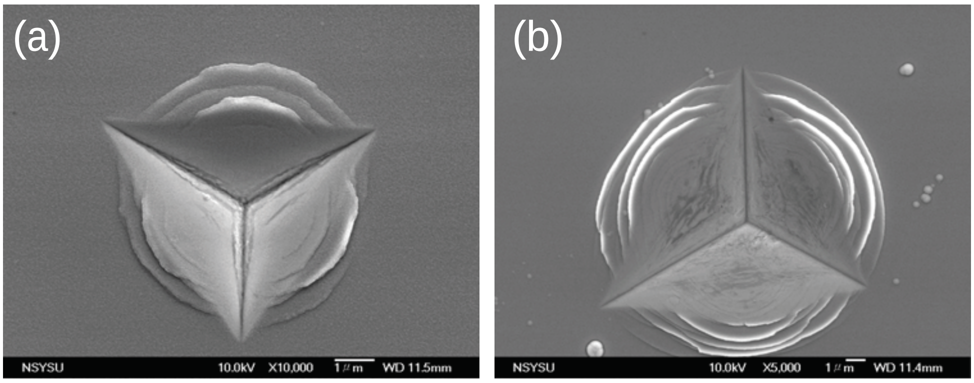

Fig. 4-26 Morphology of indentation marks of (a) ZrCuTi 50 nm/Ta 50 nm and (b) ZrCuTi 50 nm/ Ta 5 nm.

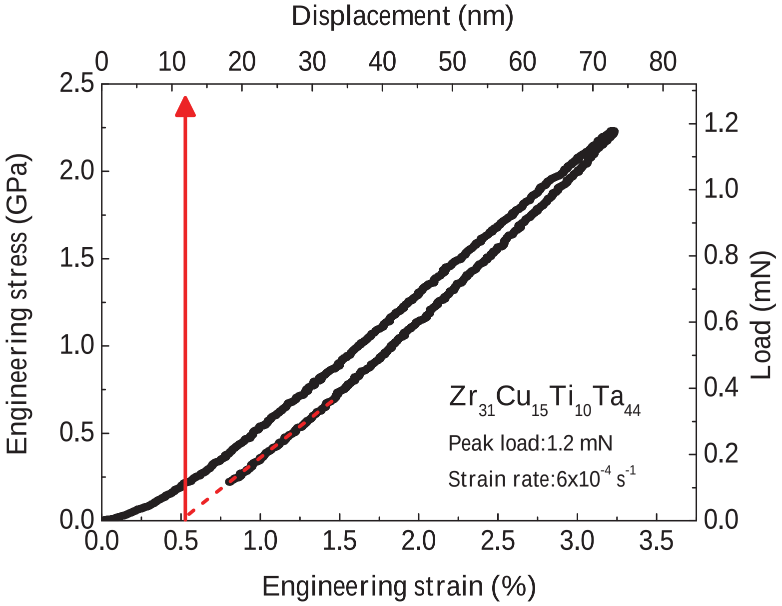

Fig. 4-27 Stress-strain curve of $Zr_{31}Cu_{15}Ti_{10}Ta_{44}$ in the elastic range. The dash line is calculated by the linear extrapolation.

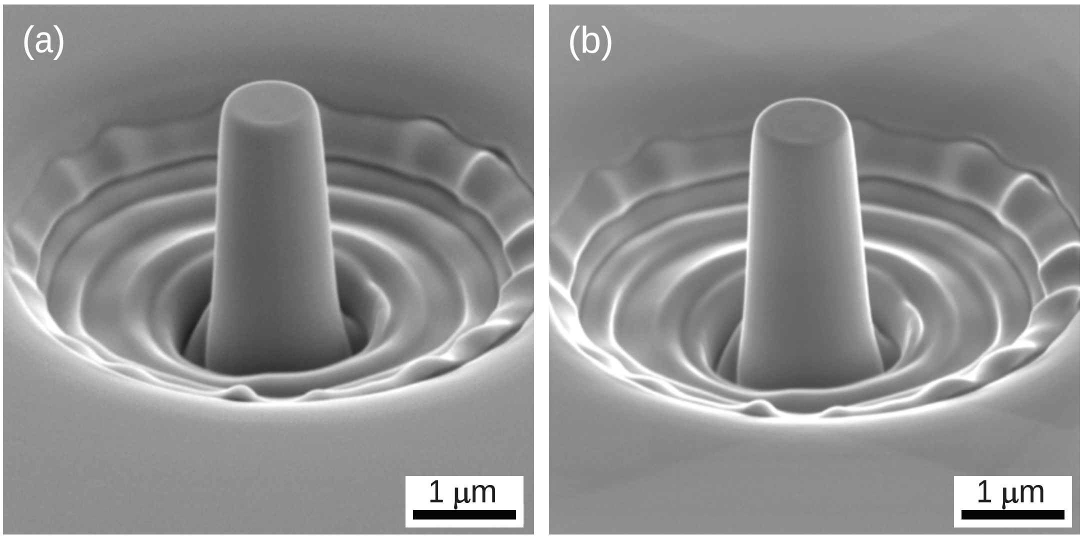

Fig. 4-28 Appearance of (a) as-fabricated and (b) elastic-deformed micropillar of $Zr_{31}Cu_{15}Ti_{10}Ta_{44}$.

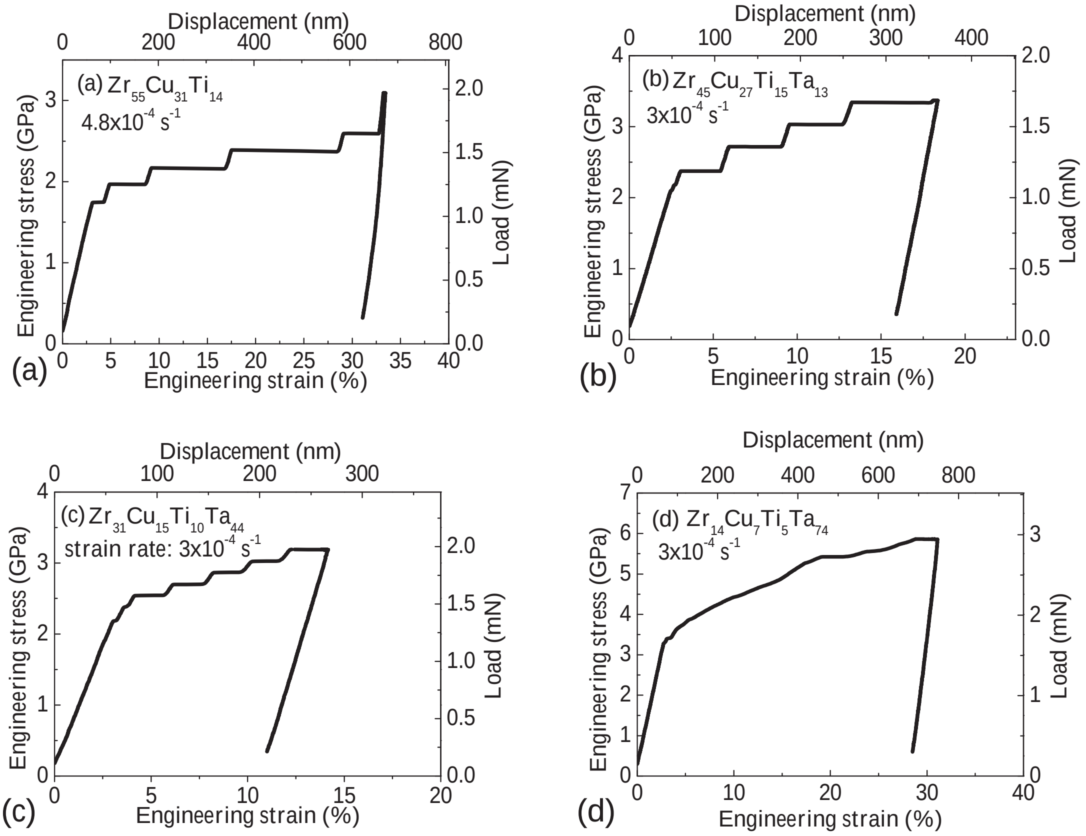

Fig. 4-29 Engineering stress-strain curves of the micropillars of (a) $Zr_{55}Cu_{31}Ti_{14}$, (b) $Zr_{45}Cu_{27}Ti_{15}Ta_{13}$ TFMGs, (c) $Zr_{31}Cu_{15}Ti_{10}Ta_{44}$ TFMGs, and (d) $Zr_{14}Cu_7Ti_5Ta_{74}$ TFMGs.

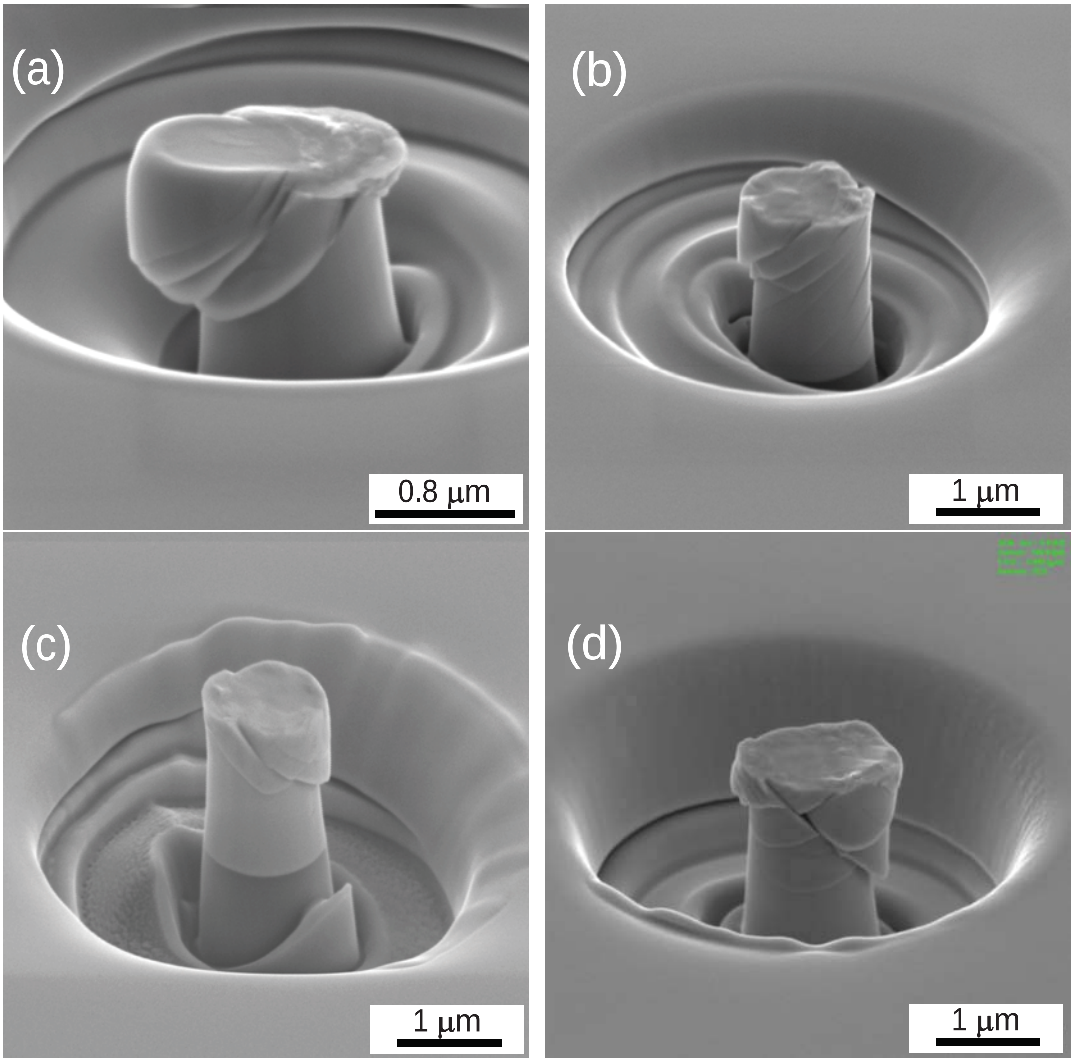

Fig. 4-30 Deformed micropillars of (a) $Zr_{55}Cu_{31}Ti_{14}$ (b) $Zr_{45}Cu_{27}Ti_{15}Ta_{13}$ TFMGs, (c) $Zr_{31}Cu_{15}Ti_{10}Ta_{44}$ TFMGs, and (d) $Zr_{14}Cu_{7}Ti_{5}Ta_{74}$ TFMGs.

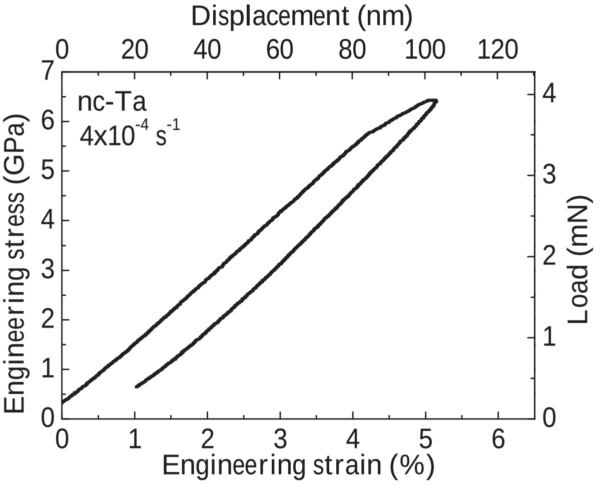

Fig. 4-31 Engineering stress-strain curve of nanocrystalline pure Ta micropillar at $4\text{x}10^{-4}\ \text{s}^{-1}$.

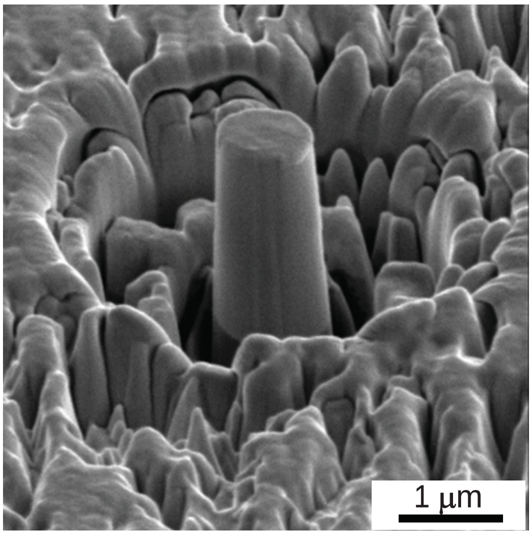

Fig. 4-32 Deformed micropillar of Ta.

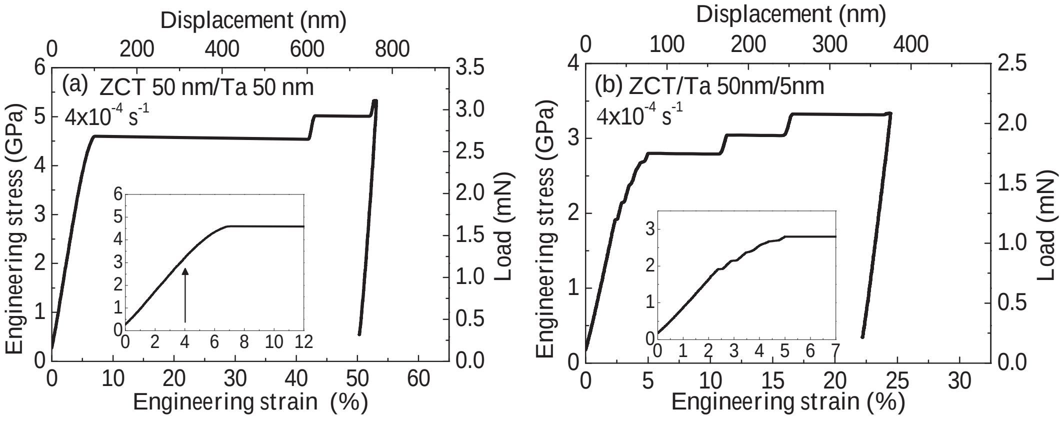

Fig. 4-33 Engineering stress-strain curves of (a) ZrCuTi 50 nm/Ta 50 nm and (b) ZrCuTi 50 nm/Ta 5 nm.

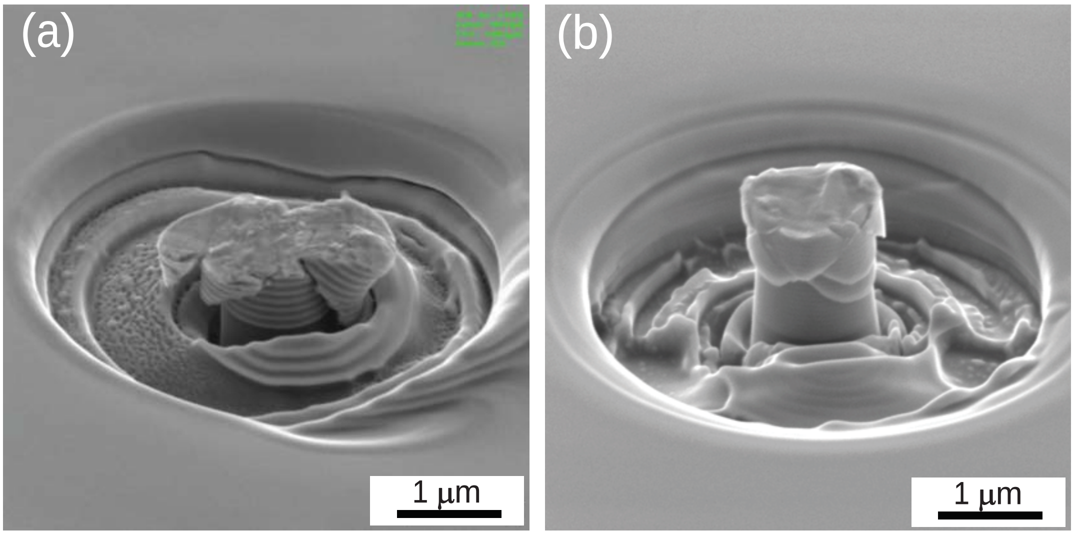

Fig. 4-34 Deformed micropillars of (a) ZrCuTi 50 nm/Ta 50 nm and (b) ZrCuTi 5 nm/Ta 50 nm.

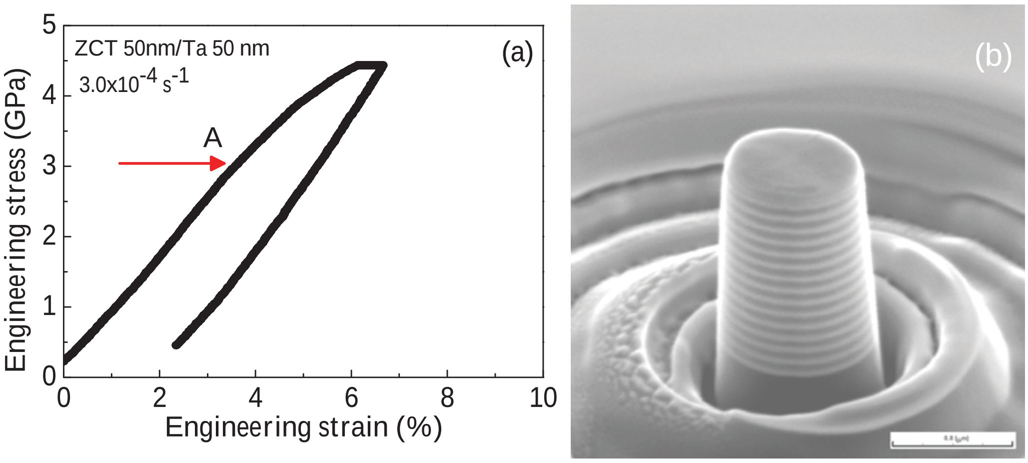

Fig. 4-35 (a) Engineering curve of ZrCuTi 50 nm/Ta 50 nm at ~5% strain. (b) Deformed micropillar at ~5%.

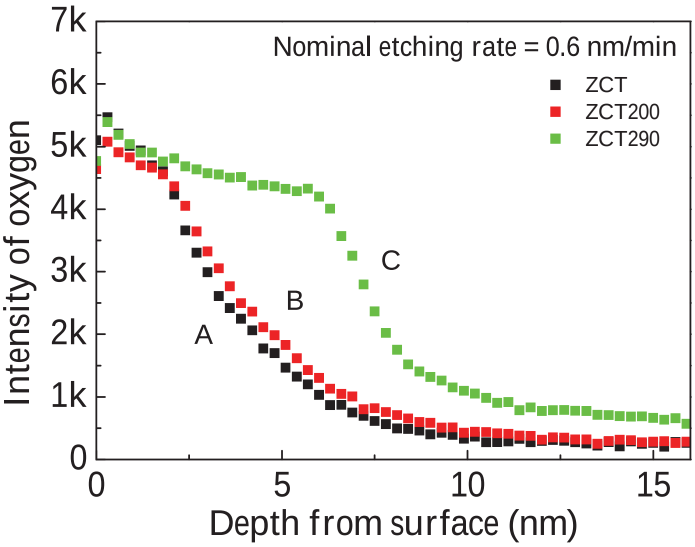

Fig. 5-1 Comparison of the doping depth of oxygen among as-deposited and annealed ZrCuTi TFMGs.

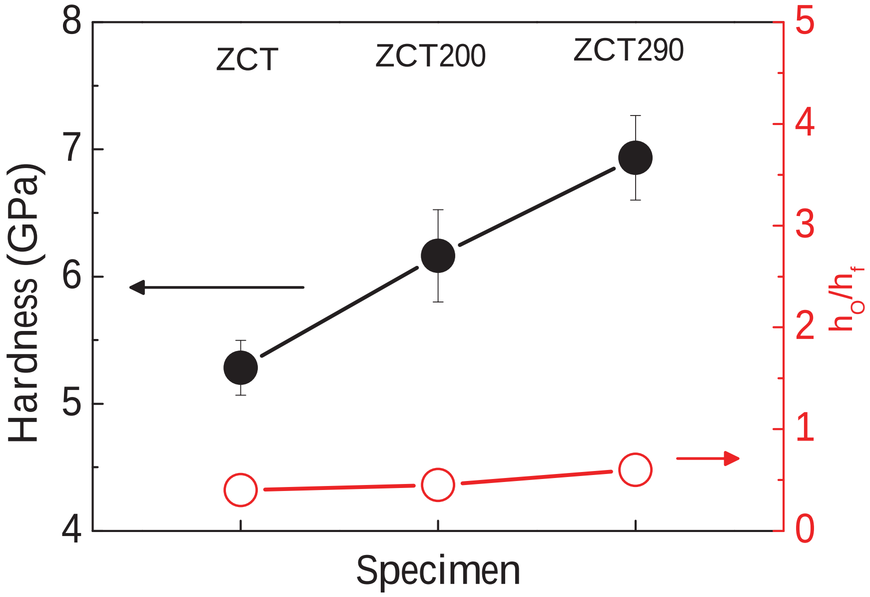

Fig. 5-2 Relationship between the hardness and the ratio of oxygen layer/film thickness (h_O/h_f).

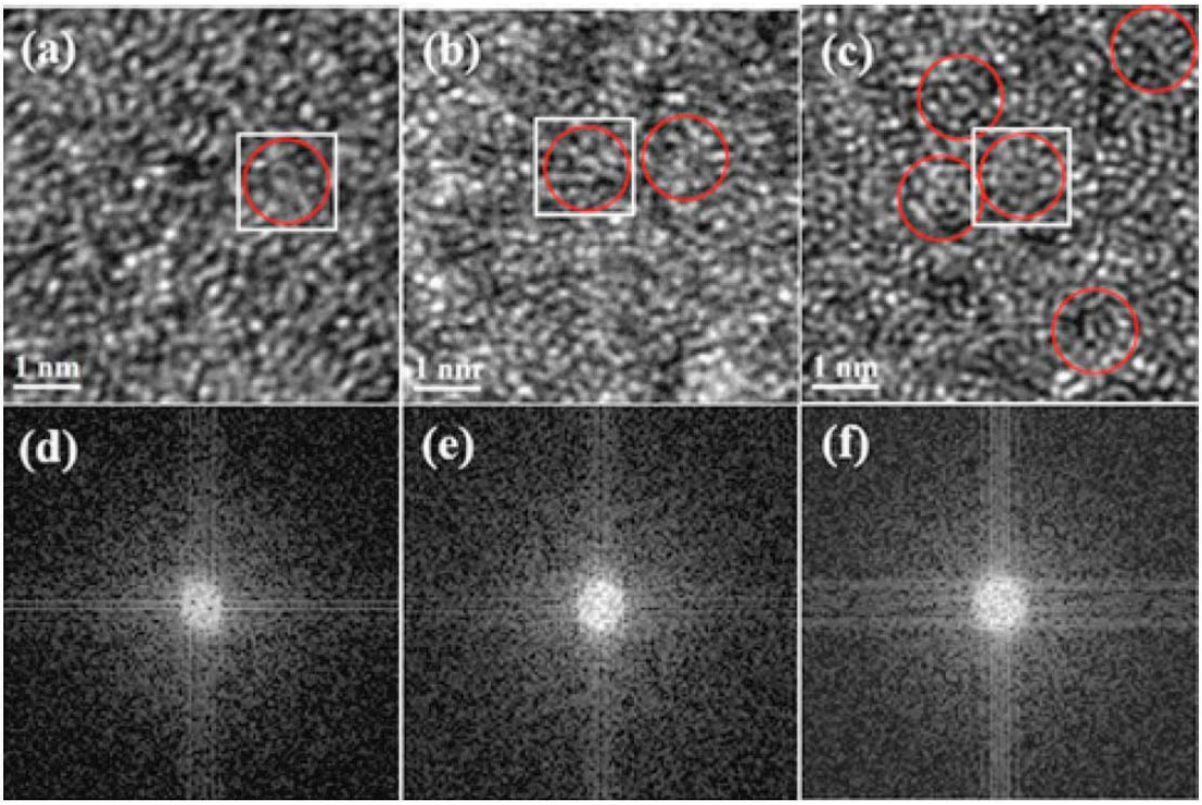

Fig. 5-3 The high-resolution TEM image of (a) specimen ZCT, (b) specimen ZCT200, and (c) specimen ZCT290. The marked circles correspond to the medium-range-ordering clusters. (d), (e), and (f) show the Fourier transform diffraction patterns for the white squares in (a), (b) and (c), respectively.

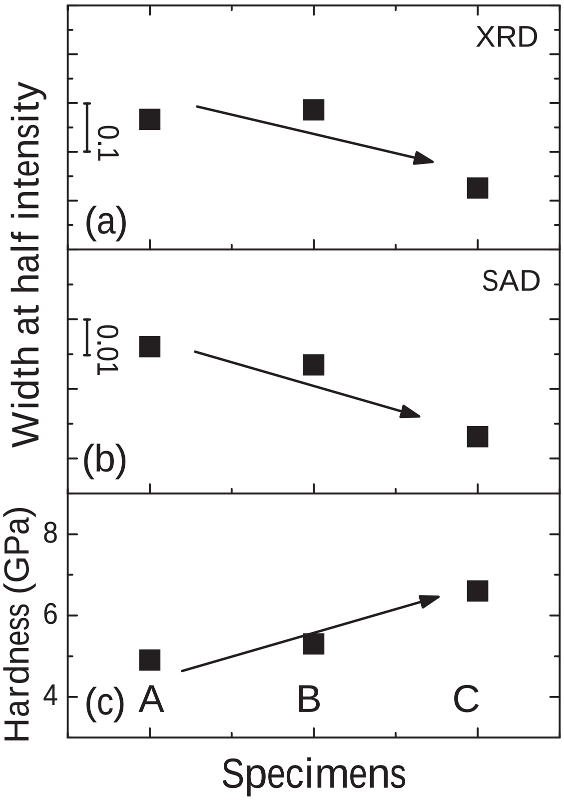

Fig. 5-4 The variation of hardness with the microstructural change. The FWHM is calculated from the (a) XRD and (b) TEM results, respectively, utilizing the peak fitting with the amplitude version of Gaussian peak function.

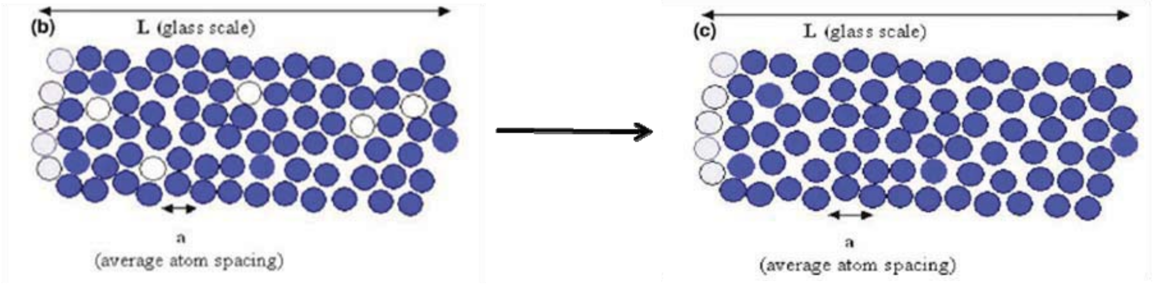

Fig. 5-5 Evolution of atomic packing in amorphous alloy after structural relaxation [99].

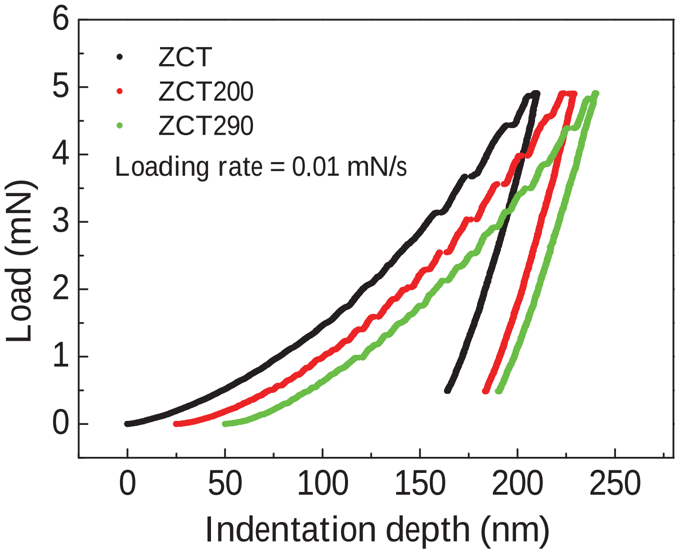

Fig. 5-6 P-h curves of $Zr_{52}Cu_{29}Ti_{19}$ TFMGs at as-deposited and annealed statue. The interval between neighbor curves is 25 nm.

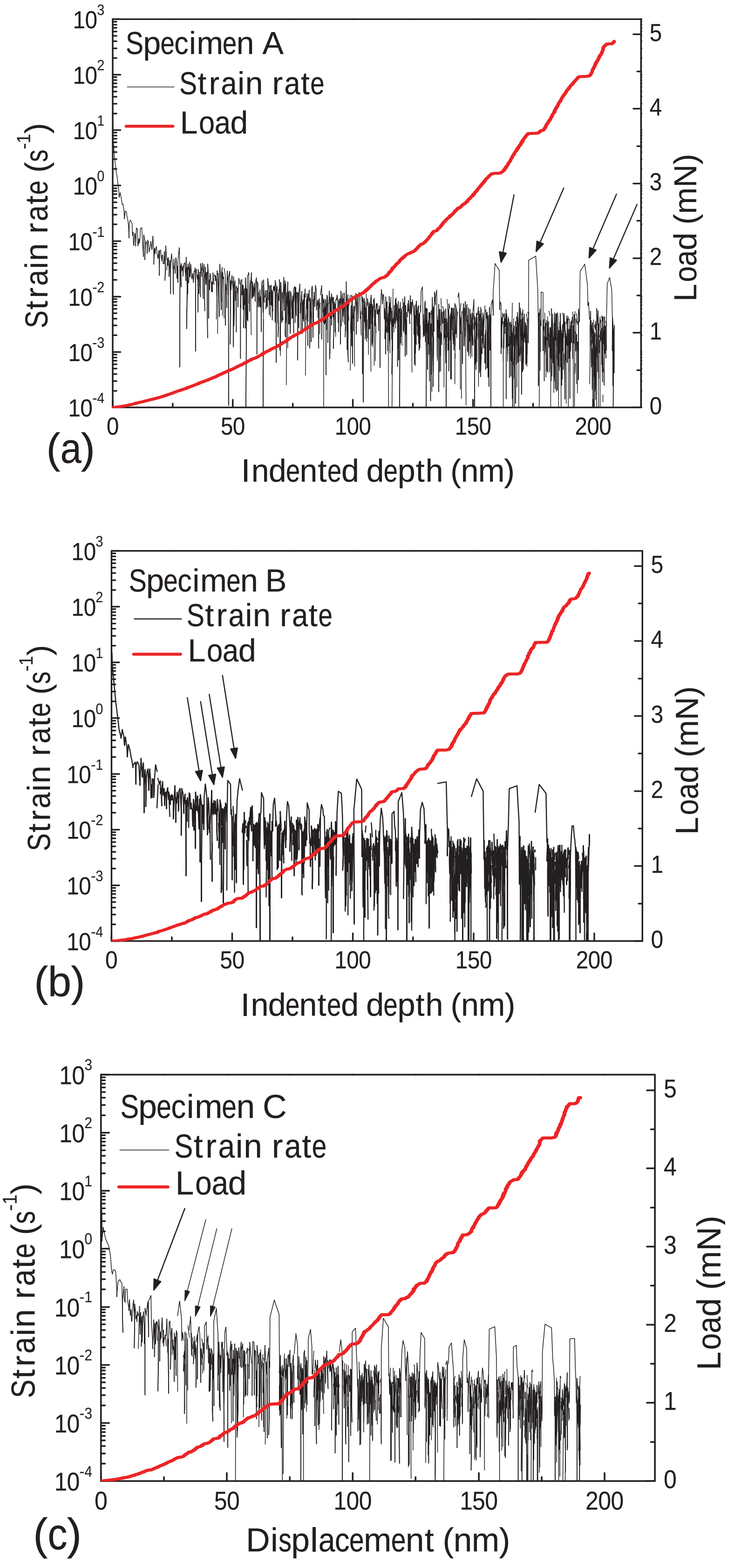

Fig. 5-7 Relation between the strain rate and load versus indentation displacement for (a) ZCT, (b) ZCT200, and (c) ZCT290.

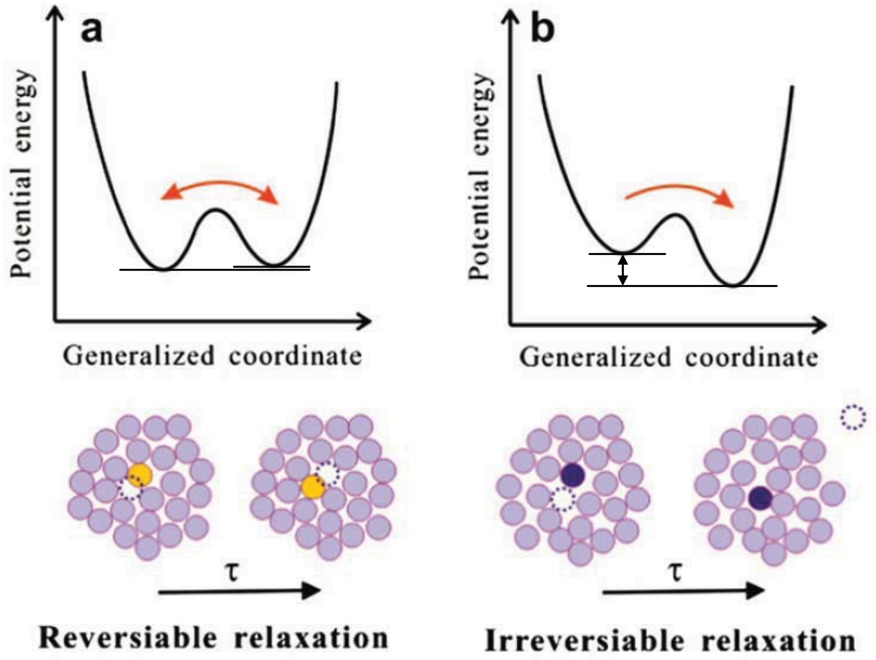

Fig. 5-8 The schematic drawings of metallic glass showing the models of dynamics recovery during cyclic loading: (a) the dynamic recovery model of reversible relaxation centers (RRCs) with a symmetry potential barrier which causes the local elastic events during the cyclic loading process, (b) the dynamic recovery model of irreversible relaxation centers (IRRCs) with an asymmetry potential barrier which causes the local plastic events during the cyclic loading process. (For interpretation of the references to colour in this figure legend, the reader is referred to the web version of this article) [108].

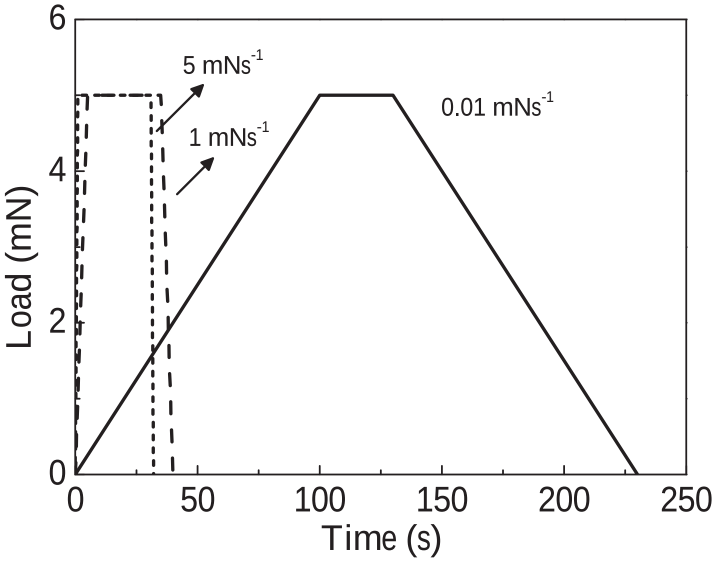

Fig. 5-9 Load functions of the holding tests.

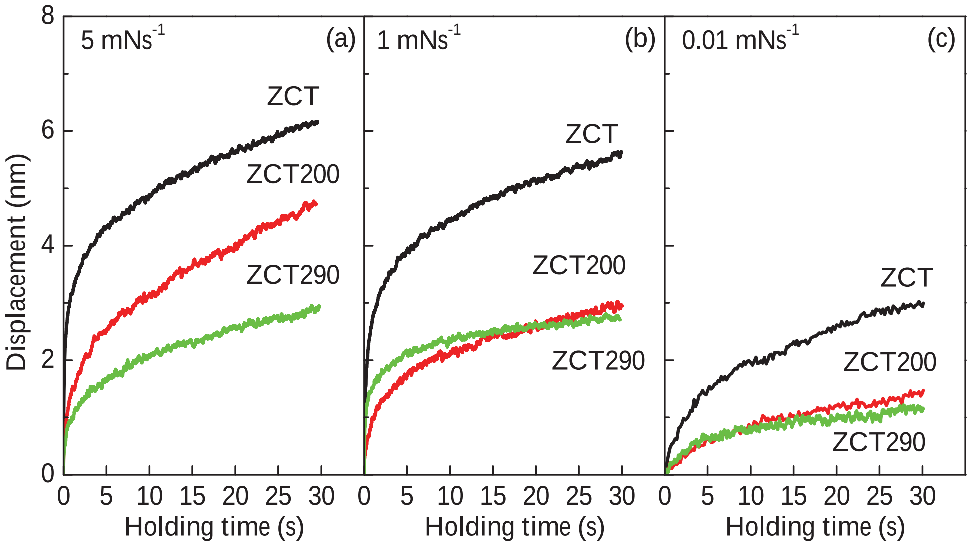

Fig. 5-10 Time-displacement curves of as-deposited and annealed ZrCuTi TFMGs tested at (a) 5, (b) 1, and (c) 0.01 mNs^{-1}.

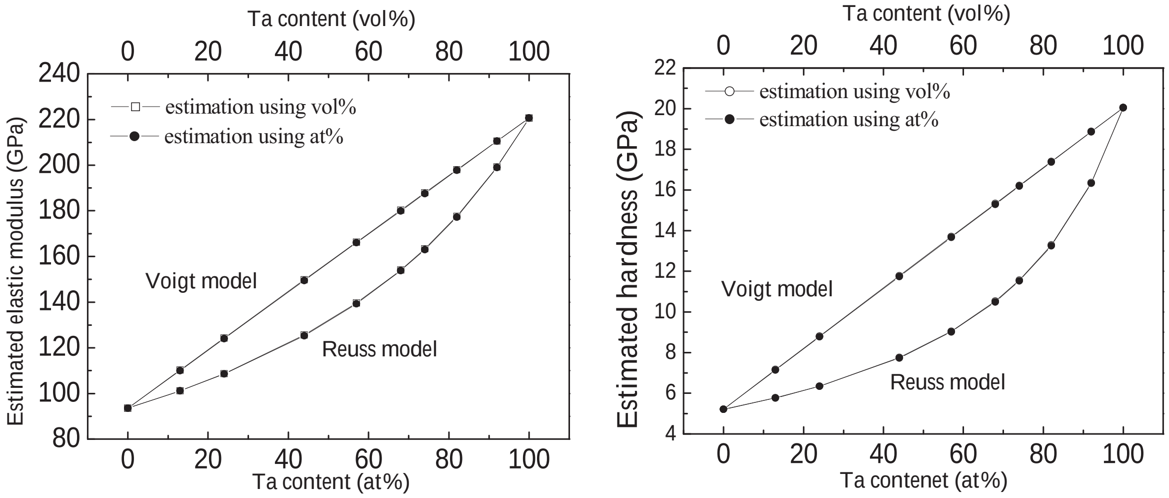

Fig. 5-11 Estimation of (a) elastic modulus and (b) hardness using rule of mixture.

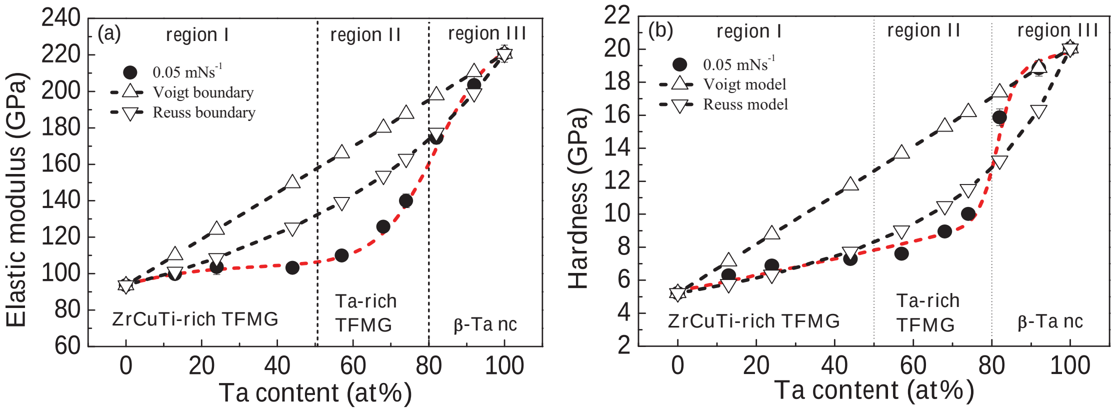

Fig. 5-12 Relationship between Ta content and (a) elastic modulus and (b) hardness.

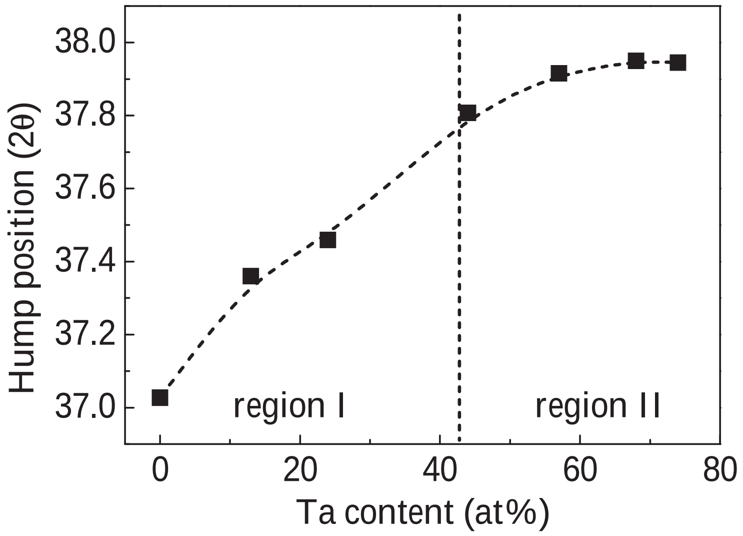

Fig. 5-13 Relationship between the amorphous hump position and the Ta content

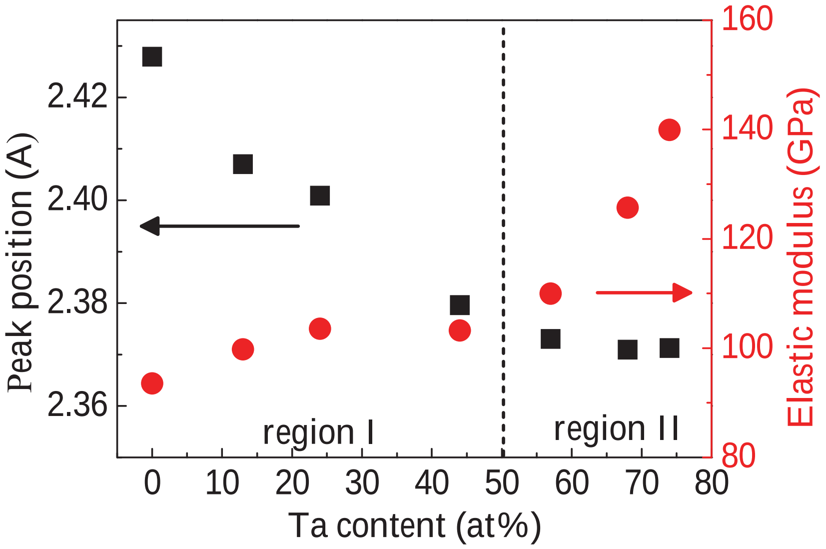

Fig. 5-14 Relationship between peak position and elastic modulus in a series of ZrCuTiTa TFMGs.

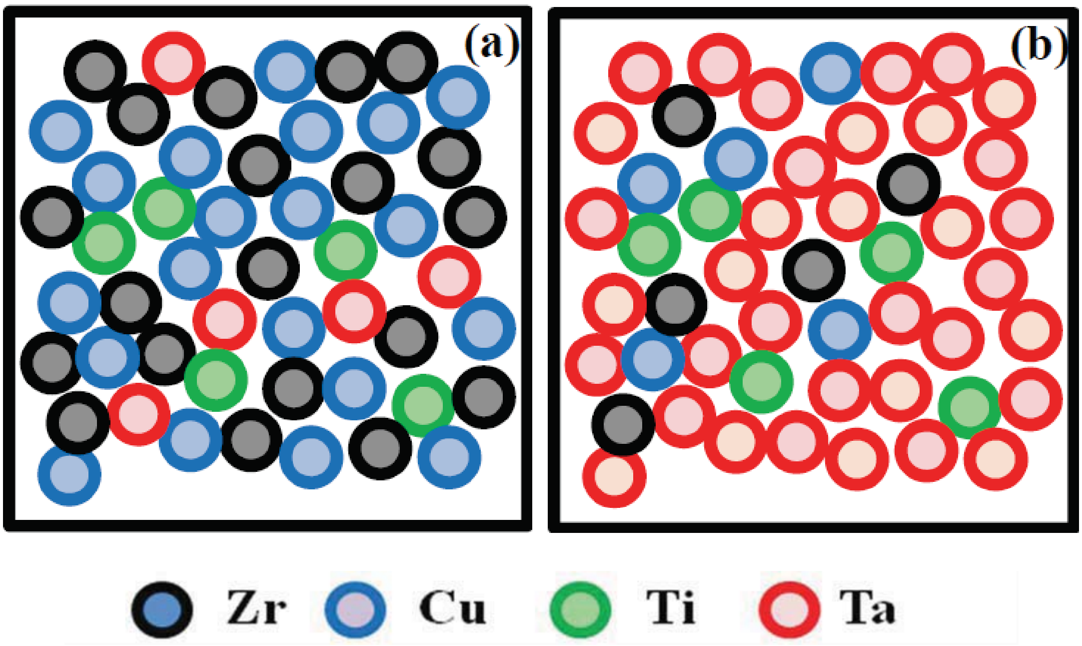

Fig. 5-15 Schemes of atomic packing in (a) $Zr_{45}Cu_{27}Ti_{15}Ta_{13}$ and (b) $Zr_{14}Cu_7Ti_5Ta_{74}$ TFMGs.

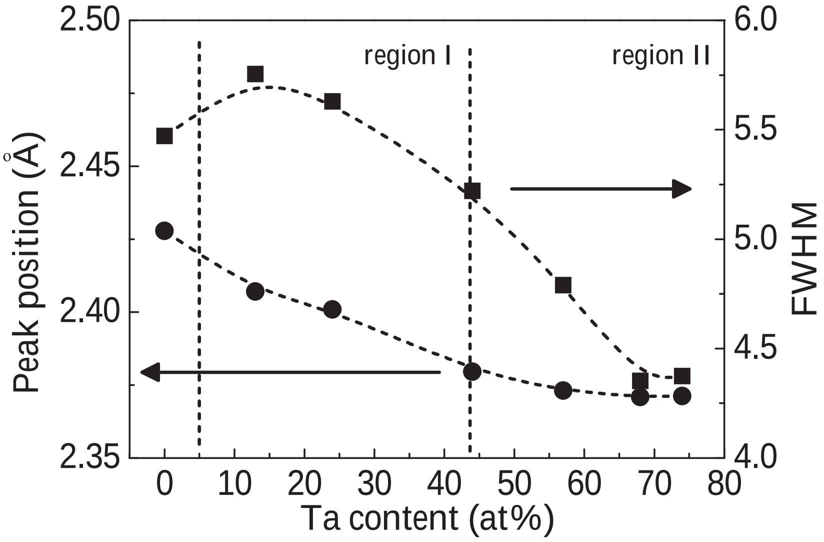

Fig. 5-16 Relationship between peak position and FWHM in a series of ZrCuTiTa TFMGs.

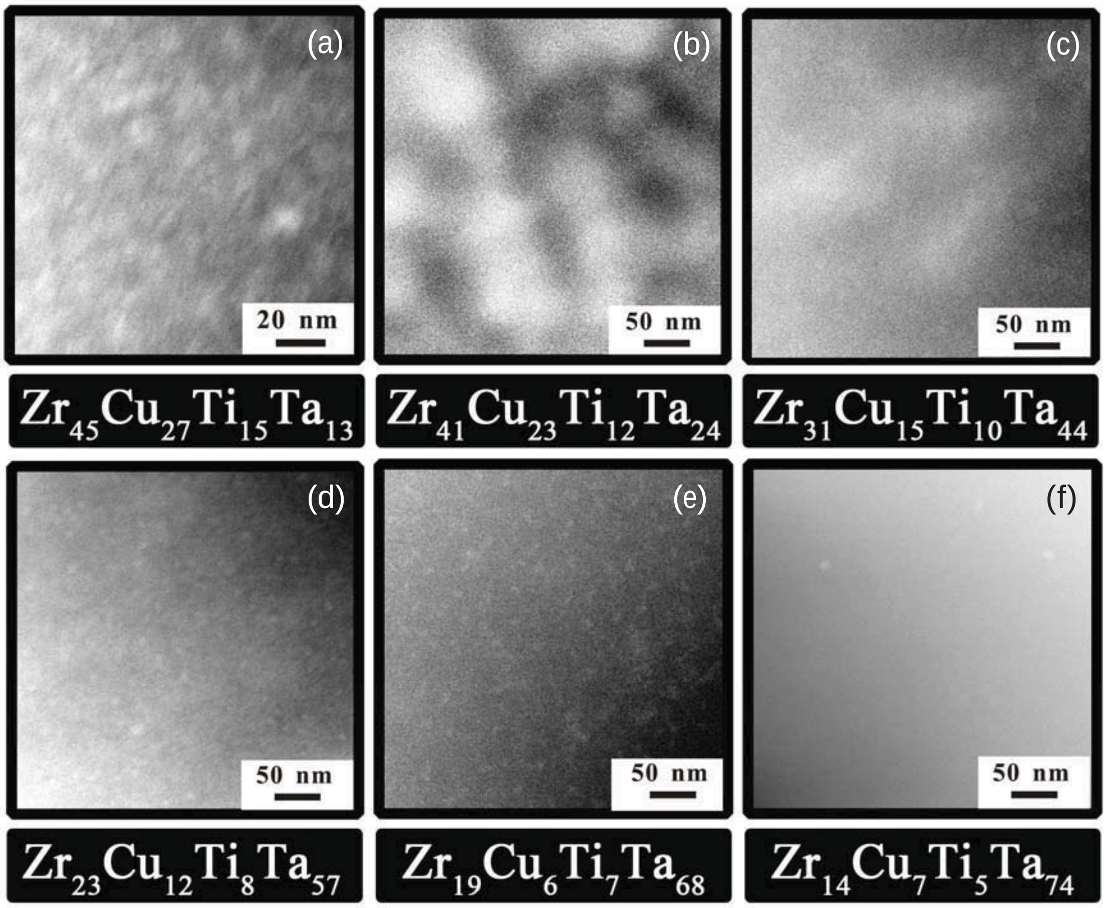

Fig. 5-17 Z-contrast image of (a) $Zr_{45}Cu_{27}Ti_{15}Ta_{13}$, (b) $Zr_{41}Cu_{23}Ti_{12}Ta_{24}$, (c) $Zr_{31}Cu_{15}Ti_{10}Ta_{44}$, (d) $Zr_{23}Cu_{12}Ti_{8}Ta_{57}$, (e) $Zr_{19}Cu_{6}Ti_{7}Ta_{68}$, and (f) $Zr_{14}Cu_{7}Ti_{5}Ta_{74}$ TFMGs.

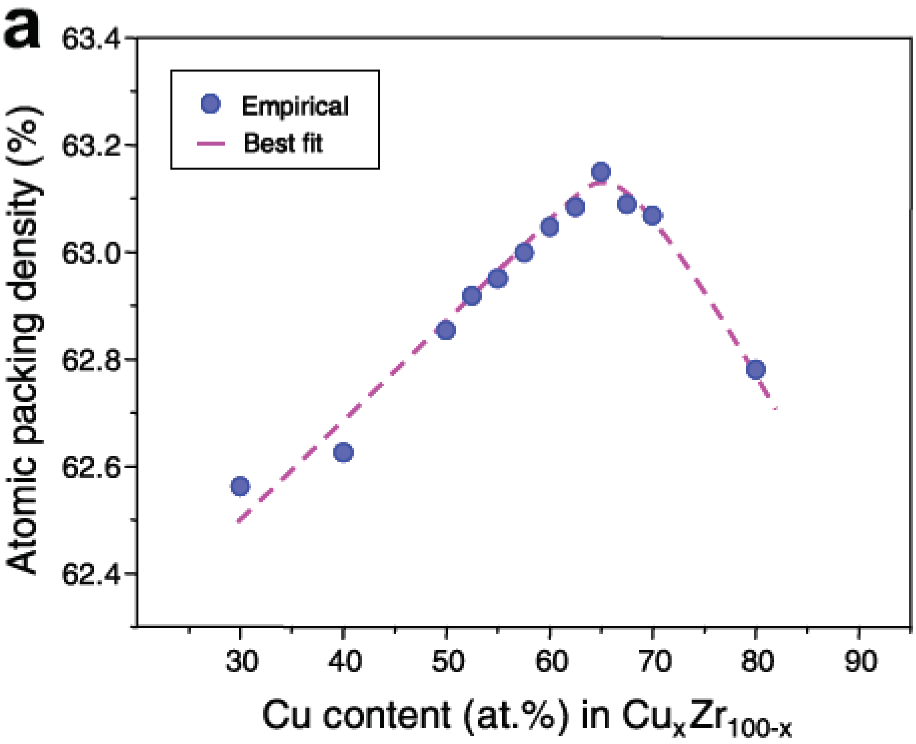

Fig. 5-18 Variations in the atomic packing density as a function of the composition in the Cu_xZr_{1-x} alloys [118].

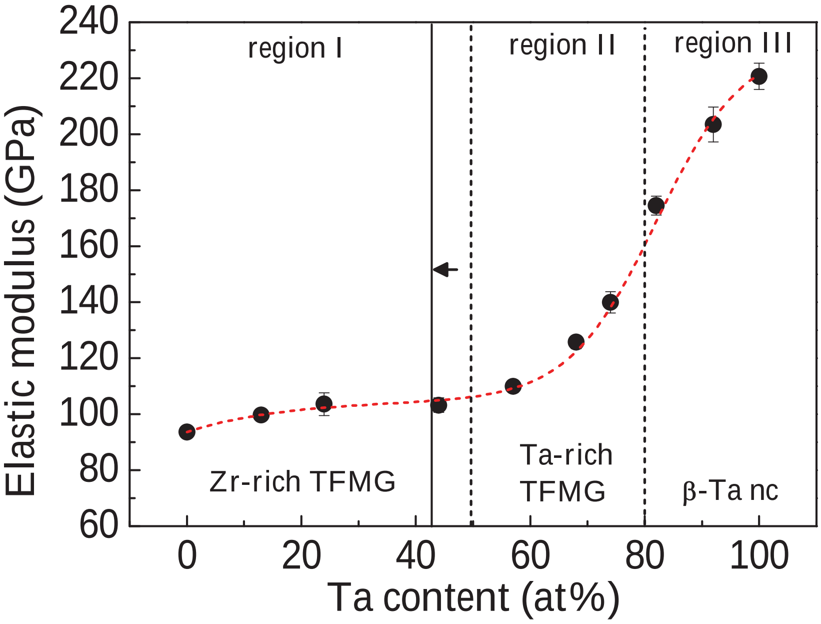

Fig. 5-19 Corrected phase boundary between region I and II.

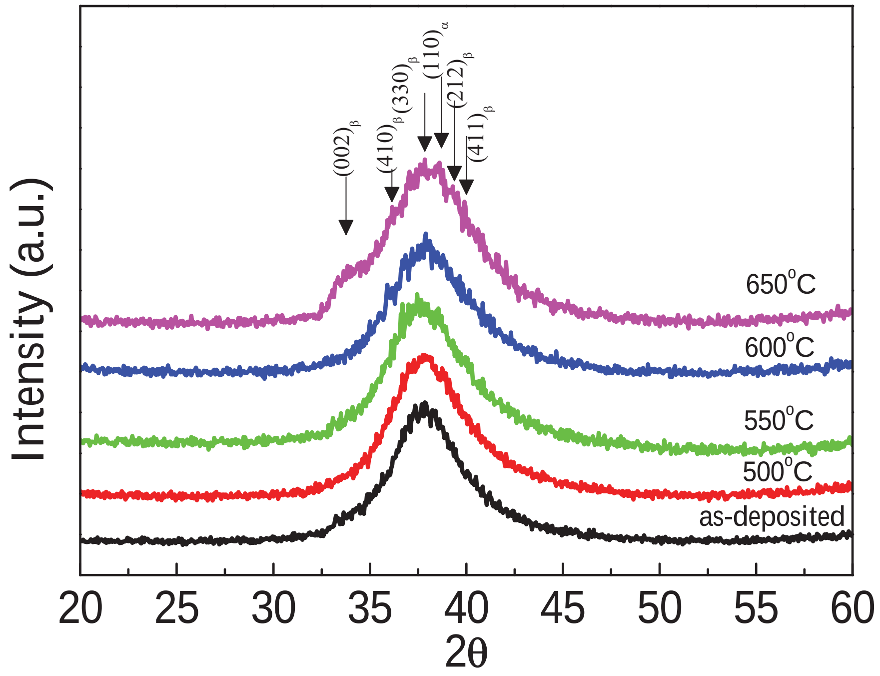

Fig. 5-20 Crystallization of $Zr_{14}Cu_7Ti_5Ta_{74}$ TFMGs by annealing.

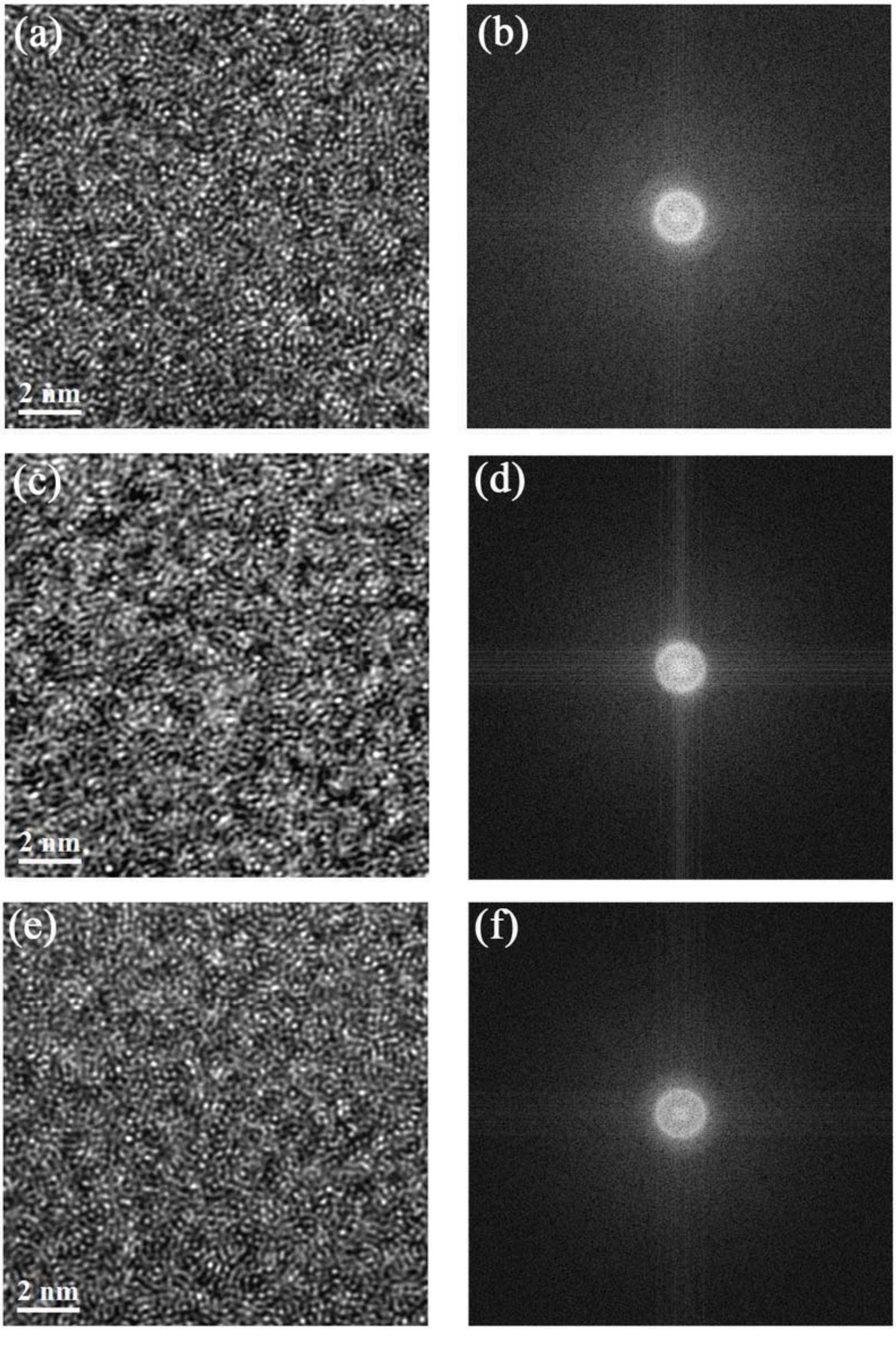

Fig. 5-21 (a) Lattice image and (b) FFT pattern of $Zr_{45}Cu_{27}Ti_{15}Ta_{13}$ TFMGs. (c) Lattice image and (d) FFT pattern of $Zr_{41}Cu_{23}Ti_{12}Ta_{24}$ TFMGs. (e) Lattice image and (f) FFT pattern of $Zr_{31}Cu_{15}Ti_{10}Ta_{44}$ TFMGs.

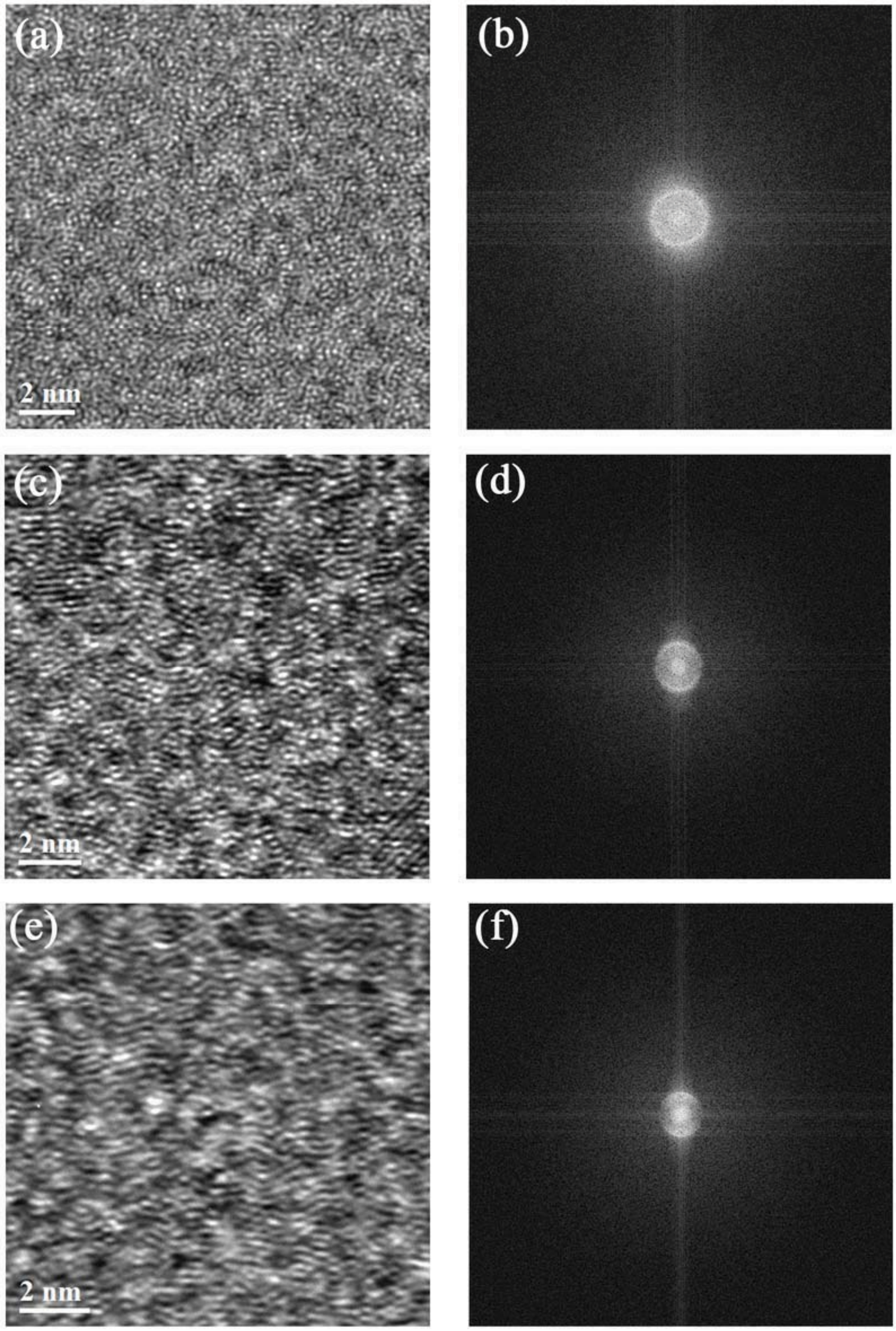

Fig. 5-22 (a) Lattice image and (b) FFT pattern of $Zr_{23}Cu_{12}Ti_8Ta_{57}$ TFMGs. (c) Lattice image and (d) FFT pattern of $Zr_{19}Cu_6Ti_7Ta_{68}$ TFMGs. (e) Lattice image and (f) FFT pattern of $Zr_{14}Cu_7Ti_5Ta_{74}$ TFMGs.

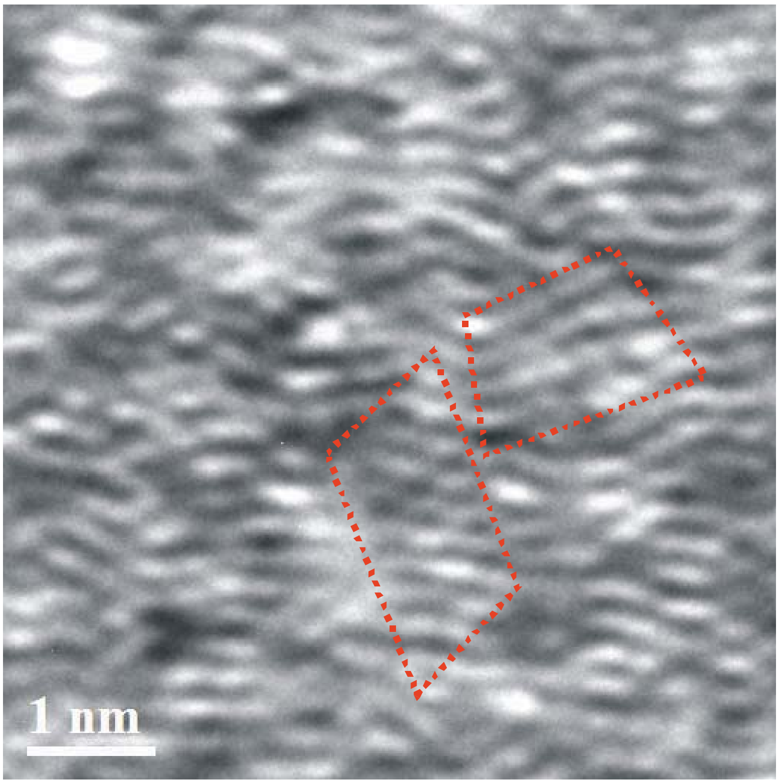

Fig. 5-23 High-magnified lattice image of $Zr_{14}Cu_7Ti_5Ta_{74}$ TFMGs.

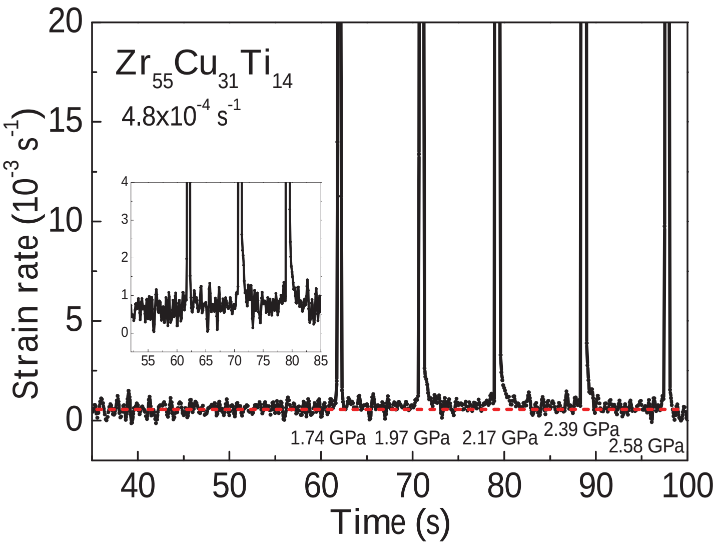

Fig. 5-24 Time-strain rate curve of amoprhous $Zr_{55}Cu_{31}Ti_{14}$ pillar.

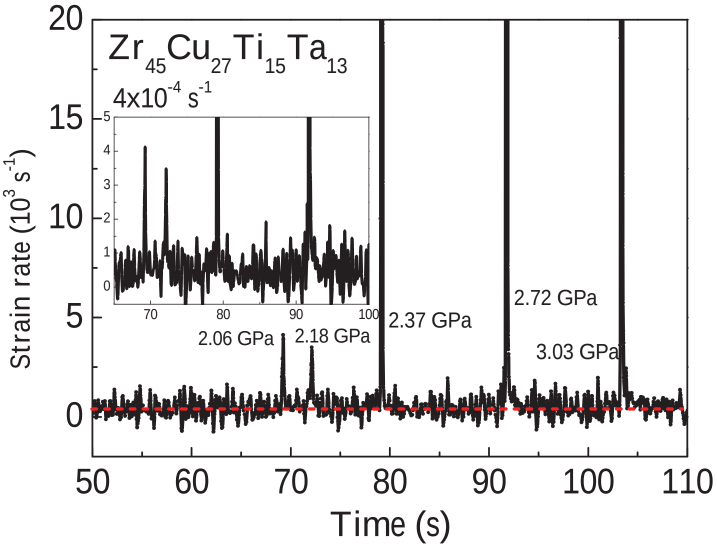

Fig. 5-25 Time-strain rate curve of amoprhous $Zr_{45}Cu_{27}Ti_{15}Ta_{13}$ pillar.

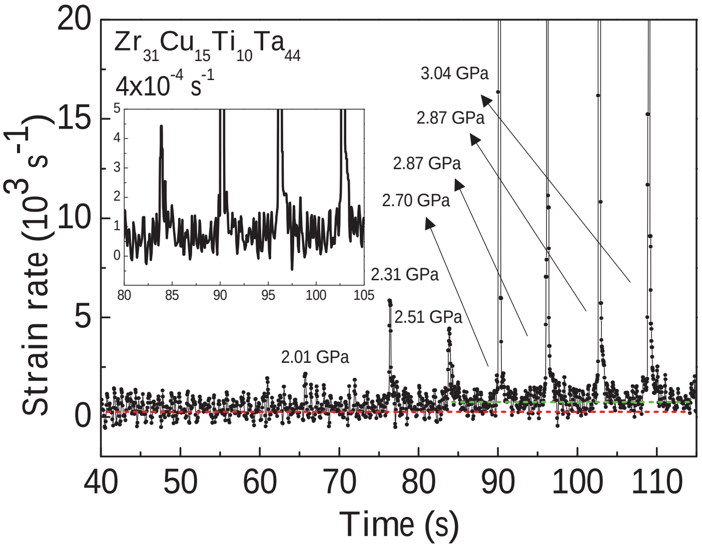

Fig. 5-26 Time-strain rate curve of amoprhous $Zr_{31}Cu_{15}Ti_{10}Ta_{44}$ pillar.

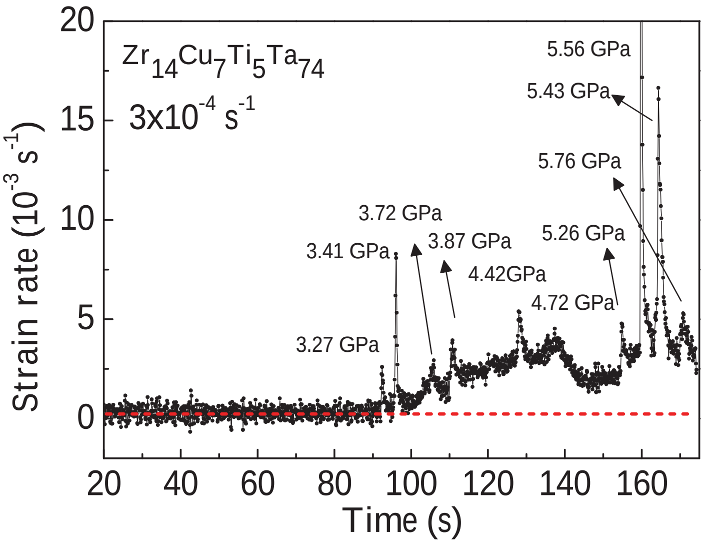

Fig. 5-27　Time-strain rate curve of amoprhous $Zr_{14}Cu7Ti_5Ta_{74}$ pillar.

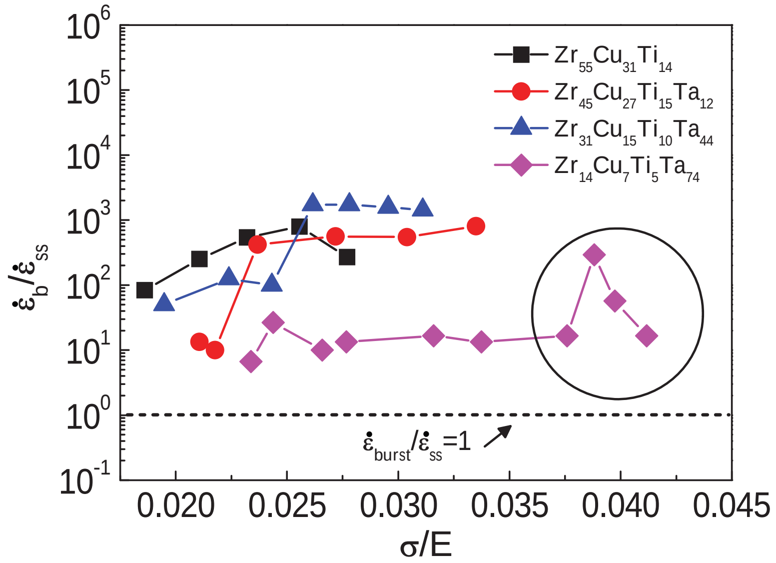

Fig. 5-28　Relationship between $\dot{\varepsilon}_b/\dot{\varepsilon}_e$ and σ/E

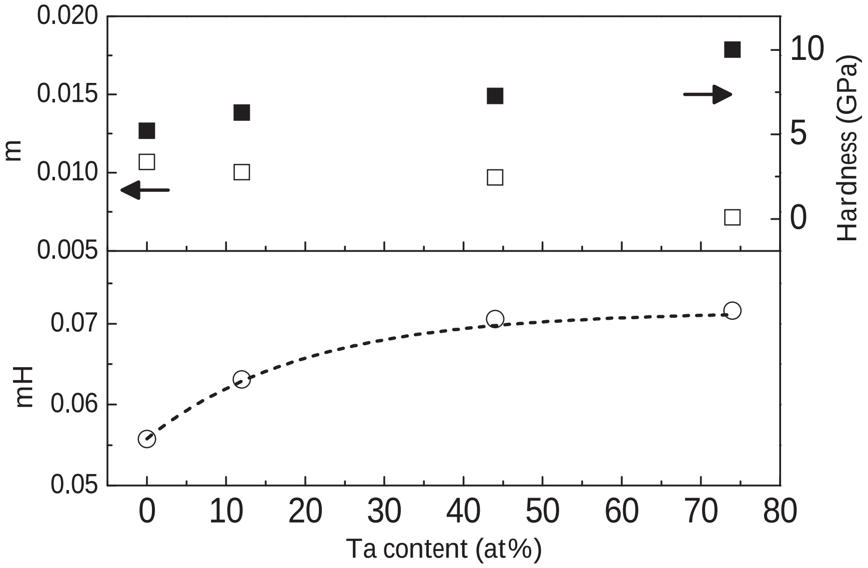

Fig. 5-29 Relationship between (a) strain rate sensitivity and hardness, (b) the product of the strain rate sensitivity and hardness and Ta content.

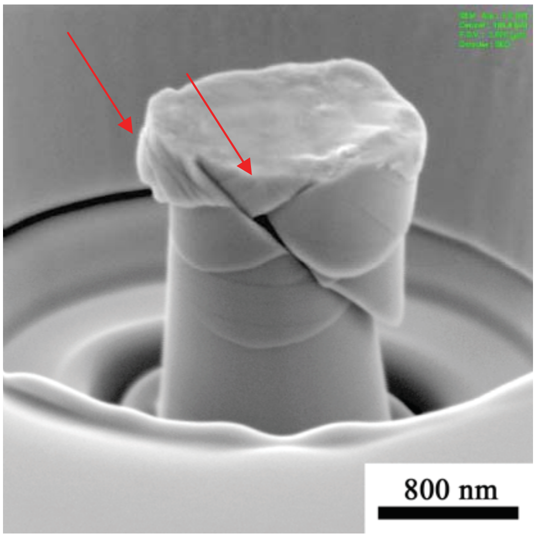

Fig. 5-30 High-magnification SEM image of deformed $Zr_{14}Cu_7Ti_5Ta_{74}$ pillar. Multiple shear bands are marked using arrows.

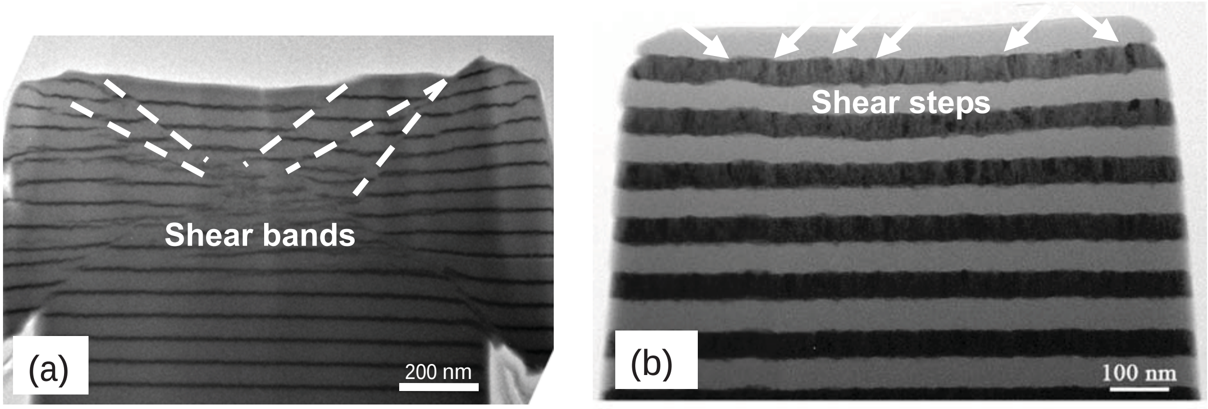

Fig. 5-31 The high-magnification TEM bright field images of the deformed (a) ZrCuTi 50 nm/Ta 5 nm pillar and (b) ZrCuTi 50 nm/Ta 50 nm pillar. The strain levels for (a) and (b) are both for the elastic-to-shear transition stage).

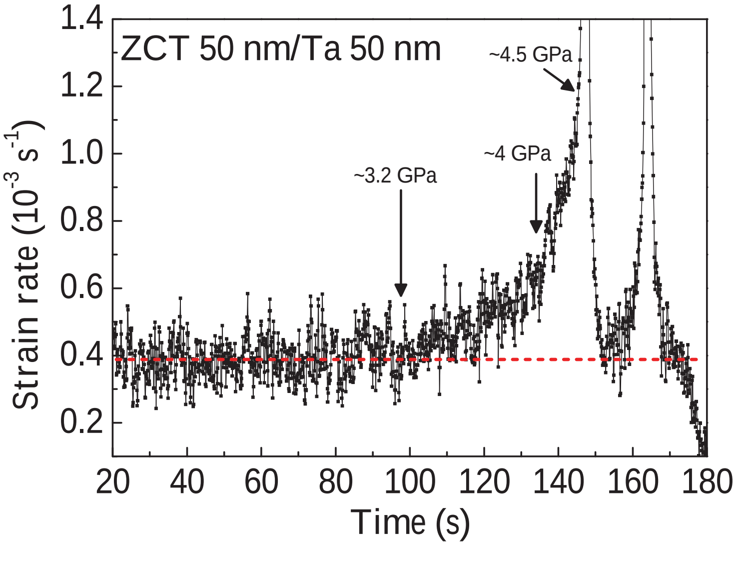

Fig. 5-32 Relationship between time and strain rate.

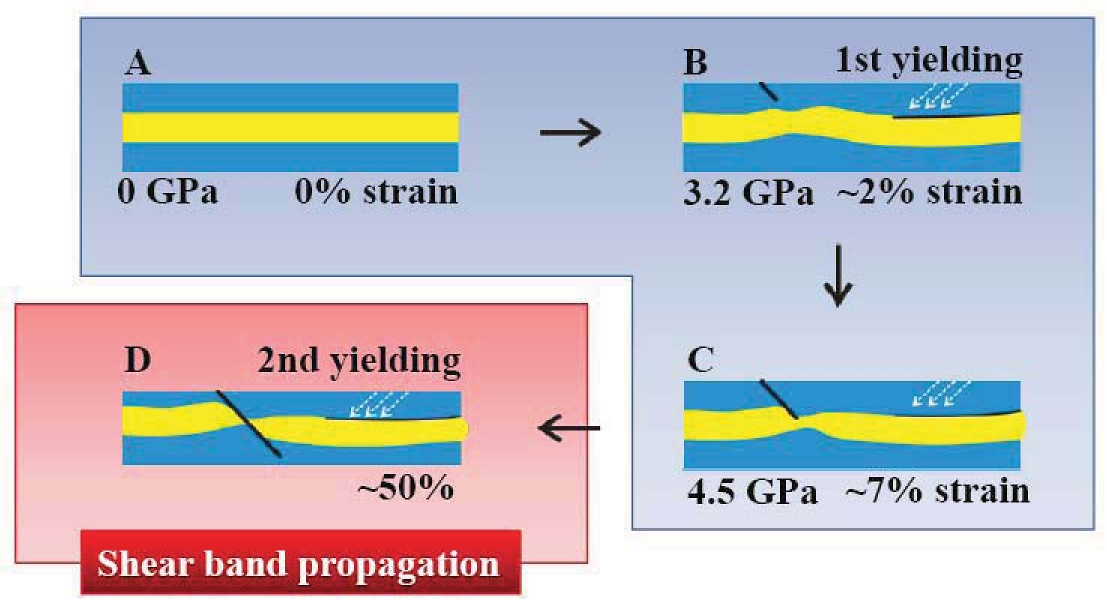

Fig. 5-33 Deformation mechanism of the amorphous ZrCuTi 50 nm/nanocrystalline Ta 50 nm nanolaminate micropillar.